



## 저작자표시-비영리-변경금지 2.0 대한민국

이용자는 아래의 조건을 따르는 경우에 한하여 자유롭게

- 이 저작물을 복제, 배포, 전송, 전시, 공연 및 방송할 수 있습니다.

다음과 같은 조건을 따라야 합니다:



저작자표시. 귀하는 원저작자를 표시하여야 합니다.



비영리. 귀하는 이 저작물을 영리 목적으로 이용할 수 없습니다.



변경금지. 귀하는 이 저작물을 개작, 변형 또는 가공할 수 없습니다.

- 귀하는, 이 저작물의 재이용이나 배포의 경우, 이 저작물에 적용된 이용허락조건을 명확하게 나타내어야 합니다.
- 저작권자로부터 별도의 허가를 받으면 이러한 조건들은 적용되지 않습니다.

저작권법에 따른 이용자의 권리는 위의 내용에 의하여 영향을 받지 않습니다.

이것은 [이용허락규약\(Legal Code\)](#)을 이해하기 쉽게 요약한 것입니다.

[Disclaimer](#)

Doctor of Engineering

Study of Functionalized Biocompatible Nanomaterials  
for Disease Diagnosis and Treatment

The Graduate School  
of the University of Ulsan  
Department of Medicine  
Huifang Liu

Study of Functionalized Biocompatible Nanomaterials  
for Disease Diagnosis and Treatment

Supervisor: Yong Shin, PhD

A Dissertation

Submitted to

The Graduate School of the University of Ulsan  
in partial Fulfillment of the Requirements for the Degree of  
Doctor of Engineering

By

Huifang Liu

Department of Medicine

University of Ulsan, Republic of Korea

February, 2021

# Study of Functionalized Biocompatible Nanomaterials for Disease Diagnosis and Treatment

This certifies that the dissertation  
of Huifang Liu is approved

Committee Chair Dr. Kim, Jun Ki

Committee Member Dr. Shim, In Kyong

Committee Member Dr. Kim, Sung Han

Committee Member Dr. Yun, Kyusik

Committee Member Dr. Shin, Yong

Department of Medicine  
University of Ulsan, Republic of Korea  
February, 2021

## ACKNOWLEDGEMENT

Thank you Father Lord for giving me the great time studying in University of Ulsan under the supervisor Prof. Shin, Yong. How grateful present I have ever received for these four years: faith experience, mentorship, friendship, research study etc. All of these experiences have being important parts of my life and guiding me on the miracle mission journey. Meanwhile I would like to extend my sincerely thanks to all of the kind support and help from uncountable individuals, particularly:

Thanks to Prof. Yong Shin for guiding me faithfully and taking care of my living life in Korea. He always supports and motivates us in research study patiently, encourages and guides us in growing up faithfully. I saw an energetic mission from him that do every effort on research for the blessed humans, one step by one step.

Thanks to all of the committee members of this dissertation: Prof. Jun Ki Kim, Prof. In Kyong Shim, Prof. Sung Han Kim and the advisor of my master couse Prof. Kyusik Yun for their insightful comments and encouragement during the course.

Thanks to my seniors: Dr. Fei Zhao, Dr. Linlin Zhong, Dr. Saravanan Govindaraju etc. and my lab colleagues: Dr. Yoon OK Jang, Thuy Nguyen Thi Dao, Bonhan Koo, Zhen Qiao, Yange Luan, Qingshuang Zou, Myoung Gyu Kim, Hyo Joo Lee etc. for their timely help and friendship.

Thanks to my dear sisters / brothers from church and friends on the way to church for their continuous prayer and companion.

Thanks to my beloved father Kehu Liu, mother Chunling Liu, brother Zhixing Liu, how grateful for me with them, love me protect me support me encourage me...They are my warm families, good teachers, close friends and wisdom heroes. To NARUTO ‘Hatake Kakashi, Nara Shikamaru...’ my youth, my passion.

Thanks Jesus Christ for bringing you all to my life in the miracle journey and growing me up. To me, from present to mission, how lucky and grateful I am. All in prayer and blessed to be blessing.

Yes U (Huifang Liu)

## ABSTRACT

Currently, pathogen identification and therapeutic approaches play important roles in controlling infections. On one hand, the traditional gold standard diagnostic method, i.e., culturing and colony counting, is limited by long waiting times (and thus wasted time), as culturing of most clinical bacterial pathogens requires 1–2 d (much longer times are required for several bacterial species), and low efficiency due to contamination and significant experimental error. On the other hand, the treatment options are limited due to the shortcoming of the pharmaceutical effect and the increased drug resistance. Therefore, rapid and effective detection technologies are urgently needed for an early-stage diagnosis, at which time there are low concentrations of the target pathogen. And research on novel antibiotic agents are especially important for fighting epidemic antimicrobial infections.

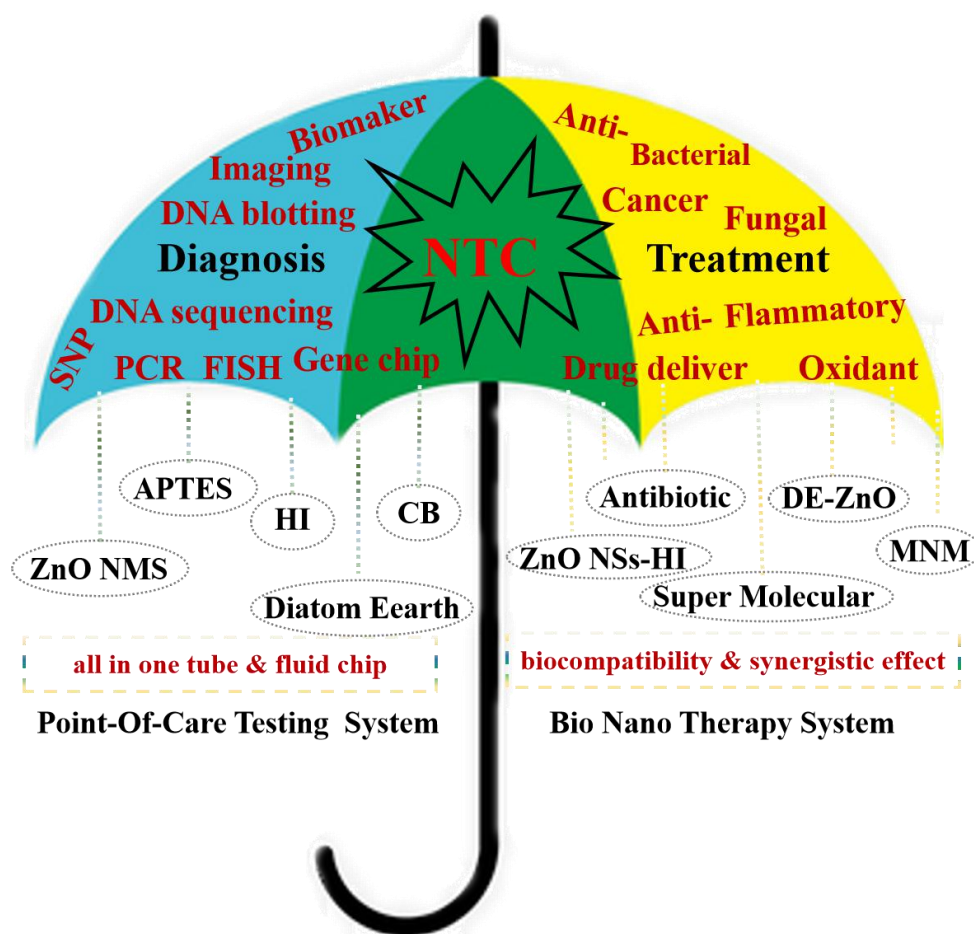
We focused on studying the bioapplications including disease diagnosis and treatment with functionalized biocompatible nanomaterials. Hereby, the useful tools for rapid and sensitive nucleic acid isolation-detection without large instruments and detergent in the field of molecular diagnostics and synergistic effect of nanomaterials on antibiotic therapy have been studied and developed in our research team.

As the representative semiconductor, the ZnO nanomaterials dissolve to ionic zinc ( $\text{Zn}^{2+}$ ) and particle-induced generation of reactive oxygen species (ROS) in the solution which represent the primary mechanism of further applications. We have studied the synthesis routes of ZnO nanomaterials that allow better control of the shape and size of nanomaterials as well as use for nucleic acid extraction-detection and pathogenic bacterium therapy.

Meanwhile, diatomaceous earth (diatom), a naturally assembled amorphous silica architecture presents a single morphology as a microscale hollow particle with numerous nanoscale pores in the wall and abundant hydroxyl groups on its surface, which suggesting ease of chemical modification and subsequent use in biological

applications. Hereby, we designed the appropriated modification on diatom and applied for sample preparation.

The binary nanomaterials (ZnO nanomaterials and diatom) integrated with surface modification and homobifunctional imidoester (HI) cross-linking have been designed for Point-of-care testing (POCT) system. Meanwhile, the synergistic effect of nanomaterials been studied with enhanced antibiotic activity against fungi (*Aspergillus fumigatus*) and Gram-negative bacteria (*Escherichia coli* and *Salmonella enterica*).



**Scheme 1. Overview of our studies on Nanotechnology (NTC) in disease diagnosis and treatment.**

Topic on point of care testing (POCT) system and bio nano therapy (BNT) system.

# TABLE OF CONTENT

ACKNOWLEDGEMENT.....	i
ABSTRACT.....	ii
TABLE OF CONTENT.....	iv
LIST OF SCHEMES.....	vii
LIST OF FIGURES.....	viii
LIST OF TABLES.....	x
ABBREVIATION.....	xi
SECTION 1. NANOMATERIALS ON DIAGNOSE.....	1
1.1 INTRODUCTION.....	2
1.1.1 Multi-applications and directions of Nucleic Acid study.....	2
1.1.2 Opportunities of the NTC in disease diagnosis and treatment.....	3
1.1.3 The character of surface modification with molecular.....	5
1.1.4 Overview of our related researches.....	7
1.2 EXPERIMENTAL SECTION.....	10
1.2.1 Chemicals and Reagents.....	10
1.2.2 Instruments.....	11
1.2.3 Biological samples.....	12
1.2.4 Morphological control of ZnO NMS synthesis.....	13
.....	13
.....	13
1.2.5 Preparation of biocompatible composites (CB-DA) .....	14
1.2.6 Cell lysis with ZnO NMS.....	15
1.2.7 Functionalized DE and DMS for NA extraction.....	16
1.2.8 Nano-composites with the DTBP system for NA isolation.....	17
1.3 RESULTS AND DISCUSSION.....	18
CHAPTER 1 Large instrument-and detergent-free assay for ultrasensitive nucleic acids isolation via binary nanomaterial.....	18
1.(3-1).1 Working principle of nanomaterials for sample preparation....	18
1.(3-1).2 Usefulness of ZnO NMS for breaking the cell membrane.....	20
1.(3-1).3 Usefulness of binary nanomaterials for sample preparation....	24
1.4.1 CONCLUSION.....	29
CHAPTER 2 Dimethyl 3, 3'-dithiobispropionimidate (DTBP) as a cleavable disulfide-based polymer to encapsulate nucleic acids in biological sample preparation.....	31
1.(3-2).1 Biomolecule encapsulation by DTBP.....	31
1.(3-2).2 Characterization of DA and DTBP composite systems.....	33
1.(3-2).3 DA-DTBP composite in ZnO NMS systems.....	35
1.(3-2).4 Application of DA-DTBP composites to the ZnO NMS system.....	38
1.(3-2).5 NA release from cleavable disulfide cross-linkers.....	40
1.4.2 CONCLUSION.....	42
CHAPTER 3 A Sample Preparation Technique Using Biocompatible	



Composites for Biomedical Applications.....	43
1.(3.3).1 Design and principle of the CB-DA biocompatible composite.....	43
1.(3.3).2 Preparation and characterization of DA.....	45
1.(3.3).3 Preparation and characterization of CB-DA.....	48
1.(3.3).4 Cell and pathogen enrichment using the CB-DA.....	51
1.(3.3).5 Nucleic acid isolation using the CB-DA.....	52
1.4.3 CONCLUSION.....	54
SECTION 2 NANOMATERIALS ON TREATMENT.....	55
2.1 INTRODUCTION.....	56
2.1.1 Challenges of the Nanotechnology (NTC) in treatment.....	56
2.1.2 The introduction of studied materials.....	57
2.1.3 Overview of our related researches.....	59
2.2 EXPERIMENT SECTION.....	62
2.2.1 Chemicals and Reagents.....	62
2.2.2 Biological samples.....	63
2.2.3 Functionalized materials.....	64
2.2.4 Characterization.....	69
2.2.5 Dye removal (adsorption).....	70
2.2.6 Adsorption equilibrium experiment.....	72
2.2.7 In vitro cytotoxicity assay.....	73
2.2.8 ROS detection.....	74
2.2.9 Antibacterials.....	75
2.2.10 Antifungal Assay via Radial Growth.....	76
2.2.11 In vitro blood test.....	77
2.2.12 In vivo toxicity assay.....	78
2.3 RESULTS AND DISCUSSION.....	79
CHAPTER 1 Cucurbituril-based Reusable Nanocomposites for Efficient Molecular Encapsulation.....	79
2.(3-1).1 CB-coated amine-modified DE for pathogen removal.....	79
2.(3-1).3 The zeta potential of the materials.....	83
2.(3-1).4 Dye removal testing.....	84
2.(3-1).5 Dye removal mechanisms.....	86
2.(3-1).6 Dye and pathogen removal testing.....	89
2.(3-1).7 Time-saving loading design.....	89
2.4.1 CONCLUSION.....	92
CHAPTER 2 An enhanced recyclable 3D adsorbent for diverse bio-applications using biocompatible magnetic nanomulberry and cucurbituril composites.....	93
2.(3-2).1 Principle of MNM-DE-CB.....	93
2.(3-2).2 Characterization and analysis of MNM-DE-CB.....	94
2.(3-2).3 Efficient dye removal by MNM-DE-CB.....	98
2.(3-2).4 Reproducibility and large volume testing of MNM-DE-CB..	103
2.(3-2).5 Biocompatibility and drug testing of MNM-DE-CB .....	106
2.4.2 CONCLUSION.....	107

CHAPTER 3 Facile Homobifunctional Imidoester Modification on Advanced Semiconductor Nanomaterials for Enhanced Antibiotic Synergistic Effect and Biocompatibility.....	108
2.(3-3).1 Characterization of the ZnO NSs-HI.....	108
2.(3-3).2 Bioapplications of the studied materials.....	112
2.(3-3).3 Antibacterial and synergistic antifungal effect of ZnO NSs-HI116	
2.(3-3).4 Biocompatibility study with vitro blood and mice vivo test..	120
2.4.3 CONCLUSION.....	124
CHAPTER 4 A Diatom Earth Framework Semiconductor Composite Assisted Antibiotic with Enhanced Efficacy and Therapy Persistence in Nano-therapy.....	126
2.(3-4).1 Synthesis and characterization of the DE-ZnO.....	126
2.(3-4).2 Antibacterials study of DE-ZnO.....	130
2.(3-4).3 Antifungal study of DE-ZnO.....	134
2.(3-4).4 Synergistic and persistence of DE-ZnO composites.....	136
2.(3-4).5 Biocompatibility and toxicity DE-ZnO composites in vivo...	138
2.4.4 CONCLUSION.....	140
SUMMARY.....	142
REFEENCE.....	143
ABSTRACT IN KOREAN.....	152
ABOUT THE AUTHOR.....	153
LIST OF PUBLICATIONS.....	153
PERSONAL PROFILE.....	155

## LIST OF SCHEMES

Scheme 1 . Overview of our studies on Nanotechnology (NTC) in disease diagnosis and treatment. ....	iii
Scheme 2 . Multi-applications and directions of Nucleic Acid study (DNA, RNA etc.).....	3
Scheme 3 . Recent opportunities and characteristic of the Nanotechnology (NTC) in disease diagnosis and treatment. ....	5

## LIST OF FIGURES

Figure 1.1.1 The schematic of single tube NA isolation via nanomaterial.....	20
Figure 1.1.2 Usefulness of ZnO NMS for breaking the cell membrane.....	21
Figure 1.1.3 Application of ZnO NMS for lysis of prokaryotic cells.....	22
Figure 1.1.4 Application of ZnO NMS for lysis of eukaryotic cells. ....	24
Figure 1.1.5 A Usefulness of binary nanomaterial for sample preparation ...	26-27
Figure 1.1.6 Application of nanomaterial for NA isolation and detection.....	29
Figure 1.2.1 Schematic representation of the principle.....	33
Figure 1.2.2 Characterization of DA and DTBP composite systems.....	35
Figure 1.2.3 The DA-DTBP composite in the ZnO NMS system.....	37-38
Figure 1.2.4 Application of DA-DTBP composites in the ZnO NMS system.....	40
Figure 1.2.5 NA release from the cleavable disulfide cross-linker.....	42
Figure 1.3.1 Characterization of the studied materials.....	45
Figure 1.3.2 Schematic of the process flow for functionalization of DA.....	47-48
Figure 1.3.3 Schematic representation of CB-DA.....	50-52
Figure 1.3.4 Pathogen enrichment schematic and demonstration.....	52
Figure 1.3.5 NA isolation using the biocompatible composite.....	54
Figure 2.1.1 Illustrative diagram of CB-DA for dye and pathogen removal.....	81
Figure 2.1.2 Characterization of the surface of DE.....	83
Figure 2.1.3 Cucurbituril (CB) coating of DA in an aqueous medium.....	85
Figure 2.1.4 Characterization of CB-DA.....	88
Figure 2.1.5 Applications of CB-DA.....	90
Figure 2.2.1 Schematic illustration of the preparation of MNM-DE-CB.....	94
Figure 2.2.2 Characterization of MNM-DE-CB.....	97
Figure 2.2.3 Verification of MNM-DE-CB.....	100
Figure 2.2.4 Application of MNM-DE-CB.....	102
Figure 2.2.5 Reproducibility and 50 mL volume testing of MNM-DE-CB	104-105
Figure 2.2.6 Biocompatibility testing of MNM-DE-CB.....	106

Figure 2.3.1 Chemical characterization of our tested ZnO nanomaterials.....	110-111
Figure 2.3.2 Bioapplications of the studied materials.....	114
Figure 2.3.3 Study on the ZnO NSs-HI with the antifungal properties.....	118-119
Figure 2.3.4 Biocompatibility and toxicity of ZnO NSs-HI in vitro blood test.	121
Figure 2.3.5 Biocompatibility and toxicity of ZnO NSs-HI in vivo.....	123
Figure 2.4.1 Procedure and characterization of the DE-ZnO.....	127
Figure 2.4.2 Antibacterial activity and bio-safety dosage study of DE-ZnO.....	132
Figure 2.4.3 Antifungal activity study of DE-ZnO.....	135
Figure 2.4.4 Synergistic and persistence of DE-ZnO against fungal infection...	137
Figure 2.4.5 Biocompatibility and toxicity of the DE-ZnO in vivo.....	139
Figure 2.4.6 Perspectives of this DE-ZnO in the industry applications.....	141

## LIST OF TABLES

Table 1	Primers used in this study.....	12
Table 2	Comparison with other researches: the KL , the absorbance constant, pH effect and reaction condition for the materials.....	91

## ABBREVIATION

APDMS	3-Aminopropyl(diethoxy)methylsilane
APTMS	(3-Aminopropyl)trimethoxysilane
BNT	Bio Nano Therapy
CB	Cucurbituril
CT	Computerized Tomography
Ct	Cycle Threshold
CTAB	Cetyltrimethylammonium Bromide
DA	Amino-functionalized Diatomaceous Earth
d	days
DE	Diatomaceous Earth
DMA	Dimethyl Adipimide
DMP	Dimethyl Pimelimide
DMS	Dimethyl Suberimide
DTBP	3,3'-Dithiobispropionimide
DNA	Deoxyribonucleic Acid
DW	Distilled Water
FE-SEM	Field-Emission Scanning Electron Microscopy
HI	Homobifunctional Imidoester cross-linkers
IA	Invasive Aspergillosis
min (s)	Minute (s)

MNM	Magnetic Nanomulberry
NA	Nucleic Acid
ND	Negative Diagnosis
NMS	Nano-Multigonal Shuttle
NTC	Nanotechnology
PCR	Polymerase Chain Reaction
POCT	Point-Of-Care Testing
RT	Room Temperature
ROS	Reactive Oxygen Species
TEM	Transmission Electron Microscopy
ZnO	Zinc Oxide
ZnO NP	Zinc Oxide Nanoparticles
ZnO NSs	Zinc Oxide Nano Spindle
ZnO NMS	Zinc Oxide Nano-multigonal Shuttle,

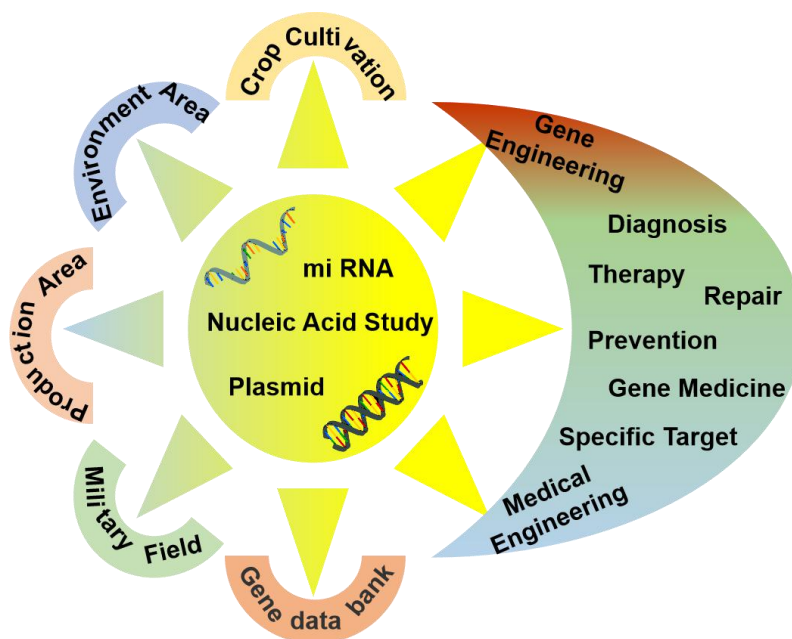


## **SECTION 1. NANOMATERIALS ON DIAGNOSE**

## **1.1 INTRODUCTION**

### **1.1.1 Multi-applications and directions of Nucleic Acid study**

As the world moves toward rapid molecular diagnosis, the quick and reliable detection of small amounts of nucleic acid (NA) has been increasingly in multi-applications.[1-5] (Scheme 2). Sample preparation steps including cell lysis and isolation and extraction of NA are particularly crucial for the quantification of trace analytes in complex sample matrices.[6-9] However, the spin column based methods require large instruments and toxic chemical reagents for sample preparation, which curve development of a point-of-care testing (POCT) system integrated with a detection system.[10-12] General commercial cell lysis detergents suffer from limitations such as unsuitability for isolating sensitive proteins and NA, difficulty of removing the chemical reagent from samples after lysis, and low lysis efficiency.[13-14] Therefore, there is a particularly urgent need to develop a new sample preparation approach that can be useful for POCT in clinical applications and overcomes the drawbacks of traditional methods such as instrument requirements, chaotropic chemicals, intensive labor, time consumption, and low yield of NA.[15-17] Recently, microfluidic technique-based sample preparation assays have been demonstrated as novel and promising technologies.[18-20] The microfluidic designs enable integration of different modules (or operations) into one device, and the intracellular products directly post processed inside the same device, which has been tested for efficiency.[21-22] Mechanical lysis-based microfluidic systems are complex to fabricate, and it can be difficult to collect the target materials from the complex mixture. In addition, the use of other optical, acoustic, and electrical lysis-based microfluidics is obstructed by complex and expensive technology.[23-24] Thus, an all-in-one system for both continuous cell lysis and rapid NA extraction without the assistance of any other substances is required compatible with downstream analysis that is still in demand for many clinical diagnostic applications.



**Scheme 2. Multi-applications and directions of Nucleic Acid study (DNA, RNA etc.)**

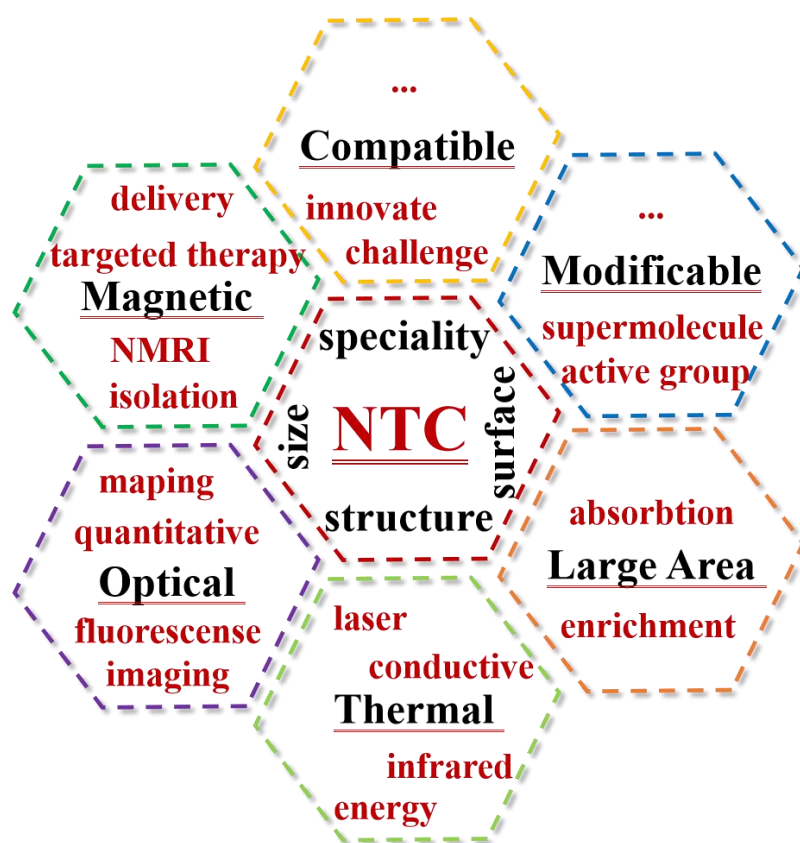
### **1.1.2 Opportunities of the NTC in disease diagnosis and treatment.**

Driven by the characteristic in size - structure - surface and various speciality, the nanotechnology (NTC) exhibit unique physical, chemical, and biological properties and have gained increasing interest over the past twenty years.[25-26] The use of nanomaterials has not been fully explored in this field of research, and their potential applications are still attracting much attention.[27-28] Rational design of nano-composite technologies can effectively enhance the desired properties of substrates and produce new benefits, such as optical and magnetic properties that can be exploited in piezoelectric actuators and sensors, organic solar cells, and intrinsic conductive polymers for use in biomedical sciences.[29-32] Numerous composite technologies have been developed, and covalently immobilized compounds with diverse dynamic properties have been integrated extensively into hybrid devices to isolate and transport biomolecules in nanoscale diagnostic systems.

For example, zinc oxide (ZnO) nanomaterials have been widely applied in antibacterial effect, electronics, photo-electronics, sensors, and photo-catalysts with

excellent chemical and conductivity properties.[33-37] ZnO dissolution to ionic zinc ( $\text{Zn}^{2+}$ ) and particle-induced generation of reactive oxygen species (ROS) represent the primary modes of action for antibacterial purposes.[38-39] In Kim's study, a feature ZnO nanowire-based microfluidic device was fabricated for mechanical cell lysis with detergents, and in So's study, a handheld device with a porous silicon surface containing ZnO nanowires was described and used for continuous mechanical cell lysis and rapid DNA isolation.[20, 40-41] The ZnO nanomaterial collides with the cells, disrupting the cell membrane in a physical manner. The released  $\text{Zn}^{2+}$  from the ZnO nanomaterial surrounding the cells also suddenly changes the ion concentration between the inside and outside of the cells.[42-44] Subsequently, water enters the cells, which swell and burst in a chemical manner. Furthermore, the ZnO nanomaterial induces generation of reactive oxygen species (ROS:  $\text{O}_2^{\cdot-}$ ,  $\cdot\text{OH}$ ,  $\cdot\text{H}_2\text{O}_2$ ) that react with the peptidoglycan layer and break the glycosidic bonds in a biological manner.[38, 45-46] Those studies have motivated an upsurge of synthesis routes of ZnO nanomaterials that allow better control of the shape and size of nanomaterials as well as use for further applications with NA extraction and sensor detection.

Meanwhile, diatomaceous earth (diatom) as a naturally assembled amorphous silica architecture shows exceptional precision and detail compared with common artificialities such as well-ordered, countless, and nanosized pores on the surface, high surface area ( $200 \text{ m}^2/\text{g}$ ), and abundant active hydroxyl groups.[47-49] Diatom mainly presents a single morphology as a microscale hollow particle with numerous nanoscale pores in the wall. The abundant hydroxyl groups on its surface were easily modified, suggesting ease of chemical modification and subsequent use in biological applications.[50-51] Recently, modified diatom has been exploited as an effective solid-phase for cell/pathogen enrichment and NA extraction, which resulted in a simple single-tube method for the diagnosis of zoonotic disease.[52-54]



**Scheme 3. Recent opportunities and characteristic of the Nanotechnology (NTC) in disease diagnosis and treatment.**

### **1.1.3 The character of surface modification with molecular**

Motivated by the widespread development of nanotechnology, various nanomaterials and novel technologies have recently been employed in a diverse range of fields, the surface modification has played an important character in promote the NTC into bioapplications.[55-57] Among, 3-Aminopropyltriethoxysilane (APTES) and 2-Aminopropyltrimethylethoxysilane (APDMS) are mainly used as a dispersant. APTES / APDMS attaches an amino group to the functional silane for bio-conjugation which are used to improve the adhesion of graphene flakes and SiO<sub>2</sub> to enable better contact with the metal electrodes. These electrodes may be used as electro-responsive tools for bio-sensing applications.[24, 58-59] It can be used to functionalize silane diazirine for fiber optic biosensor application.

Meanwhile, cross-linking polymers (synthetic or natural) may promote bio-molecular interactions and other properties that can be exploited in biomedical applications.[60-61] Cross-linking polymers, such as dimethyl adipimide (DMA), dimethyl pimelimide (DMP), dimethyl suberimide (DMS), and 3,3'-dithiobispropionimide (DTBP) have been exploited in biomedical applications, such as disease diagnostics and drug delivery.[62-63] Recent innovations in typical reduction-sensitive disulfide bonds, which previously posed formidable challenges to composite technologies, have led to tremendous developments for biomedical application as disease diagnostics, biomarkers, and gene therapies.

In addition, the pumpkin-shaped cucurbituril (CB) family, which plays an important role in host-guest chemistry, has been employed in various applications involving molecular encapsulation, water treatment, surface adhesion, biomarker-targeted theranostics, and drug delivery.[64-66] CB consists of  $n$  glycoluril motifs ( $n=5-8, 10, 14$ ) linked by methylene bridges to form two hydrophilic carbonylated portals and a hydrophobic cavity.[67-68] Driven by a diverse range of inter- and intramolecular interactions, CB has been identified as an ideal host for charged amphiphilic guests due to ion-dipole stabilization and possible hydrogen bonding inside the CB cavity.[69] Although the great potential of CB has been highlighted in many studies, three main performance limitations have also been identified for the CB family: (1) unexplained poor solubility in aqueous solutions, (2) unsuccessful functional group modification, and (3) unclarified ion effects in CB applications.[70] In particular, the poor solubility of CB poses a serious obstacle for the development of CB applications.[71] Thus, numerous research efforts have attempted to overcome these limitations by developing new water-soluble host/guest systems with a synergistic blend of supramolecular assemblies and nanomaterials

Conventional diagnostic systems suffer from various limitations, such as low sensitivity, requirements of complicated reagent system and multiple auxiliary instruments, and incomplete purification of biomolecules. To overcome these limitations, emerging nano-composites are leading to overall improvements in human medical engineering applications, with improved sensitivity and simplicity.[72-73]

Nano-composites with general advantages of high surface area can be produced by coating with silanization, and these can be used in assembly's with proteins and nucleic acids as solid substrates. These technologies have dominated the diagnostic market, offering convenient and low-cost downstream analyses for rapid and sensitive disease diagnosis and high-efficiency nano-therapy.[72,74-76]

#### **1.1.4 Overview of our related researches**

In chapter 1, we introduce an innovative large instrument- and detergent-free assay for ultrasensitive nucleic acids isolation and detection via a binary nanomaterial that is a combination of a ZnO NMS and diatom with dimethyl suberimidate complex (DDS). Firstly, we studied the synthesis route, which allows for control of the shape and size of the ZnO nanomaterial. An economical and simple size-controlled growth route of ZnO NMS is presented, and its application in NA extraction is verified. We compared the commercial ZnO nanoparticles (NP; 20 nm) and synthesized ZnO NMS (200~1000 nm) for the purpose of cell lysis to avoid the problems introduced by detergent and thermal instruments. We found that the ZnO NMS can have good cell lysis ability at room temperature (RT) within 2 min in several cells (eukaryotic and prokaryotic cells) compared with that of ZnO NP and a spin column kit with detergent and a thermal instrument. Next, we combined the ZnO NMS with DDS complex for the capture and isolation of NA from cells (cancer cell lines, *Brucella ovis*, *Escherichia coli*, *Salmonella* spp., *Staphylococcus aureus*, and *Bacillus cereus*) to avoid the problems of chaotropic reagents and large instruments such as centrifuges and vortexes. Using this binary nanomaterial, a high quality and quantity of NA can be isolated and extracted within 15 min at RT without large instruments and chaotropic detergent for enhancement of downstream analysis. Consequently, the detection sensitivity with the binary nanomaterial was enhanced 100 times that of the spin column based methods.

In chapter 2, we present a novel functionalization scheme using amine-modified diatomaceous earth (DA) to capture and release nucleic acids in DTBP, which acts as

a cleavable disulfide cross-linker for sample preparation in disease diagnostics. In these studies, the DA was used as a solid extraction substrate due to its low environmental impact, high biocompatibility, and significant advantages of scalability, structural reproducibility, and low production cost. Nucleic acid isolation using DTBP with DA yielded 100 folds efficacy compared with a commercially available spin column-based reference kit. Additionally, we used a zinc oxide nanomultigonal shuttle (ZnO NMS) to replace chaotropic detergents for cell lysis.[25, 26] In addition to achieving cell lysis, ZnO NMS produced oxidative environments that protected the disulfide bonds of DTBP. In further experiments, we eluted nucleic acids from nano-composites without using PCR inhibitors, such as bile salts, bilirubin, EDTA, NaCl, SDS, and Triton X-100.[27] We only used DTT to cleave disulfide bonds of DTBP after encapsulation of nucleic acids, and to remove potential PCR inhibitors. Under this novel functionalization scheme with nano-composite DTBP, we demonstrated encapsulation and release of nucleic acids in eukaryotic and prokaryotic cells. Our data show more efficient extraction of nucleic acids without PCR inhibitors than that achieved with the widely used Qiagen extraction kit. Therefore, nano-composites with cleavable disulfide linkages have promise as novel functional schemes for various biological applications, including diagnostics and therapeutics.

In chapter 3, an efficient method for fabricating a cucurbituril-decorated, amine-modified diatom composite (CB-DA) is proposed, and the usefulness of this CB-DA composite for efficient sample enrichment and in-situ nucleic acid preparation from pathogens and cells is demonstrated. The well-characterized process of amino functionalization of the surface of DE renders it a universal tool for targeting molecules, and cucurbit[6]uril (CB) has been introduced to enhance the ability of CB-DA composites to rapidly and efficiently adsorb molecules [3, 16, 17]. We have also verified that modification with APDMS (3-aminopropyl-methyl-diethoxysilane) is more effective than traditional modification with APTES (3-aminopropyl-triethoxysilane). Characterization of the surface charge (as represented by the zeta potential) indicated that the charge conferred by the APDMS modification is about twice that conferred by the APTES modification.



Furthermore, the efficiency of the CB-DA composite to enrich for pathogens and cells was examined using three approaches. First, we tested the absorbance of supernatants collected after CB-DA enrichment. The results show that the enrichment efficiency was as high as 90% within 3 mins, even at an *Escherichia coli* concentration of  $10^6$  cfu/mL. Second, the morphology of the composites precipitated by the CB-DA system showed that numerous eukaryotic cells adhered to the surface of the CB-DA. Third, we also compared the performance of real-time PCR using amplified DNA, samples collected from the CB-DA enrichment system, and DNA extracted via a commercial column system as templates. The results showed an approximately 4-fold increase in the early amplification signal. In summary, we have confirmed that this CB-DA composite system can provide improved performance for bio-sample preparation for early diagnosis.

## 1.2 EXPERIMENTAL SECTION

### 1.2.1 Chemicals and Reagents

All reagents were of analytical grade and used without further purification. Zinc nitrate hexahydrate ( $\text{Zn NO}_3 \cdot 6 \text{ H}_2\text{O}$ , 98%), ammonium hydroxide solution (28%  $\text{NH}_3$  in  $\text{H}_2\text{O}$ , 99.99% trace metals basis), and (3-aminopropyl) triethoxysilane (APTES, 98%) 3-aminopropyl(diethoxy)methylsilane 97% (APDMS) were purchased from Sigma-Aldrich (St. Louis, MO, USA). Cucurbit[6]uril hydrate was also obtained from Sigma-Aldrich (St. Louis, MO, USA). Hexadecyltrimethylammonium bromide ( $\text{C}_{19}\text{H}_{42}\text{BrN}$ , >98%, CTAB) was produced by Tokyo Chemical Industry Co., Ltd (Tokyo, Japan). Proteinase K Solution (Mat. No. 1014023, Qiagen, Germany) is commonly used to digest protein and remove contamination in the nucleic acids. Commercial zinc oxide nanoparticles (dispersion, <40 nm average part size, 20 weight % in  $\text{H}_2\text{O}$ , China) were purchased as the substance for further characterization and comparison testing of the nanoparticles. We ordered the biocompatible diatomaceous earth (powder, suitable for most filtrations) from Sigma-Aldrich to use for design of the new NA extraction system. Milli-Q water with a resistance greater than 18 M $\Omega$ , 99% ethyl alcohol, phosphate-buffered saline (PBS, 10 $\times$ , pH 7.4), and streptavidin-coupled magnetic beads (Thermo Fisher Scientific, Waltham, MA, USA) were used in all experiments.

### 1.2.2 Instruments

The morphologies of the samples were examined using scanning electron microscopy (SEM; JEOL JSM-7500F, Tokyo, Japan). X-ray diffraction (XRD; Scintag-SDS 2000, Cupertino, CA) was performed at 40 kV voltage and 30 mA current with continuous-scanning  $2\theta$  mode to analyze the crystalline structures of the ZnO nanomaterials, and Fourier transform infrared (FTIR) spectroscopy (Nicolet 6700, Thermo Scientific) was used mainly for the analysis of the chemical properties of the samples. Raman measurements were performed using a Renishaw inVia Raman microscope system (Renishaw, Wotton-under-Edge, UK). The commercial QIAamp DNA/RNA Mini Kit (DNA Mini Kit: Cat No. 51304, RNA Mini Kit: Cat No.74104, Germany) was used as a spin column method for NA isolation. The kit was used following the supplier's instructions. The spin-down device for the centrifugation (CF-5, 100~240 Vas, 50/60 Hz, 8 W), vortex mixer (T5AL, 60 Hz, 30 W, 250 V), and LABOGENE 1730R (220V~, 60Hz, 2.0kVA, South Korea) and MSH-30d stirring heater were produced by Daihan Scientific Co., Ltd (Wonju-Si, South Korea). The AriaMx Real-Time PCR system (Agilent Technologies, Santa Clara, CA, USA), GeneAmp PCR system 9700 (LSK Singapore), electrophoresis apparatus (Submerge-Mini WSE-1710), Gel Documentation System (Clinx science instruments co. Ltd.) and NanoDrop 2000 spectrophotometer (PeqLab Korea) were used for the NA detection test.

### 1.2.3 Biological samples

Eukaryotic cells (HCT-116 colorectal cancer cells) were maintained in plastic culture dishes with high-glucose Dulbecco's Modified Eagle's Medium supplemented with 10% fetal calf serum (FCS) in a 37 °C humid incubator with 5% ambient CO<sub>2</sub>. *Brucella ovis* (ATCC 25840) was inoculated in Brucella agar (Sigma-Aldrich) with 5% defibrinated sheep blood (MBcell, Korea) and incubated at 37 °C in an atmosphere of 5% CO<sub>2</sub> for 48 h. *Escherichia coli* (ATCC 25922) was inoculated in nutrient broth medium and incubated for 24 h at 37 °C under an aerobic atmosphere. *Staphylococcus aureus* (ATCC 25923), and *Bacillus cereus* (ATCC 14579) were inoculated in Luria-Bertani (LB) medium and incubate overnight at 37 °C with shaking. All primers used for downstream analysis of cells are described in Table 1.

**Table 1.** Primers used in this study

	Primer	sequences (5'→3')	Annealing Tem. (°C)
<i>Actin</i>	<i>Actin-210F</i>	ATG GTG GGC ATG GGT CAG A	58
	<i>Actin-210R</i>	ACA TGA TCT GGG TCA TCT TCT C	
<i>18S rRNA</i>	<i>18S-F</i>	GCT TAA TTT GAC TCA ACA CGG GA	58
	<i>18S-R</i>	AGC TAT CAA TCT GTC AAT CCT CTC	
<i>E coli</i>	<i>Ecoli-rodA-195F</i>	GCA AAC CAC CTT TGG TCG	58
	<i>Ecoli-rodA-195R</i>	CTG TGG GTG TGG ATT GAC AT	
<i>Brucella</i>	<i>Brucella-O223F</i>	TGG CTC GGT TGC CAA TAT CAA	58
	<i>Brucella-O223R</i>	CGC GCT TGC CTT TCA GGT CTG	
<i>S. aureus</i>	<i>S. aureus F</i>	AAT CTT TGT CGG TAC ACG ATA TTC	56
		TTC ACG	
	<i>S. aureus R</i>	CGT AAT GAG ATT TCA GTA GAT AAT	
		ACA ACA	
<i>B. cereus</i>	<i>B. cereus F</i>	ATT GGT GAC ACC GAT CAA ACA	56
	<i>B. cereus R</i>	TCA TAC GTA TGG ATG TTA TTC	

#### **1.2.4 Morphological control of ZnO NMS synthesis**

The ZnO NMS crystals were synthesized by the hydrothermal method in alkaline medium. Briefly, 1 mL of 1 M  $\text{Zn NO}_3 \cdot 6 \text{ H}_2\text{O}$  and 1 mL of 1 M cetyl trimethyl ammonium bromide (CTAB) was added to 98 mL Milli-Q water in a 250 mL flask. The system was magnetically stirred (500 rpm) along with heating at 90 °C for 50 min. Subsequently, under steady stirring conditions, 2 mL ammonium hydroxide solution was added drop-wise to the reaction mixture. As stirring, the milky colloidal solution appeared. In order to evaluate the assay with an optimal morphology of ZnO NMS, we adjusted the reaction temperature (45 and 90 °C), reaction time (1, 3, and 5 min) and stirring speed (200 and 500 rpm) to control the growth of uniform ZnO NMS. For controlling the growth of ZnO NMS, the reaction flask was placed in a 0 °C freezer immediately for 10 min, then centrifuged, washed with Milli-Q water for 3 times for washing out the residual ions in the 50 mL Conical tube and dried the precipitate using the Vacuum Desiccator (Nalgene, USA) at RT for over night. The whole synthesis was carried out without any unusual treatment. Finally, the samples were stored in ethanol (99%) for further characterization and testing.

### **1.2.5 Preparation of biocompatible composites (CB-DA)**

The gravity-powered washing method was used to remove fragments from the commercial DE to prepare uniform DE. For the production of amine-modified diatomaceous earth (DA), the modification efficiencies of two types of amino polydimethylsiloxanes were compared. The electrokinetic potentials of the composite surfaces were assessed by measuring the zeta potentials. Briefly, serial aliquots of APTES or APDMS were added dropwise into 1 mL aliquots of 95% ethanol solution, followed by manual shaking for 3 mins at room temperature (RT). Subsequently, 50 mg of DE was added to the amino solution with stirring. The optimal reaction ratio and modification time were determined. The amino-functionalized DA was washed, collected by centrifugation, and dried in a vacuum overnight at RT. The DA powder was stored in a reagent bottle. Preparation of the CB-DA was performed via the microwave method. Briefly, 50 mg of DA was dissolved in 1 mL of DI water to form a 50 mg/mL DA solution. CB (25 mg) [6] was added to 1 mL of DI water, and this solution was then sonicated for 1 minute using an ultrasonic instrument. Subsequently, 20  $\mu$ L of the 25 mg/mL CB solution was added dropwise into 2 mL of prepared DA solution, followed by heating in a microwave oven for 1 minute. The double-functionalized CB-DA was washed and collected by centrifugation and then dried in a vacuum overnight at RT. The CB-DA powder was stored in a reagent bottle.

### **1.2.6 Cell lysis with ZnO NMS**

The commercial the spin column kit was used for testing the cell lysis properties of the ZnO NMS. The workflow for NA extraction with the spin column kit is shown in Figure 2A. For the first procedure, 100  $\mu$ L  $10^4$  HCT 116 cells was added into the 1.5-mL sample tube, and 100  $\mu$ L AL buffer, which is used in DNA extraction and causes cell lysis to expose the DNA, was mixed into the tube. After incubation at 56 °C for 10 min for DNA extraction and at RT for 1 min for RNA extraction, the prepared samples were transferred into the spin column kit for further washing and elution. For the second procedure, 100  $\mu$ L HCT 116 cells was added into the 1.5-ml sample tube, and 100  $\mu$ L ZnO NMS and 10  $\mu$ L Proteinase K solution were was mixed with the cells without any chaotropic detergent at RT for 2 min. After 3~5 times gentle pipetting for mixing well with 200  $\mu$ L size tip, the prepared samples were transferred into the spin column kit for further washing and elution. The quantity and purity of NA extracted from the cells were measured by PCR, real-time PCR, reverse transcription (RT)-PCR, and NanoDrop spectrophotometry. We confirmed that the proteinase K could not affect to PCR reaction.

### 1.2.7 Functionalized DE and DMS for NA extraction

For further testing of the ZnO NMS for sample preparation for a detergent-free assay, the diatom based-system was used with a modified previous protocol. The functionalized diatom-APTES and dimethyl suberimidate complex (DDS) were used with ZnO NMS as a binary nanomaterial for nucleic acids isolation and extraction in a 1.5-mL tube. APTES is selected not only for its robust coating of saline with covalent bond formation, but also for its chemical stability, which can be oxidized. DDS is combined with dimethyl suberimidate and diatom-APTES for the extraction of high-quality nucleic acids. This acts as a capture reagent that recognizes the amine groups on the sticky ends of nucleic acid fragments. Briefly, 100  $\mu$ L of cell sample solution was added into a 1.5-mL tube with 10  $\mu$ L of proteinase K and 100  $\mu$ L of ZnO NMS solution (different sizes) that was mixed gently with 3-5 times pipetting and incubated at RT for 2 min (10  $\mu$ L DNase was added for RNA extraction). Then, 2 mg/mL diatom-APTES was added, followed by 100  $\mu$ L of 100 mg/mL DDS solution. This mixture was vortexed well for 10 seconds then incubated at RT for 2 min. After the incubation, the supernatant was removed after the spin-down, and the precipitate was re-suspended twice with 200  $\mu$ L of PBS for washing using the vortexer and the spin-down device. Finally, 60  $\mu$ L of elution buffer (pH~10.6  $\text{NaHCO}_3$ ) was added and incubated for 1 min at RT. The DDS and NA are formed a complex at pH 8 and released at pH >10. After centrifugation with a spin-down device, the supernatant was transferred to a 1.5-ml tube. The extracted DNA or RNA was stored at -20 °C for downstream analysis. The quantity and purity of NA extracted from the cells were measured by PCR, real-time PCR, reverse transcription (RT)-PCR, and NanoDrop spectrophotometer.



### **1.2.8 Nano-composites with the DTBP system for NA isolation**

To test the performance of nano-composites following use of the DTBP system for nucleic acid isolation, we compared several potential combinations. Briefly, 100- $\mu$ L cell sample solutions were added to 1.5-mL tubes with 10  $\mu$ L of proteinase K and 100  $\mu$ L of lysis buffer solution that had been mixed by pipetting 3–5 times gently and incubating. We then added the traditional chaotropic reagent as a cell lysis buffer and incubated cells at 56 °C for 10 min. Alternatively, we added our synthesized ZnO NMS and lysed the cells at RT for 2 min in the absence of chaotropic reagent. Subsequently, 2-mg samples of DA were added, followed by 100  $\mu$ L of 50-mg/mL DMS or DTBP solutions. Mixtures were then vortexed well for 10 s and were incubated at RT for 2 min. After spinning down, supernatants were removed and precipitates were then washed twice by re-suspending in 200- $\mu$ L aliquots of PBS with vortexing and spinning down. Finally, 60- $\mu$ L aliquots of elution buffer that had been adjusted to pH 10.6 using  $\text{NaHCO}_3$  or DTT (for the novel elution system) were added and incubated for 1 min at RT. After centrifugation using the spin-down device, supernatants were transferred to 1.5-mL tubes and purified DNA or RNA fragments were stored at  $-20$  °C for downstream analyses. Quantities and purities of nucleic acids from the cells were measured using PCR, real-time PCR, reverse transcription-PCR, and a NanoDrop spectrophotometer.

## **1.3 RESULTS AND DISCUSSION**

### **CHAPTER 1 Large instrument-and detergent-free assay for ultrasensitive nucleic acids isolation via binary nanomaterial**

#### **1.(3-1).1 Working principle of nanomaterials for sample preparation**

Figure 1A shows the scheme of a large instrument- and detergent-free assay via binary nanomaterial for rapid NA extraction with high quantity and quality. This assay couples ZnO NMS for diverse cell (eukaryotic and prokaryotic) lysis without detergent and a specific incubation temperature and a DDS complex for NA isolation and extraction without large instruments. This binary nanomaterial assay can extract NA within 15 min at RT and offers the possibility of diagnostic testing. The sample preparation process via the binary nanomaterial consists of three steps in a single tube: cell lysis without chaotropic detergent at RT (break cell membrane), NA isolation (capture), and NA collection (elution) (Fig. 1.1.1.A). The ZnO NMS used in this study can break various cell membranes through its physical, chemical, and biological properties. These properties of ZnO NMS occur simultaneously in this study; the cells were lysed within 2 min via ZnO NMS without detergent and non-RT incubation (Fig.1.1.1B). Secondly, the DDS complex is used for isolation and extraction of NA as a solid substrate without instruments such as centrifuges and vortexes (Fig. 1.1.1C). The DDS complex couples amine-modified diatom and dimethyl suberimidate that can bind the NA. The complex reacts with the active amine group on both ends of double-stranded DNA or covalently bond in single-stranded RNA.

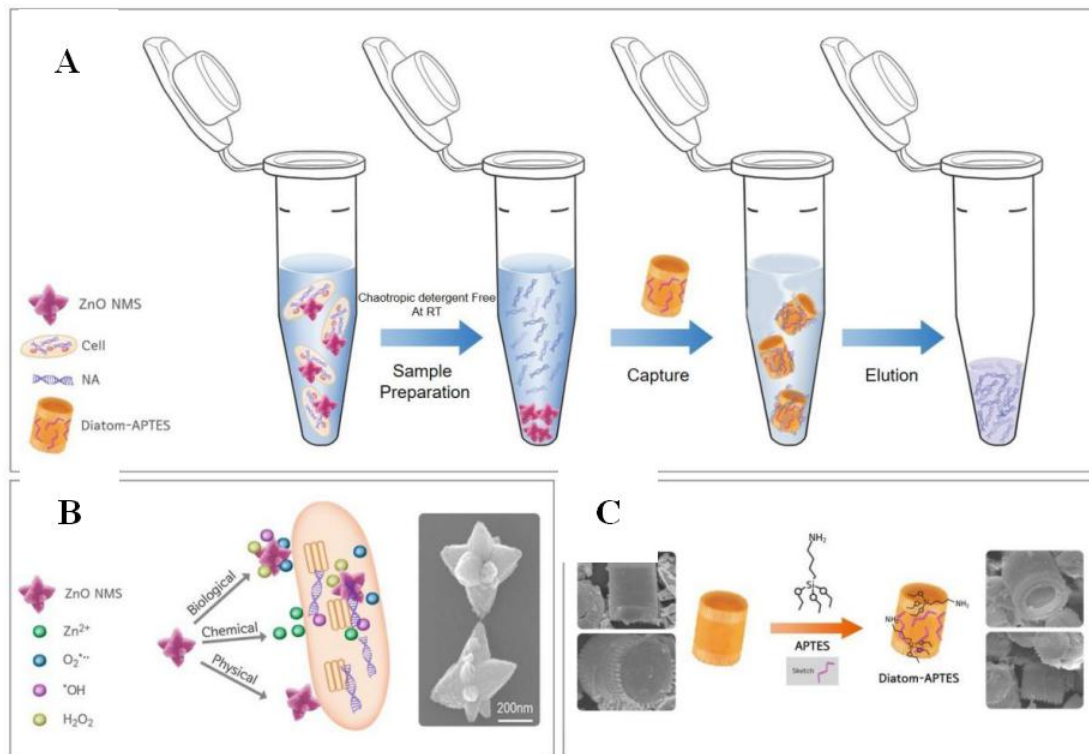


**Figure 1.1.1. The schematic of an innovative large instrument- and detergent-free assay in a single tube for ultrasensitive nucleic acids isolation via binary nanomaterial.**

(A) *In situ* sample processing involves ZnO nano-multigonal shuttle (NMS) and diatomaceous earth (diatom) with dimethyl suberimidate (DDS) in a single tube. (B) A schematic of ZnO NMS for breaking of cell membrane based on biological, chemical, and physical properties of ZnO. (C) The schematic of the DDS complex for isolation and extraction of NA (RNA and DNA) without centrifuges and vortexes. In a slightly acidic condition, the amine-modified diatom (diatom-APTES) captured NA and dimethyl suberimidate with high quantity and quality. Subsequently, the NA extracted from cells using the binary nanomaterial assay can be detected with highly sensitivity in downstream analysis.

## 1.(3-1).2 Usefulness of ZnO NMS for breaking the cell membrane

To test the usefulness of ZnO NMS as a nanomaterial for rapid cell lysis, we used various sizes of ZnO NMS from 100 nm to 1000 nm without detergent at RT (Fig. 1.1.2). To investigate usefulness of the nanomaterial in prokaryotic cells, the ZnO NMS was added into 100  $\mu$ L of *Brucella ovis* ( $10^4$  colony-forming units (CFU)/mL) solution. Then, the spin column kit was used for DNA extraction. The extracted DNA was used for downstream analysis by real-time PCR (Fig. 1.1.2.A). Based on the real-time PCR results, cell exposure to 500-nm ZnO NMS at RT for 2 min were the optimal conditions. The 500-nm ZnO NMS showed the earliest cycles with real-time PCR compared with other sizes. Even *Brucella* was detected one cycle sooner via the ZnO NMS (at RT for 2 min) than with the spin column kit (at 56 °C for 10 min,  $p=0.0002$ , Fig. 1.1.2.B).

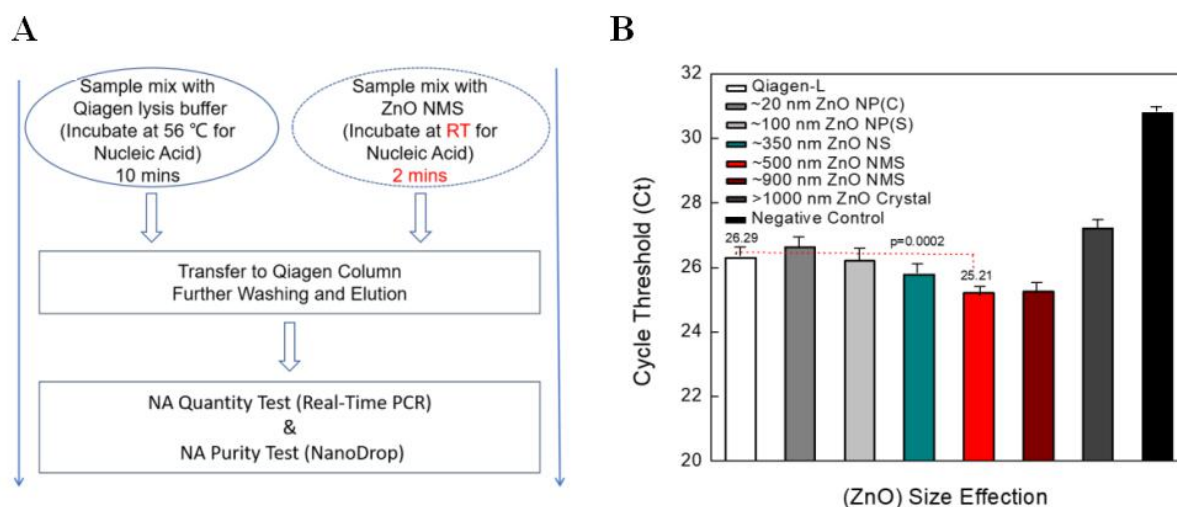


**Figure 1.1. 2. Usefulness of ZnO NMS for breaking the cell membrane.**

(A) The workflow for NA extraction with either ZnO NMS for cell lysis at RT for 2 min without detergent or spin column kit at 56 °C for 10 min with chaotropic detergent. (B) Comparison of DNA amplification efficiencies by real-time PCR depending on the size of ZnO NMS after NA extraction. Error bars indicate standard deviation from the mean, based on at least 3 independent experiments.

To further evaluate the usefulness of the ZnO NMS, we used other bacterial species including gram-positives (*Staphylococcus aureus* and *Bacillus cereus*) and gram-negatives (*Escherichia coli* and *Brucella ovis*) for DNA (Fig. 1.1.3.A) and RNA extraction (Fig. 1.1.3.B). The sample solution containing  $10^4$  CFU/mL was in the same volume of 100  $\mu$ L. We performed real-time PCR for the amplification of bacterial DNA from the spin column and ZnO NMS assays. We observed that the genes extracted from those bacteria using the ZnO NMS assay were strongly amplified. The enhancement of all samples using the ZnO NMS was statistically significant compared with those from the spin column assay (Fig. 1.1.3.A). In addition, we performed conventional PCR for amplification of bacterial RNA from the spin column kit (at RT for 10 min) and ZnO NMS (at RT for 2 min) assays. We showed that the quality and quantity of extracted RNA and the efficiency of amplification of RNA extracted from the ZnO NMS assay were comparable to that of the spin column assay.

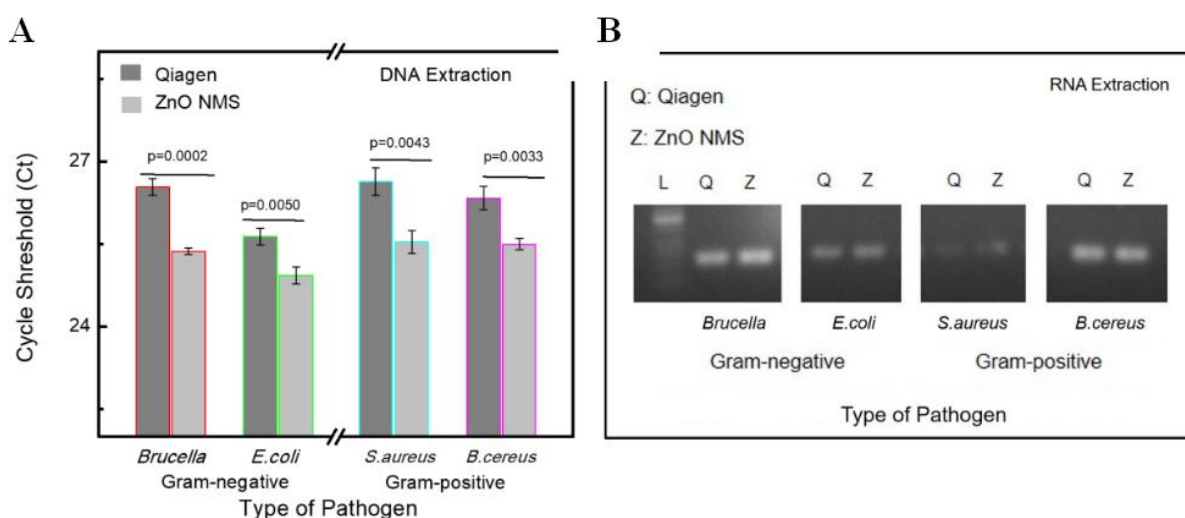


**Figure 1.1. 3. Application of ZnO NMS for lysis of prokaryotic cells.**

(A) Parallel experiments comparing the performance of the commercial kit with that of the ZnO NMS approach for analysis of bacterial DNA using real-time PCR at the same concentrations. (B) Parallel experiments comparing the performance of the commercial kit with that of the ZnO NMS approach for analysis of bacterial RNA using end-point reverse transcription PCR at the same concentrations.

Next, to investigate the usefulness of the nanomaterial in eukaryotic cells, HCT 116 cells were used with serially diluted samples containing 1 to  $10^4$  cells / 100  $\mu$ L for both DNA and RNA extraction. Using the optimized conditions of ZnO NMS, both genomic DNA and RNA were detected up to 1 cell / mL by real-time PCR. The detection limits of ZnO NMS were 100 times better for DNA and 10 times better for RNA than those of the spin column kit (Fig. 1.1.4). In addition, we compared the cell lysis efficacies of commercial ZnO NP (20 nm) and synthesized ZnO NMS. Genomic DNA and RNA were detected 1 to 1.5 cycles sooner via the ZnO NMS than with the ZnO NP (Fig. 1.1.4.A-B). The NA extraction products show a higher quantity and purity via ZnO NMS than via the spin column kit. Particularly, the quality and quantity of RNA extracted from ZnO NMS were quite high even with a low number of cells ( $3.5 \pm 2.3$  ng/ $\mu$ L and  $1.73 \pm 0.26$  at  $10^1$  cells/ 100  $\mu$ L). Based on the experimental results, the ~500 nm size of ZnO NMS with 0.05 mg/mL is selected for stable and superior performance of NA extraction. Taken together, the ZnO NMS can be used as a nanomaterial for rapid cell lysis without detergent at RT in various types of cells. This nanomaterial may be useful in a diagnostic system in a clinical setting.

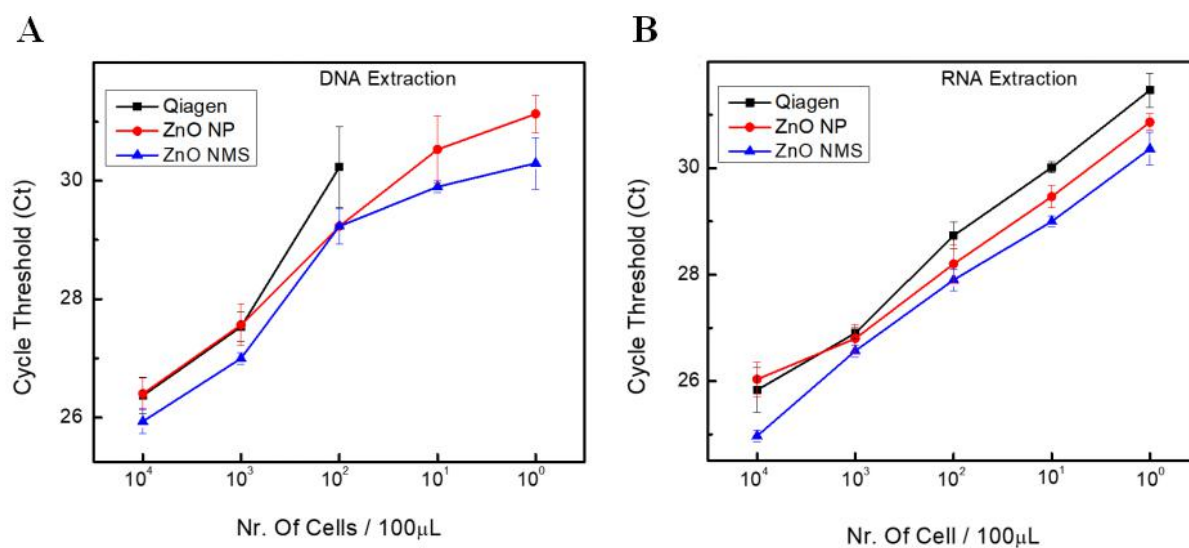


**Figure 1.1. 4. Application of ZnO NMS for lysis of eukaryotic cells.**

(A) Performance of the DNA extraction assay using either ZnO NMS, ZnO NP, or the spin column kit with a series of HCT 116 cell concentrations from 1 to  $10^4$  cells/ 100  $\mu$ L. (B) Performance of the RNA extraction assay using either ZnO NMS, ZnO NP, or the spin column kit with a series of cell concentrations from 1 to  $10^4$  cells/ 100  $\mu$ L by comparison of the cycle threshold (Ct) of real-time reverse transcription PCR. Error bars indicate standard deviation from the mean, based on at least 3 independent experiments.

### **1.(3-1).3 Usefulness of binary nanomaterials for sample preparation**

Based on the experimental results above, ZnO NMS (500 nm) is a good candidate for rapid cell lysis. However, an isolation and extraction technique for NA is needed with the rapid cell lysis system for use in a diagnostic system. Next, we applied ZnO NMS to the DDS technique for a large instrument- and detergent-free sample preparation (Fig. 1.1.5.A). Finally, to test the usefulness of the binary nanomaterial that couples ZnO NMS for sample preparation and the DDS technique for isolation and extraction of NA as a large instrument- and detergent-free sample preparation system, we compared the performances of sample preparation from the spin column based methods (chaotropic detergent) and binary nanomaterial assays (Fig. 1.1.5.B-C). In the case of DNA isolation and detection, DNA extracted from the binary nanomaterial assay was amplified sooner with a statistical significance at RT ( $p=0.0002$ ) than that of the spin column kit and chaotropic detergent assays (Fig. 1.1.5.B).



A

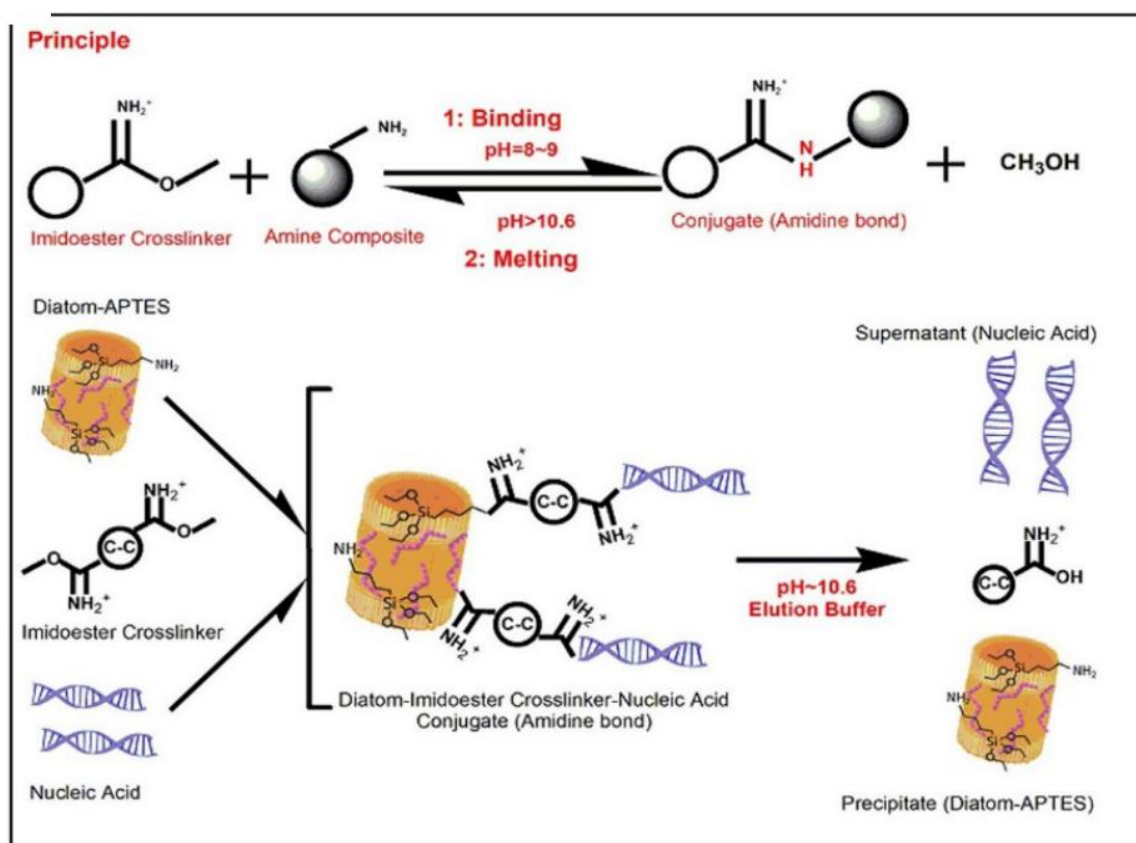


**Figure 1.1. 5. A Usefulness of binary nanomaterial for sample preparation.**

(A) The principle of DDS complex for capture and isolation of NA with ZnO NMS. The homobifunctional imidoester with specific amine groups is available to link to two primary amines from both diatom-APTES and NA in pH=8~9 simultaneously. Then, a high pH (10.6) would detach the interaction.

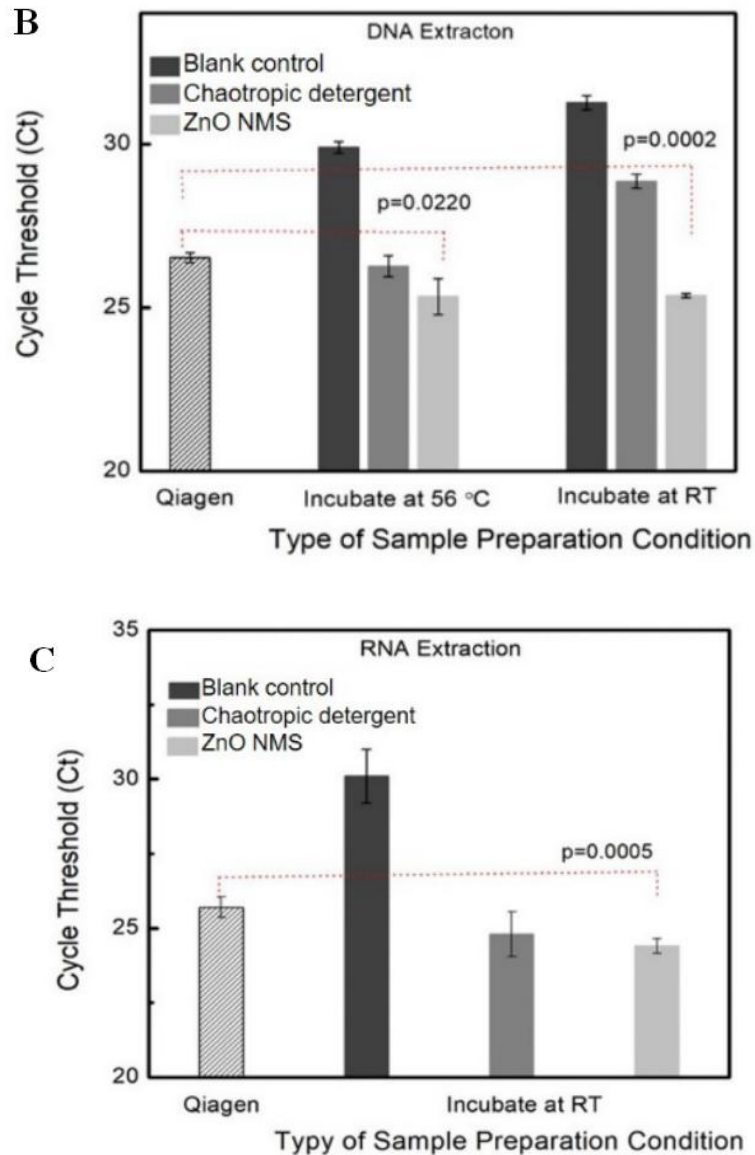


**Figure 1.1.5.B-C** Usefulness of binary nanomaterial for sample preparation. (B) Performance of the DNA extraction assay using the binary nanomaterial with *Brucella* (CFU:  $10^4$ ) by comparison of the cycle threshold (Ct) of real-time PCR from blank control with no lysis, chaotropic detergent incubated at 56 °C, and ZnO NMS at RT. (C) Performance of the RNA extraction assay using the binary nanomaterial with *Brucella* (CFU:  $10^4$ ) by comparison of the cycle threshold (Ct) of real-time PCR from blank control with no lysis, chaotropic detergent incubated at RT, and ZnO NMS at RT. Error bars indicate standard deviation from the mean, based on at least 3 independent experiments.

In addition, to test the detection limit of the binary nanomaterial in prokaryotic cells, *Brucella ovis* was used with serially diluted samples containing 10 to 10<sup>4</sup> cells/mL for DNA isolation and detection. The detection limit of the binary nanomaterial was found to be 10 times more sensitive than that of the spin column assay (Fig. 1.1.6.A, C). Next, in the case of RNA isolation and detection, RNA extracted from the binary nanomaterial assay was also amplified sooner with a statistical significance at RT ( $p=0.0005$ ) than that of the spin column and chaotropic detergent assays (Fig. 1.1.6.C). In addition, to test the detection limit of the binary nanomaterial in prokaryotic cells, *Brucella ovis* was used with serially diluted samples containing 10 to 10<sup>4</sup> cells/ 100  $\mu$ L for RNA isolation and detection. The detection limit of the binary nanomaterial was found to be 2 cycles sooner amplified than that of the spin column assay (Fig. 1.1.6.B, D). In Fig. 1.1.6.A and 1.1.6.B, the quantity of DNA/RNA extraction with a series dilution of *Brucella* (100  $\mu$ L, CFU: 10<sup>1</sup> to 10<sup>4</sup>) is shown. The large instrument- and detergent-free system exhibited a high quantity of NA extraction at a low concentration of cell, while the spin column kit was limited at 10<sup>2</sup> CFU for the DNA and RNA extraction, and the chaotropic detergent extractions were unstable at 10<sup>1</sup>. Taken together, the large instrument- and detergent-free assay for ultrasensitive nucleic acids isolation and detection via binary nanomaterial presented here requires less time (15 min), fewer processes, and no large instruments and could be applied to POCT in clinical settings.

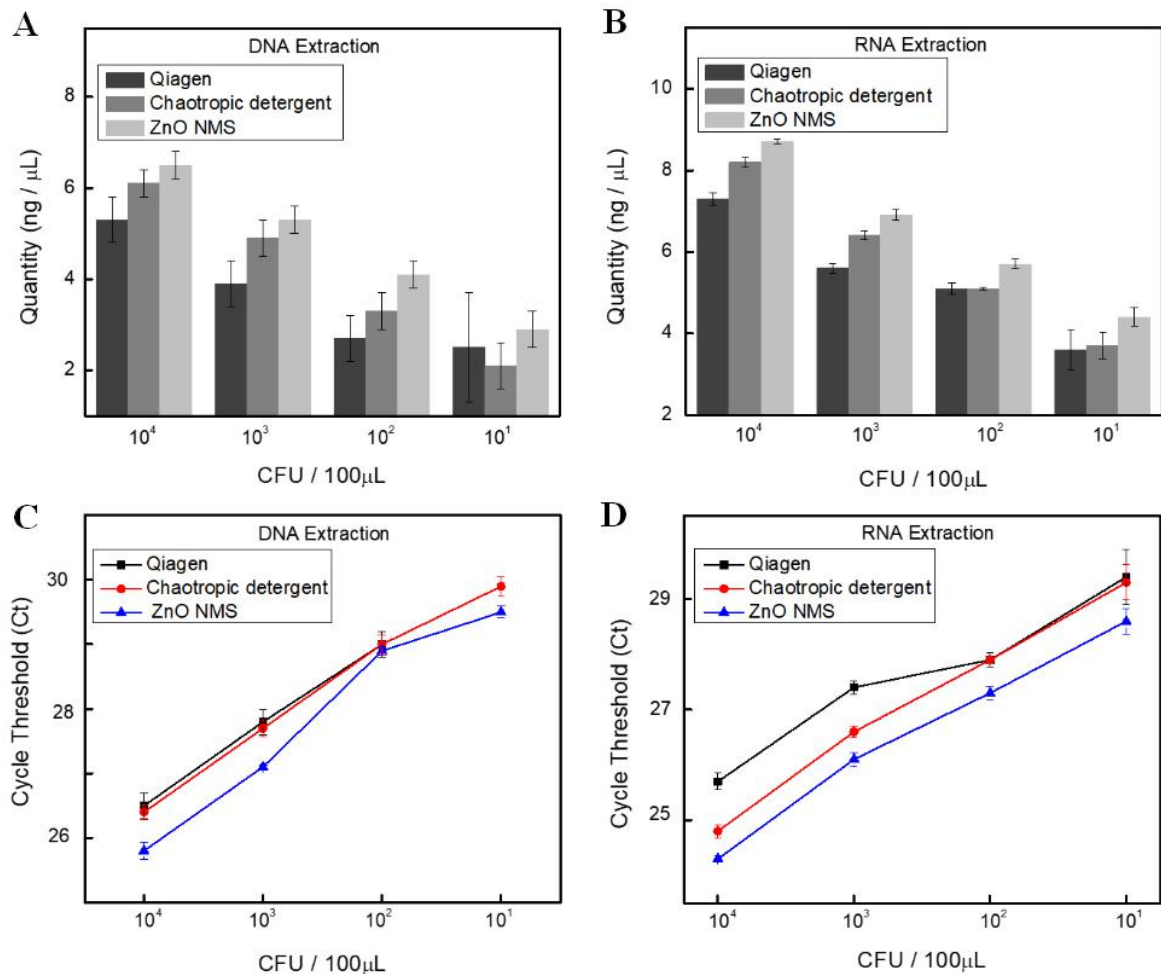


**Figure 1.1.6. Application of binary nanomaterial for nucleic acid isolation and detection.**

The quantity of DNA (A) and RNA (B) using the binary nanomaterial with a series of *Brucella ovis* from  $10^1$  to  $10^4$  CFU/ 100  $\mu$ L. (C) Performance of the DNA extraction assay using the binary nanomaterial by comparison of the cycle threshold (Ct) of real-time PCR. Error bars indicate standard deviation from the mean, based on at least 3 independent experiments. (D) Performance of the RNA extraction assay using the binary nanomaterial by comparison of the cycle threshold (Ct) of real-time reverse transcription PCR. Error bars indicate standard deviation from the mean, based on at least 3 independent experiments.

### 1.4.1 CONCLUSION

Here, in chapter 1 we report a large instrument- and detergent-free system for ultrasensitive nucleic acids isolation and detection via a binary nanomaterial, which couples a ZnO nano-multigonal shuttle (ZnO NMS) and a diatomaceous earth (diatom) with dimethyl suberimidate (DDS) technique. Using this proposed system, we have overcome the sample preparation and detection limitations of conventional point-of-care testing (POCT) systems, which require multiple instruments (thermal controller, centrifuge, and vortex), chaotropic detergent, and complex substrates (membrane/filter). First, we used an economical method for synthesis of ZnO NMS with uniformity and size control. The ZnO NMS showed a clear growth route in the surfactant and was developed from particles, resulting in a single shuttle and finally a multi-shuttle. As ZnO nanomaterials are produced in large quantities for both diagnostic and therapeutic clinical applications, we would expect more education and information on their use and nature, and it is important to motivate communities to study their safety. ZnO nanomaterials have been shown to bind biomolecules in desired orientations and improved conformations and produce high biological activity, resulting in enhanced sensing characteristics. Furthermore, their compatibility with complementary metal-oxide-semiconductor technology for construction of integrated circuits makes them a suitable candidate for future small integrated biosensor devices. The use of a ZnO nanomaterial for sample preparation results in strategic progress for NA extraction and downstream detection. ZnO nanoparticles (<20 nm) have been used for DNA extraction with chaotropic detergent. However, the efficiency of DNA extraction is lower than that of commercialized methods. Second, we validated the synthesis of 500-nm ZnO NMS for cell lysis without any detergent at RT within 2 min. The performance of the ZnO NMS was 100 times higher than that of the spin column kit. Third, we used a DDS technique for isolation and extraction of NA from both eukaryotic and prokaryotic cells without the use of chaotropic reagents. Fourth, we used a binary nanomaterial that coupled the synthesized 500-nm ZnO NMS and the DDS technique for ultrasensitive nucleic acids isolation and detection. Using the

binary nanomaterial, the detection limit was 10 times more sensitive than that of the spin column kit. Fifth, this binary nanomaterial system isolated and detected NA with high sensitivity and speed (<15 min). Lastly, this system does not require instrumentation for thermal incubation, centrifugation, and complex washing to remove chaotropic detergent and offers a possible POCT system for developing countries. Although this system still requires hand-on time and small device, it has many advantages compared to the spin-column method. The system is amendable for use in microfluidic system for subsequently building point-of-care testing system. Further evaluation studies for an optimal system would be needed for large clinical samples. We believe that this binary nanomaterial system would be a useful tool for rapid and sensitive nucleic acids isolation in the field of immediate molecular diagnostics.

## **CHAPTER 2 Dimethyl 3, 3'-dithiobispropionimide (DTBP) as a cleavable disulfide-based polymer to encapsulate nucleic acids in biological sample preparation**

### **1.(3-2).1 Biomolecule encapsulation by DTBP**

In recent decades, many substances have been investigated for biomolecule encapsulation.[14] Herein, we used amine-coated diatomaceous earth (DA) as a solid substance that could support large surface areas with many more selective amine groups (Fig. 1.2.1.A). To encapsulate biomolecules, homobifunctional imidoester cross-linkers (HI) including DMS, DMA, DMP, and DTBP, were used to link pairs of primary amines from DA and target biomolecules. Binding and melting properties of HIs are presented in Fig. 1.2.1.B as isoelectric points. For biological amphoteric groups, such as  $\text{NH}_2^+$ , net charge is affected by pH, and at pH 8–9 HIs with specific amine groups form amidine bonds with amines from bio-amine composites. The resulting conjugated amidine bonds then melt and release amine composites at high-pH (over 10.6). Among HIs, DTBP only contains disulfide bonds in its structure (Fig. 1.2.1.C). These reversibly cross-linked disulfide bonds can be cleaved even by mild reductants, and hence, DTBP can be used to overcome previous difficulties in nucleic acid encapsulation and elution for applications to disease diagnostics. We compared the abilities of DTBP (Figure 1.2.1.C-C2) and DMS (Figure 1.2.1.C-C1) to cross-link during sample preparation for disease diagnosis.

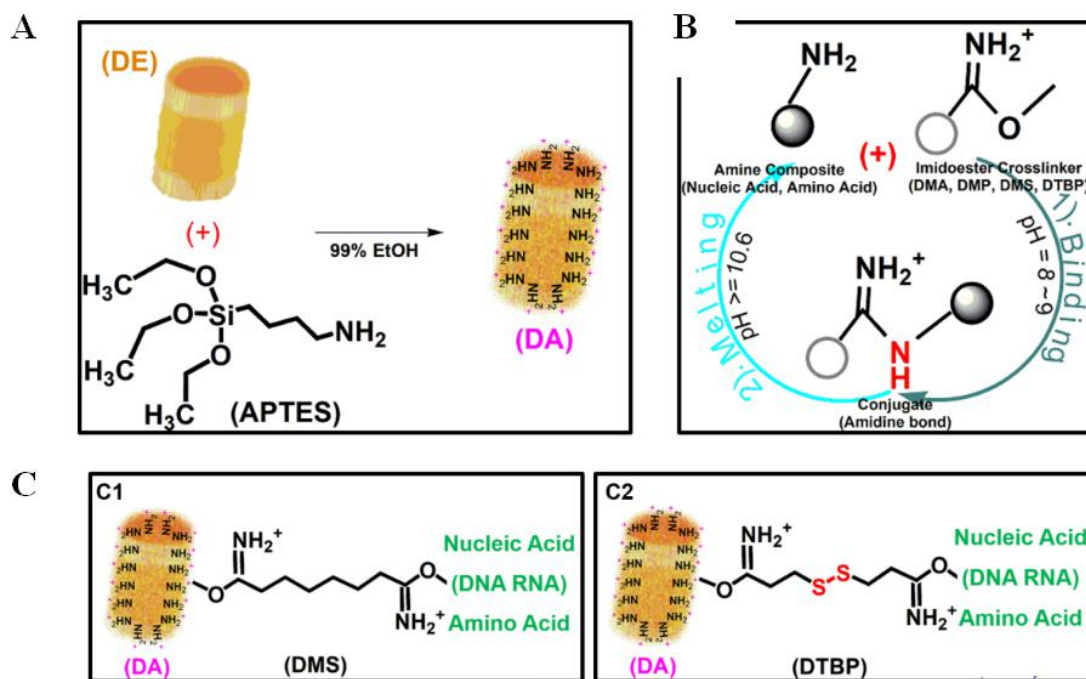


**Figure 1.2.1. Schematic representation of the principle of nano-composites with cleavable disulfide bond cross-linkers as an effective binding–melting strategy to improve solid-phase based nucleic acid extraction from biomedical samples**

(A) amine group functionalization via APTES on diatomaceous earth (DE) produces Diatom-APTES (DA) at room temperature under anti-hydrolysis (99% EtOH) conditions; (B) the principle of imidoester cross-linkers with specific amine groups; the two primary amines from both DA and bio-amine composites are linked at pH = 8–9 (binding) and melted at pH 10.6. (C) Two representative cross-linkers were compared in terms of nucleic acid extraction with the respective nano-composites. (C1) DMS is a non-cleavable disulfide system. (C2) DTBP provides a cleavable disulfide system.



### **1.(3-2).2 Characterization of DA and DTBP composite systems**

To optimize the protocol for coating diatom surfaces with amine groups, amine functionalization conditions, such as concentration, reaction time, and temperature, were examined as shown in Fig. 1.2.2.A. No encapsulation of nucleic acid was observed with diatoms lacking amine group coating, indicating that the pure diatom (DE) without selective amine groups fail to extract nucleic acids. We selected conditions with 2% amine coating of diatoms (DA) at room temperature for 60 min. Under chaotropic-agent based cell lysis conditions at 56 °C for 30 min (Fig. 1.2.2.B), we compared nucleic acid isolation and purification with DA and DTBP composite systems at various DE and DA contents cell concentrations (Fig. 1.2.2.C-D). DNA from RT-qPCR reactions was quantified using cycle threshold (Ct) values. In these experiments, lower fractional cycle numbers indicated that the earlier fluorescence passes the fixed threshold quantity of extracted nucleic acids. In Fig 2C, the obvious quantities of DNA in the DA-DTBP AD-HI system suggested that homobifunctional imidoester cross-linkers easily bind amine groups. We also compared DNA extraction efficacy using either a spin column kit (Qia-kit) or a DA-DTBP composite system with diluted cell concentrations to  $10^1$ – $10^6$  cells in 100- $\mu$ L (Fig. 1.2.2.D). The detection limit of the DA-DTBP composite system was 100 times more sensitive than that of the Qia-kit.

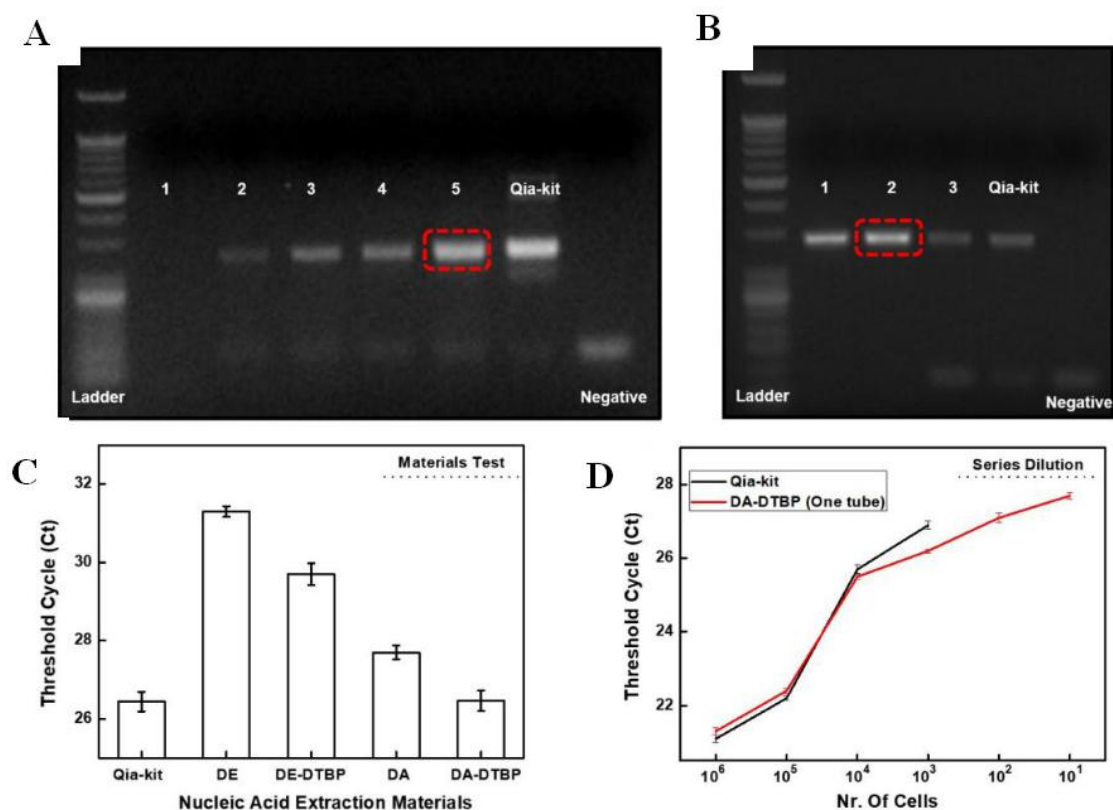


**Figure 1.2.2. Characterization of amine-modified diatom earth (DA) and DTBP composite systems**

(A) amine-modified conditions on DE via APTES; 1, 0% APTES at 65 °C for 60 min; 2, 1% APTES at 65 °C for 60 min; 3, 1% APTES at RT for 60 min; 4, 2% APTES at 65 °C for 60 min; 5, 2% APTES at RT for 60 min; Qia-kit, positive control using commercialized Qiagen kit and negative control. (B) Incubation times for cell lysis reactions; 1, 10 min; 2, 30 min; and 3, 60 min. (C) Comparison of amplification efficiencies in real-time PCR using DNA from 116 HCT cells with the following combinations: DE, diatom earth only; DE-DTBP, diatom earth with DTBP; DA, amine-modified diatom earth only; DA-DTBP, amine-modified diatom earth with DTBP; and Qia-kit. Error bars indicate standard deviations of the mean and were calculated from at least 3 independent experiments. (D) DNA extraction assays using the Qia-kit or DA-DTBP composite system at varying HCT 116 cell concentrations between  $10^1$  and  $10^6$  cells/100  $\mu$ L ( $10^0$ - $10^5$ ); comparison of cycle threshold (Ct) values for real-time PCR. Error bars indicate standard deviations from the mean and were calculated from at least 3 independent experiments.

### 1.(3-2).3 DA-DTBP composite in ZnO NMS systems

In contrast with other HIs, the disulfide bonds of DTBP can be cleaved by reduction (SDS) during cell lysis using chaotropic reagents. We replaced the chaotropic detergent with the semi-conductor ZnO NMS (Fig. 1.2.3.A) so that the cleavable disulfide bonds were protected and the cleaved disulfide bonds could be repaired under oxidative conditions (Fig. 1.2.3.B), which were achieved using a reactive oxygen species (ROS) generating system. ZnO NMS with the special band gap that protected the disulfide bond of DTBP resulted in an oxidative environment (Fig. 1.2.3.B). Briefly, when semiconductor materials absorb energy ( $E_i > E_g$ ), electrons are promoted from the valence band (VB) to the conduction band (CB). This results in the generation of holes ( $h^+$ ) in the valence band and free electrons ( $e^-$ ) in the conduction band. These hole-electron pairs can interact with  $H_2O$  or  $O_2$  to generate reactive oxygen species (ROS) such as superoxide anions ( $O_2^{\bullet-}$ ) and hydroxyl radicals ( $\cdot OH$ ). To determine disulfide bond effects of DTBP in ZnO NMS, we performed chemical-optical Fourier transform infrared (FTIR) spectral analyses. The absorption peak at  $2550\text{ cm}^{-1}$  in the red line is ascribed to the S-H thiol and confirmed that the disulfide bond was cleaved in the chaotropic lysis system (Fig. 1.2.3.C). In the ZnO NMS assistant system, the disulfide bond of DTBP was protected as for DTBP alone, as indicated by comparisons of the performance of DA-DMS (non-cleavable) and DA-DTBP (cleavable) in ZnO NMS assisted systems (Fig. 1.2.3.D). Fluorescence signals in RT-PCR analyses of DNAs extracted from *Escherichia coli* using DA-DMS and DA-DTBP systems are shown in Fig. 1.2.3.E. These data show that DNAs that were extracted from DA-DMS using lysis buffer had lower Ct values than those from DA-DTBP with lysis buffer. In contrast with the DA-DMS system, chaotropic detergent effects in the DA-DTBP system indicated that the chaotropic detergent may break typical reduction-sensitive disulfide bonds of DTBP and reduce the efficiency of DNA linking. Taken together, we confirmed that the disulfide bond of DTBP was easily cleaved by the reducing substance, leading to decreases in yields of nucleic acid.

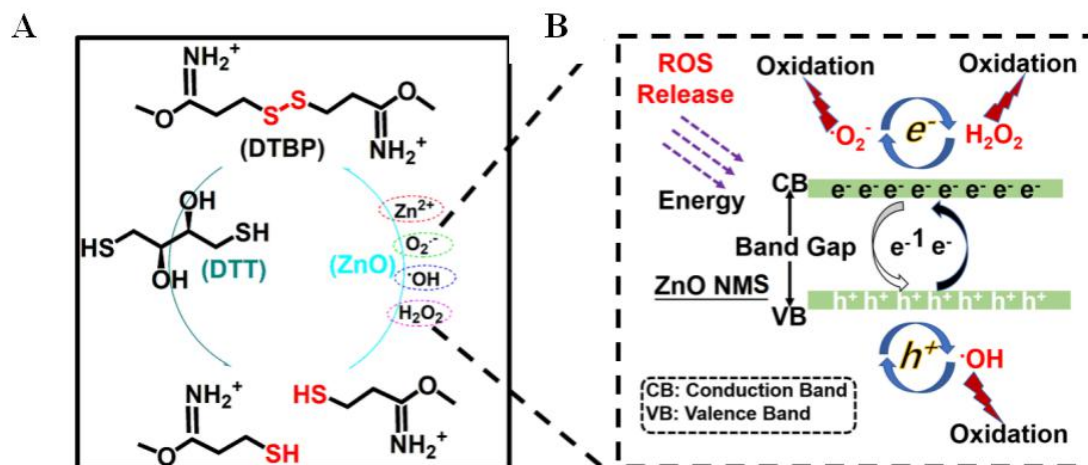


**Figure 1.2.3. The DA-DTBP composite in the ZnO nanomultigonal shuttle (ZnO NMS) system as a substitute for chaotropic reagents**

(A) The scheme of cleavable disulfide bond of DTBP be cleaved by DTT and protected under oxidative conditions. (B) Oxidative conditions were provided by zinc oxide nanomaterials in the multigonal shuttle structure (ZnO NMS).

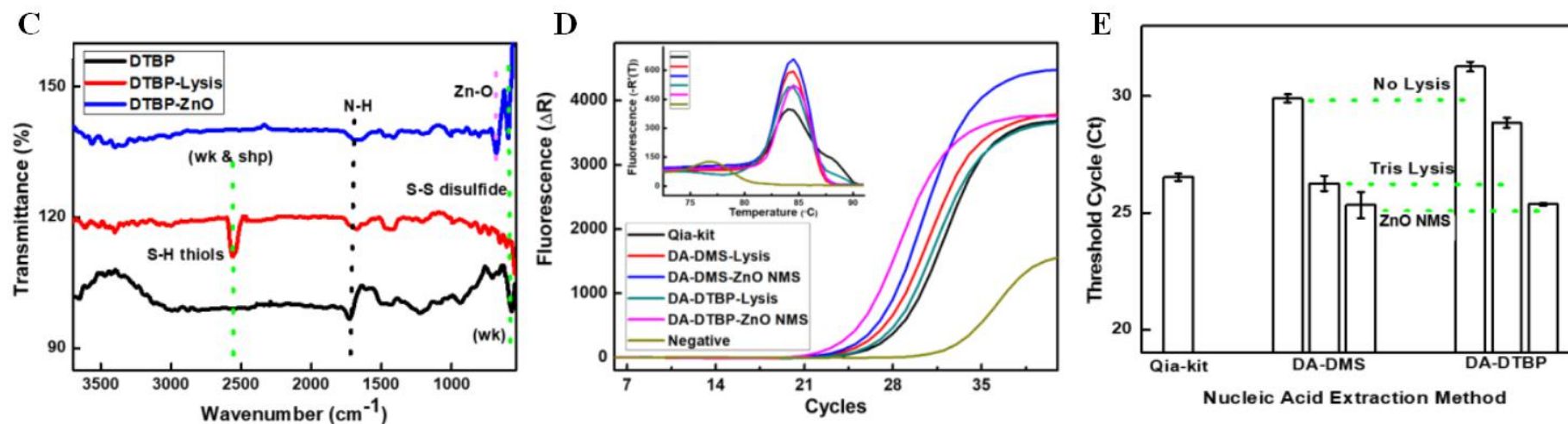


**Figure 1.2.3. The DA-DTBP composite in the ZnO nanomultigonal shuttle (ZnO NMS) system as a substitute for chaotropic reagents**

(C) FTIR analysis of DTBP only, DTBP with lysis buffer, and DTBP with ZnO NMS (wk = weak, shp = sharp, Standard abbreviations to describe the absorption bands). (D) Fluorescence signals in real-time PCR analyses of amplified DNAs that were extracted from *Escherichia coli* using DA-DMS and DA-DTBP composite systems; the inside figure shows melting-curve plots representing amplification products from the systems. (E) Comparison of non-cleavable DA-DMS and cleavable DA-DTBP systems with and without ZnO NMS; error bars indicate standard deviations from the mean and were calculated from at least 3 independent experiments.

#### **1.(3-2).4 Application of DA-DTBP composites to the ZnO NMS system**

To determine the performance of DA-DTBP composites in ZnO NMS systems, we used them to extract DNA from gram-positive (*Staphylococcus aureus*) and gram-negative (*Salmonella*) pathogens (Fig. 1.2.4.A). In experiments using the DA-DTBP composite in the ZnO NMS system, Ct values were much lower than those from experiments using commercial spin column-based reference kits. We also confirmed that the reversibly cross-linked disulfide bond in ZnO NMS released sufficient quantities of ROS and Zinc ions to result in cell lysis[14]. Subsequently, we used this system to extract RNA from prokaryotic (*Brucella*) and eukaryotic (*HCT 116*) cells (Fig. 1.2.4.B) and showed that the DA-DTBP composite in the ZnO NMS system was stable and led to higher efficiency RNA extraction than the other methods (Fig. 1.2.4.B).

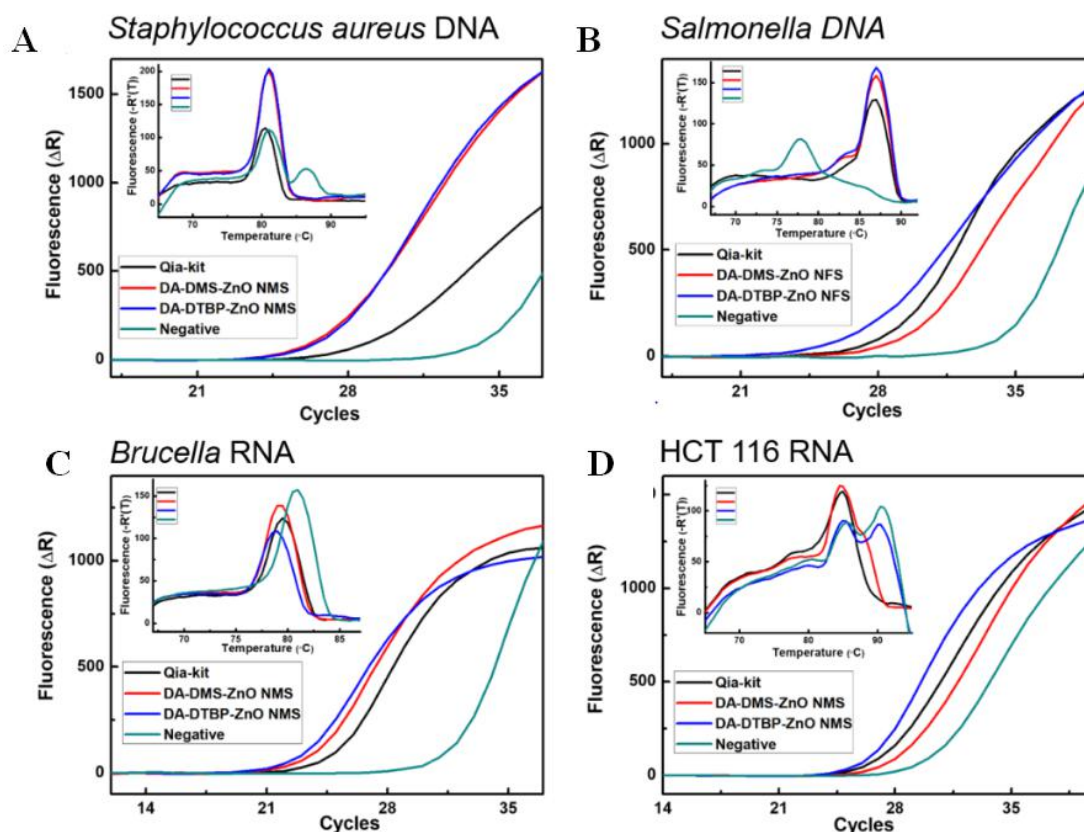


**Figure 1.2.4. Application of DA-DTBP composites in the ZnO multigonal shuttle system.**

Fluorescence signals from real-time PCR analyses of amplified DNAs and RNAs that were extracted from gram-positive bacteria, gram-negative bacteria, and human cells using DA-DMS and DA-DTBP composite systems; (A-B) DNA was extracted from *Staphylococcus aureus* (A) and *Salmonella* (B). (C-D) RNA extraction from *Brucella* (C) and HCT 116 cells (D). The inside figure shows melting-curve plots of amplification products from the systems.

### **1.(3-2).5 NA release from cleavable disulfide cross-linkers**

Alkaline-pH (over 10.6) salts have been used to release nucleic acids from nanoparticle systems, but the potential for degradation of extracted nucleic acids can hamper downstream analyses. Thus, we used dithiothreitol (DTT,  $C_4H_{10}O_2S_2$ ) to break disulfide bonds (S-S) of DTBP and release nucleic acids (Fig. 1.2.4). To determine whether redox-neutral DTT releases nucleic acids from the DTBP cross-linker, we performed experiments with DTT at  $10^{-1}$ – $10^{-4}$  mol and then selected optimal conditions that did not inhibit PCR (Fig. 1.2.5.A). At  $10^{-3}$ -mol, DTT did not inhibit DNA amplification. We also tested DTT at pH 10.6, 9.4, and 8.6 after adjustment with  $NaHCO_3$ , but show no differences in DNA extraction between pH conditions (Fig. 1.2.5.B). To investigate whether salts in the elution buffer shield negative charges and neutralize decreases in DNA repulsion and stabilization, we performed experiments after adjusting DTT solutions to pH 7–8 using the sodium salts  $NaHCO_3$ , NaAc, and NaCl. These experiments showed the best results after pH adjustments using NaCl (Fig. 1.2.5.C). Finally, we investigated the efficacy of DTT as a nucleic acid releasing agent in DA-DMS (non-cleavable) and DA-DTBP (cleavable) ZnO NMS assistant systems (Fig. 1.2.5.D). DTT facilitated the ZnO NMS assistant system in the presence of DA-DTBP but not in the presence of DA-DMS. Therefore, we selected DA-DTBP in the ZnO NMS assistant system as a polymer for rapid and simple disulfide-based encapsulation and release of nucleic acids.



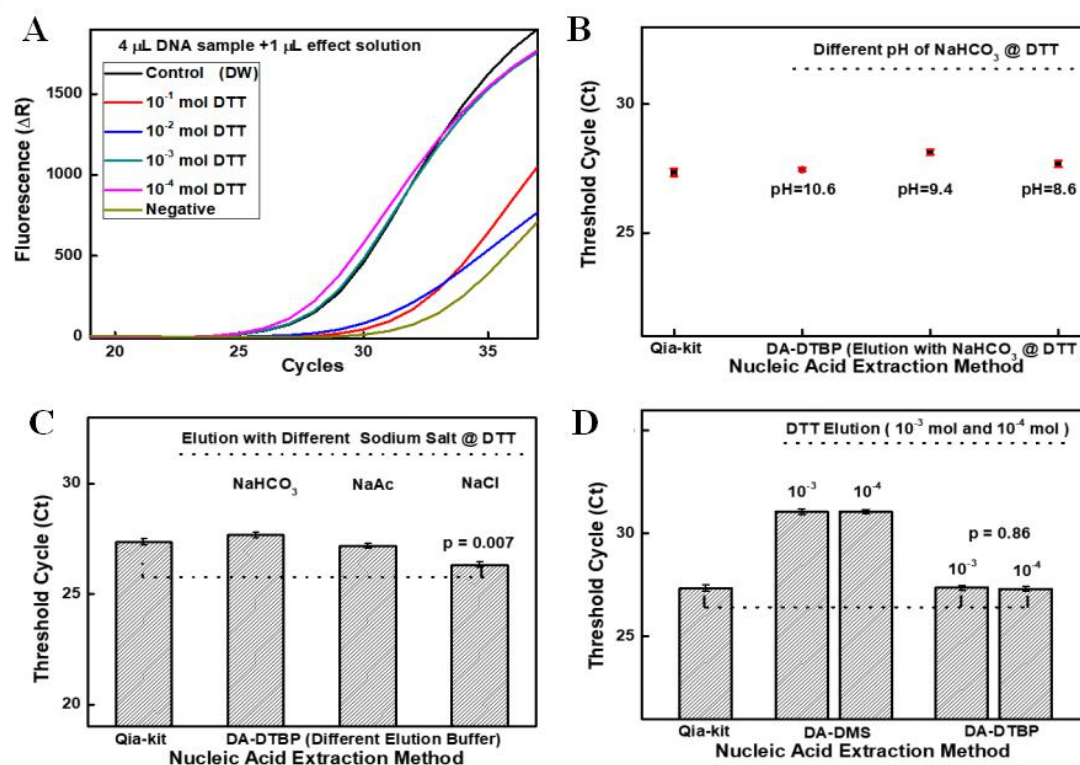


**Figure 1.2.5. Nucleic acid release from the cleavable disulfide cross-linker;** (A) optimal concentrations of DTT that do not inhibit PCR. (B) pH (pH 10.6, 9.4, and 8.6) of DTT; error bars indicate standard deviations from the mean and were calculated from at least 3 independent experiments. (C) Effects of the sodium salts  $\text{NaHCO}_3$ ,  $\text{NaAc}$ , and  $\text{NaCl}$  in combination with DTT on the release of nucleic acids; error bars indicate standard deviations from the mean and were calculated from at least 3 independent experiments. (D) Comparison of releasing nucleic acid release with DTT in the present systems; DA-DMS was non-cleavable system and DA-DTBP is a cleavable system. Error bars indicate standard deviations from the mean and were calculated from at least 3 independent experiments.

## 1.4.2 CONCLUSION

In chapter 2, we report the first novel functionalization scheme using nano-composites to afford nucleic acid capture and release using DTBP as a cleavable disulfide bond based cross-linker for biological applications. Under the conditions of our experiments, the efficiency of sample preparation for disease diagnostics was improved by various adjustments. First, conjugates of amine-modified diatomaceous earth (DA) and DTBP formed stable suspensions with chaotropic reagents without the need for sophisticated instruments. Second, conjugation with ZnO NMS led to good cell lysis without additional reagents and maintained cleavable disulfide linkages between nucleic acids and DA surfaces, reflecting protection of disulfide bonds of DTBP by the semi-conductor ZnO NMS under oxidative conditions. Third, the cleavable disulfide bond of DTBP was cleaved easily by DTT at pH 7 in the absence of inhibitors such as salts and SDS, and the extracted nucleic acids were suitable for downstream analysis. The present cleavable functionalization scheme for biomolecules could be used for transportation of nucleic acids in diagnostic applications. Our findings give a new insight into stimuli-responsiveness of disulfide bonds and provide the foundation for further developments of the novel redox-responsiveness of DTBP in human disease diagnostic and drug delivery systems.

## **CHAPTER 3 A Sample Preparation Technique Using Biocompatible Composites for Biomedical Applications**

### **1.(3.3).1 Design and principle of the CB-DA biocompatible composite**

As we reported in our previous study, cucurbituril-based diatom composites (CB-DA) exhibit a strong host-guest interaction that supports molecular encapsulation. An efficient method for fabricating CB-DA to diagnose pathogen is proposed in this study. By examining the DE using scanning electron microscopy (SEM; JEOL JSM-7500F, Tokyo, Japan) and dynamic light scattering (DLS, DynaPro NanoStar, Wyatt), we confirmed that the size of the DE particles was well distributed between 10 and 20  $\mu\text{m}$ , an appropriate size range for this project. (Fig. 1.3.1.A-B). APTES (3-aminopropyl-triethoxysilane)-modified DE (also known as DA) has an enhanced pathogen enrichment property. Here, we focus on DE surface medication with the similar chemical diethyl amino polydimethylsiloxane (APDMS (3-aminopropyl-methyl-diethoxysilane)). The structural formula of APDMS is shown in Fig. 1.3.1.C, and the chain length of the organic amino compound can be seen. A diagram of cucurbit[6]uril with a portal diameter of 3.9 Å, a cavity diameter of 5.8 Å, and a height of 9.1 Å is shown in Fig. 1.3.1.D.

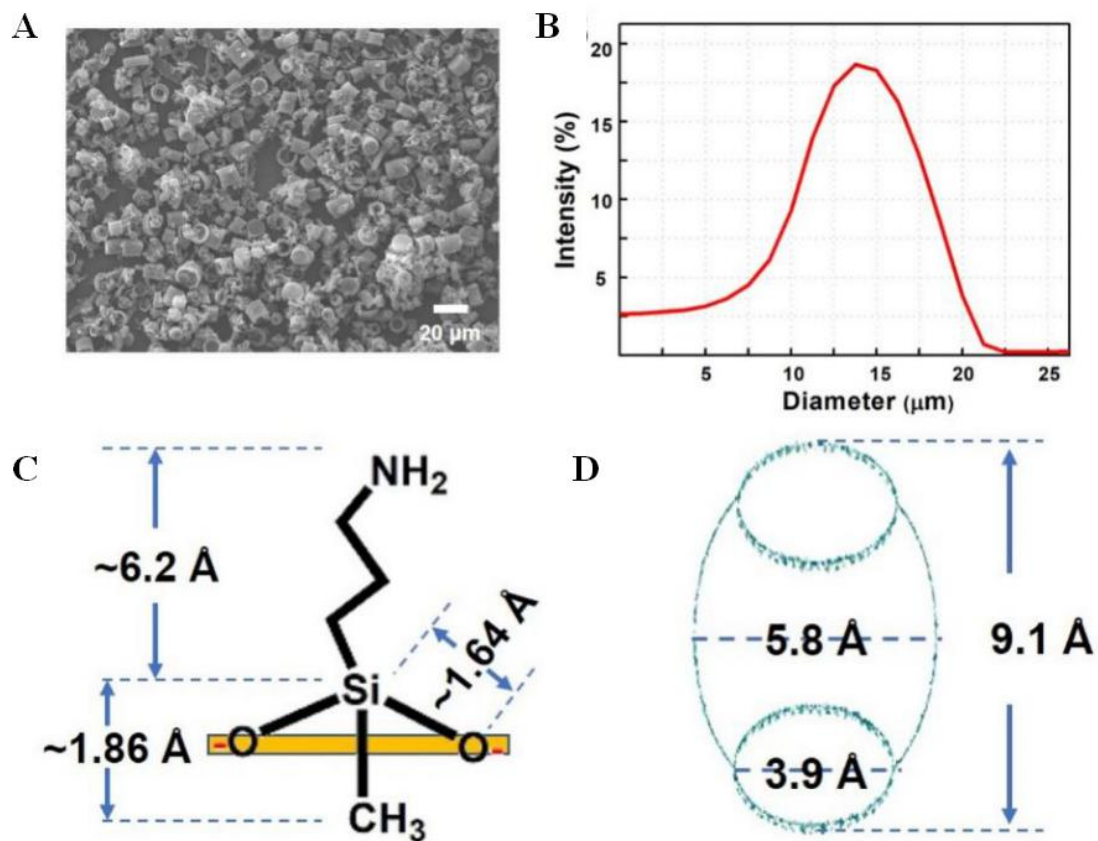


**Figure 1.3.1. Characterization of the studied materials.**

A: SEM image of DE. B: DLS analysis of the size distribution of the DE. C: Short chain length of amino organic compound (3-aminopropyl-methyl-diethoxysilane). D: Diagram of cucurbit[6]uril, portal diameter (3.9  $\text{\AA}$ ), cavity diameter (5.8  $\text{\AA}$ ), and height (9.1  $\text{\AA}$ ).

### 1.(3.3).2 Preparation and characterization of DA

A schematic of the process flow for amino functionalization of diatomaceous earth (DA) with different chemicals is shown in Fig. 1.3.2.A. The diethyls of APDMS is differences from the triethyls of APTES for the surface modification of materials. Two points of the bonding site from the APDMS is expected to be more efficiency on bonding than APTES with three points (Fig. 1.3.2.A). The surface charges of the composites (reported as the zeta potential) were measured to estimate the efficiency of the amino modification (Fig. 1.3.2.B-C). Pure DE exhibited a negative surface charge. Amine groups surrounding the inner and outer surfaces of the DE skeleton can enhance its chemical stability, allow it to be used for extended periods of time, and lead to a robust coating with saline via covalent bond formation. Serial doses of APDMS or APTES, ranging from 50  $\mu$ L to 400  $\mu$ L, were added to 500  $\mu$ L (100 mg/mL) of DE. The zeta potentials shown in Fig. 1.3.2.B and C show that a modification ratio of 1:2 (250  $\mu$ L into 500  $\mu$ L of DE) led to good modification efficiency for both APDMS and APTES. Overall, APDMS modification was more efficient than APTES modification under the same conditions, perhaps due to differences in the contact surface area of the molecules. Modification with APDMS (which contains diethyl groups) requires two sites, while modification with APTES (which contains triethyl groups) requires three sites. To optimize the APDMS modification time (Fig. 1.3.2.D), the modification reaction was monitored from 30 to 180 mins. Here, the modification ratio at 1:2 (250  $\mu$ L into 500  $\mu$ L DE) was studied to measure optimization of the APDMS modification time. Notably, we referred the reported APTES modification procedure, 120 mins incubation (modification) time has been fixed on the dosage studies. A modification time of 90 mins was chosen for use in the fabrication process. Taken together, these results show that APDMS modification resulted in the presence of two free chains on the DA surface that could be involved in additional linkages.

A

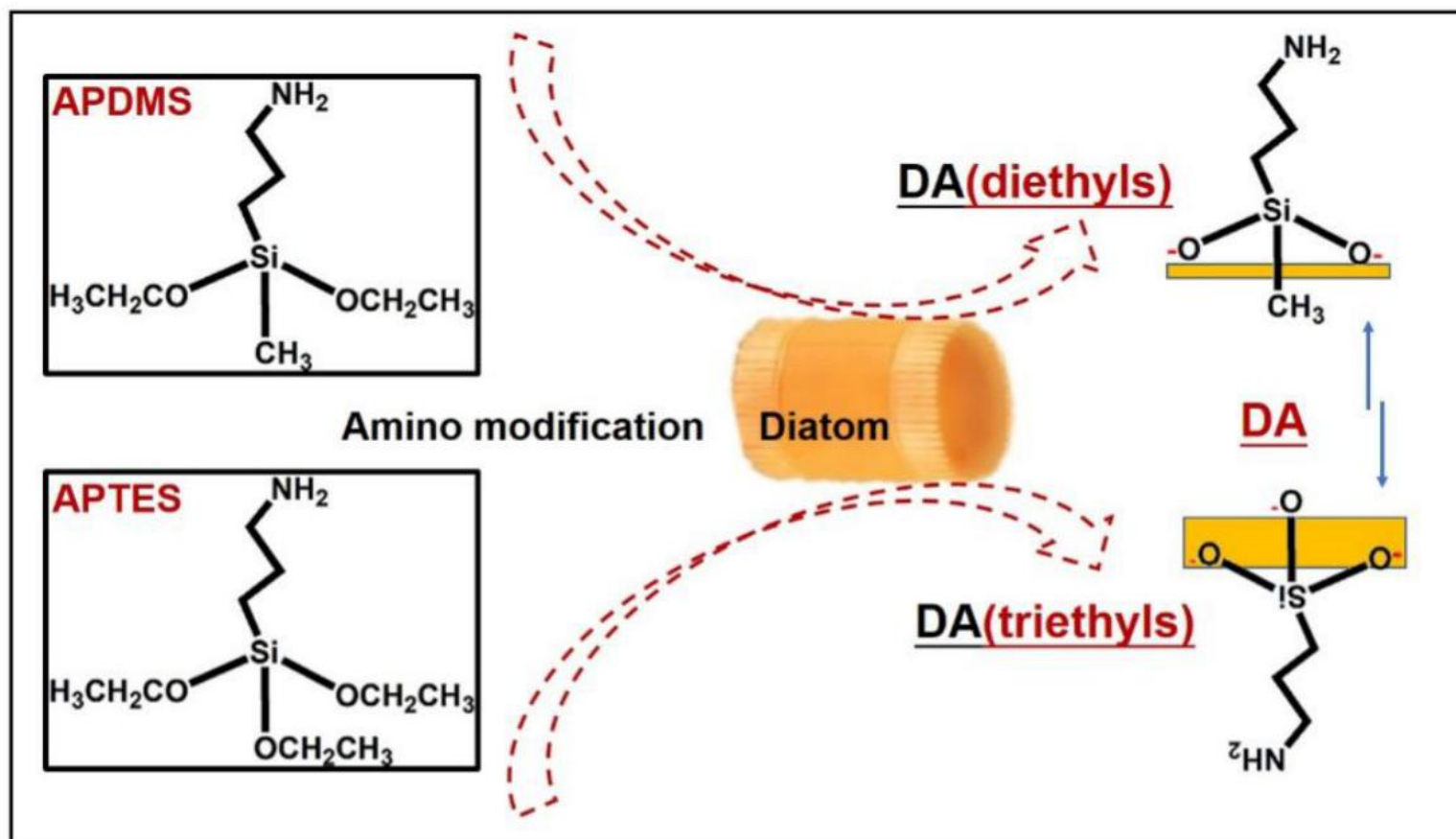


**Figure 1.3.2. (A) Schematic of the process flow for amino functionalization of diatomaceous earth (DA)**The diatom substrate was modified with APDMS or APTES

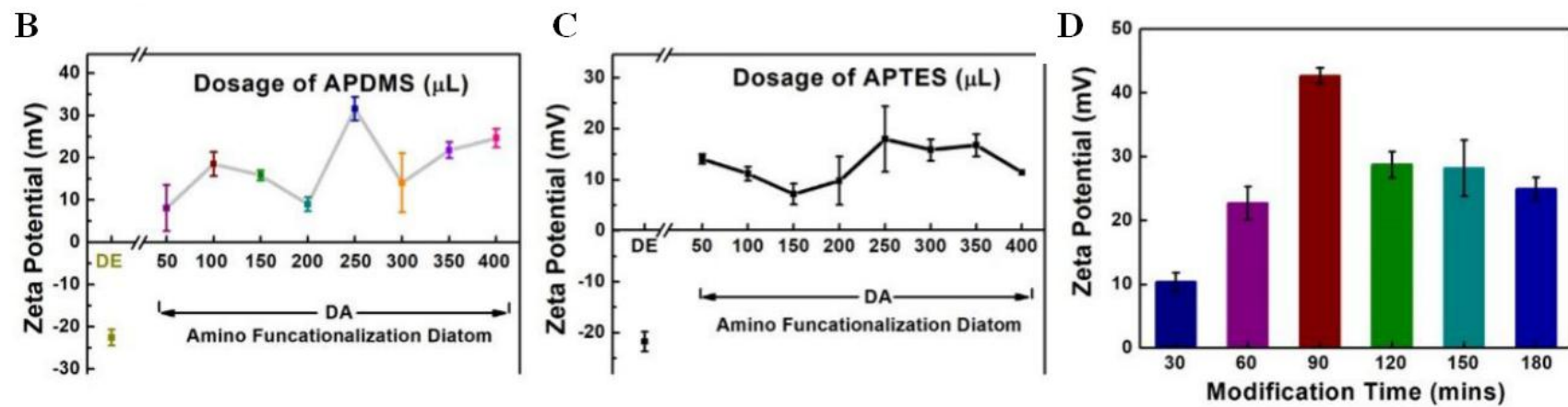


**Figure 1.3.2. Schematic of the process flow for amino functionalization of diatomaceous earth (DA).** (B-C) Optimized conditions for amino functionalization of DE via APDMS (diethyls) and APTES (triethyls). Doses ( $\mu\text{L}$ ) of APDMS and APTES reacted with  $500 \mu\text{L}$ ,  $50 \text{ mg. L}^{-1}$  DE in  $1.5 \text{ mL}$  tubes for 120 mins. (The volume ratios ranged from 1/11 to 8/18.) APDMS or APTES ( $50$  to  $400 \mu\text{L}$ ) was tested serially. (D) Optimization of the APDMS modification time. The zeta potentials of DA products with different APDMS modification times ranging from 30 to 180 mins

### 1.(3.3).3 Preparation and characterization of CB-DA

A schematic representation of cucurbituril coating of APDMS-modified DE (CB-DA) is shown in Fig. 1.3.3.A. The two free chains of the APDMS on the substrate are encapsulated in the cavity of the CB, which is a key property of this second DE surface modification. Chemical-optical spectrum analysis of the composites was performed to assess the modification status. SEM images were used to assess the morphology of the DE and CB-DA, as shown in Fig. 1.3.3.B. The pores on the DE surface are open, and the pore diameter is less than 100 nm (Fig. 1.3.3.B, top). However, the CB-DA is rougher with blocked pores on the surface (Figure 3B, bottom). To assess the electrostatic properties of the CB-DA in solution, the zeta potentials of the CB-DA were measured (Fig. 1.3.3.C). Because of the uniform size of the DE particles, we ignored the size effect of the surface charge. Notably, the zeta potential of the CB-DA composite was higher than that of the DA, likely reflecting the diverse anchor bindings between the DA and CB, which may include the reported possible anchor linking/ion-dipole interaction between the carbonyl groups of the CB portals. Furthermore, the positively charged amine groups in the CB-DA composite could enhance the absorbency efficiency of the CB-DA conjugate during its interaction with other molecules via enhanced covalent bonding, physical adsorption, electrostatic interaction, and heterogeneous surface binding. In the Fourier-transform infrared (FTIR) spectrum analysis of the composite (Fig. 1.3.3.D), the absorption peak at  $1450\text{ cm}^{-1}$  was attributed to asymmetric stretching vibrations in the Si–O–Si bonds, and the peak at  $1410\text{ cm}^{-1}$  resulted from the Si–CH<sub>2</sub> bond (black curve). In addition, the absorption peaks at  $3295$  and  $1180\text{ cm}^{-1}$  can be attributed to Si–OH and C–N bonding, respectively, on the surface of the pure DE. After the surface modification to form DA, the well-defined absorption bands at  $1100$ ,  $2250$ , and  $2720\text{ cm}^{-1}$  represent C–C–C bonding, C–H bonding, and O–H bonding, respectively. The stretching vibrations at  $2850$ – $3000\text{ cm}^{-1}$  from the CH, CH<sub>2</sub>, and CH<sub>3</sub> groups and that at  $2720\text{ cm}^{-1}$  from the aldehyde (C–H) in the CB-DA group (blue curve) verified the presence of a CB-DA supermolecule.



A

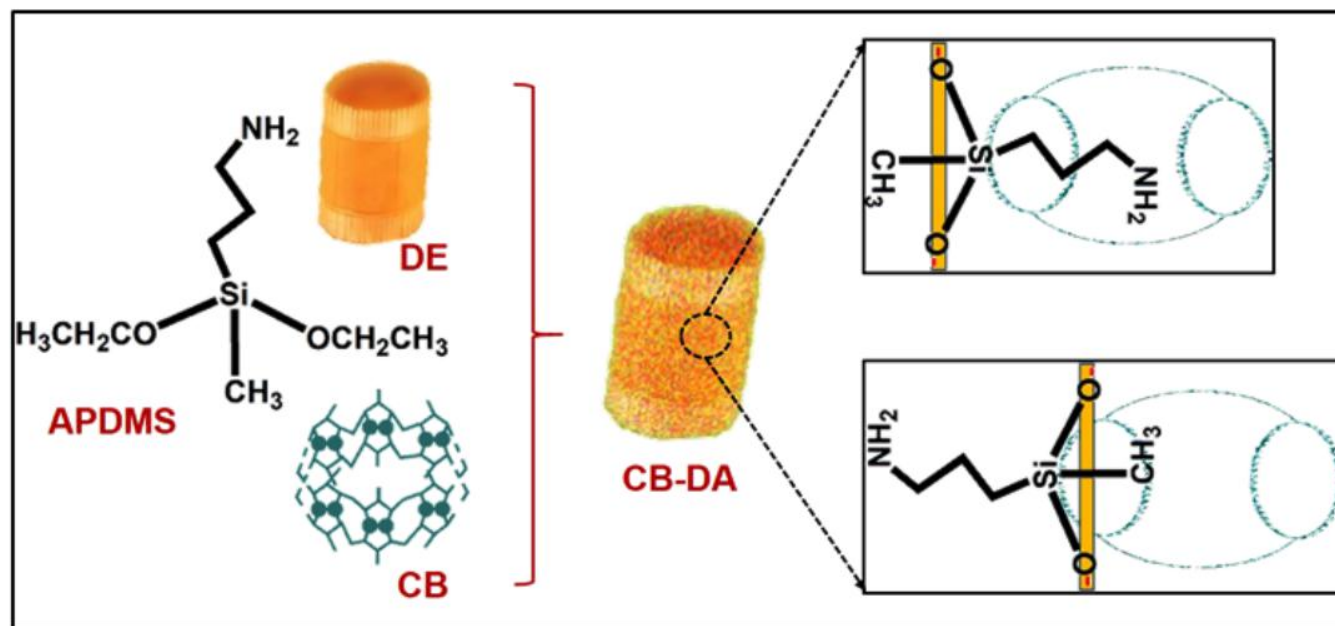


**Figure 1.3.3. (A) Schematic representation of the cucurbituril modification of the amino-functionalized diatomaceous earth (CB-DA).**

The two free chains of APDMS on the substrate are encapsulated in the cavity of the CB.

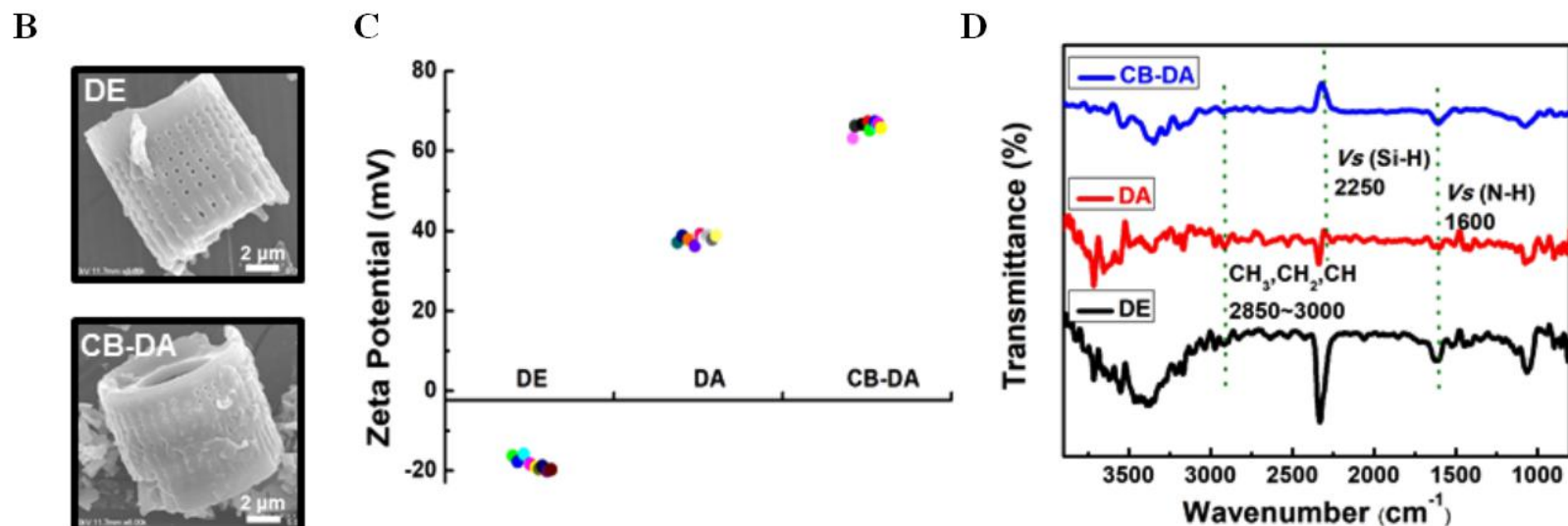


**Figure 1.3.3. Schematic representation of the cucurbituril modification of the amino-functionalized diatomaceous earth (CB-DA).** (B) Scanning electron microscopy (SEM) images of DE and CB-DA. (C) Zeta potentials of the prepared materials: pure DE, amino-functionalized diatomaceous earth (DA), and cucurbituril-modified amino-functionalized diatomaceous earth (CB-DA). (D) Fourier-transform infrared (FTIR) spectrum analysis of the materials with dye. Pure DE (DE, black line), amine-modified DE (DA, red line), cucurbituril-coated amine-modified DE (CB-DA, blue line).

#### 1.(3.3).4 Cell and pathogen enrichment using the CB-DA

A schematic of the pathogen enrichment process is shown in Figure 4. Electrostatic interactions between the positive surface of the CB-DA and the negative charge of the cell membrane form bridges that facilitate absorption (Fig. 1.3.4.A). The pathogen-composite complex precipitates easily. To assess the enrichment capacity, a UV spectrophotometer (Libra 22 UV) was used to measure the absorbances of the supernatants from the tested pathogen samples containing *E. coli* ( $10^6$  CFU, 2 mL) after treatment with DA alone or after the CB-DA enrichment process. As shown in Fig. 1.3.4.B, the lower absorbance of the supernatant following CB-DA enrichment indicates that the CB-DA composite achieved a 90% capture efficiency within 3 mins at an *E. coli* concentration of  $10^6$  CFU/ml. Furthermore, SEM images of HCT-116 cells bound to the CB-DA surface are shown in Fig. 1.3.4.C. These experiments confirm that CB-DA is useful for biocompatible enrichment of pathogens and cells.

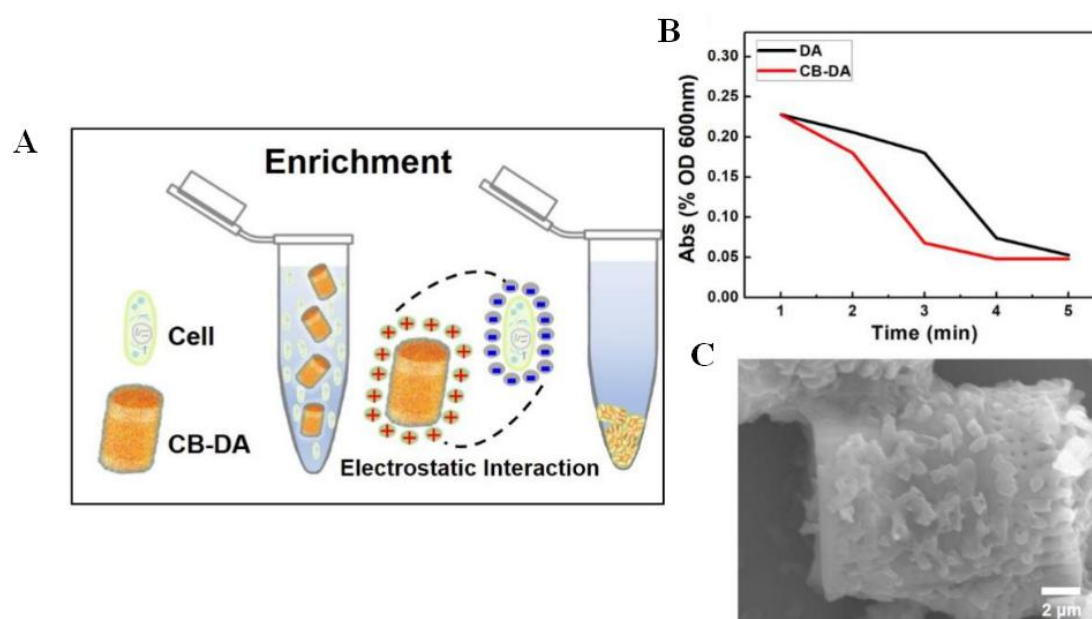


**Figure 1.3.4. Pathogen enrichment schematic and demonstration.** (A) Enrichment schematic; the electrostatic interaction between the positive surface of the CB-DA and the negative charge from the cell membrane. (B) The supernatant absorbances of the tested pathogen samples after DA and CB-DA *E. coli* enrichment (CFU  $10^6$ , 2 mL). (C) Cell enrichment demonstration. SEM images of the HCT-116 cells adhered to the surface of CB-DA.

### 1.(3.3).5 Nucleic acid isolation using the CB-DA

To further confirm that the CB-DA composite rapidly and effectively adsorbed the bacteria, the fluorescence signals from real-time PCR analyses of amplified DNA extracted from the supernatant and precipitate (Fig. 1.3.5.A) of the *E. coli* (CFU  $10^4$ , 1 mL) enrichment using a Qiagen kit (100  $\mu$ L of tested sample) are shown in Fig. 1.3.5.B. The inside figure shows the melting-curve plots, which represent the amplification products from the systems (black line:  $10^4$ , 100  $\mu$ L as a positive control; red line: supernatant from the CB-DA-treated sample, 100  $\mu$ L; blue line: enrichment with CB-DA, 100  $\mu$ L of precipitate; green line: DW as a negative control). The cycle number – fluorescence data in Fig. 1.3.5.B showing the PCR efficiency ( $= 2^{\text{cycles}}$ ) of enrichment from CB-DA system (in blue) and original pathogen (positive, in black) are  $2^{26}$  and  $2^{28}$  under 100 (fluorescence) respectively. We observed that the CB-DA enrichment system was  $(2^{(28-26)})4$ -fold more effective for pathogen enrichment, suggesting that it could be used for sample preparation in diagnostic systems. In addition, we simply measured the amount of DNA (low molecular weight from salmon sperm, 31149-10G-F) captured by DA or CB-DA in 5 mins. DNA (100  $\mu$ L; 0.1 mg/mL) was added to 1 mL of DA (50 mg/mL) or CB-DA (50 mg/mL), and the surface charges of the DA-DNA and CB-DA-DNA mixtures after washing out the free DNA are shown in Fig. 1.3.5.C. The reduction in the surface charge of the CB-DA-DNA indicates that the CB-DA composite is more effective at capturing the nucleic acid, and this effect may be due to the previously reported covalent bonding, physical adsorption, electrostatic interactions, and heterogeneous surface binding intrinsic to supermolecular family members.

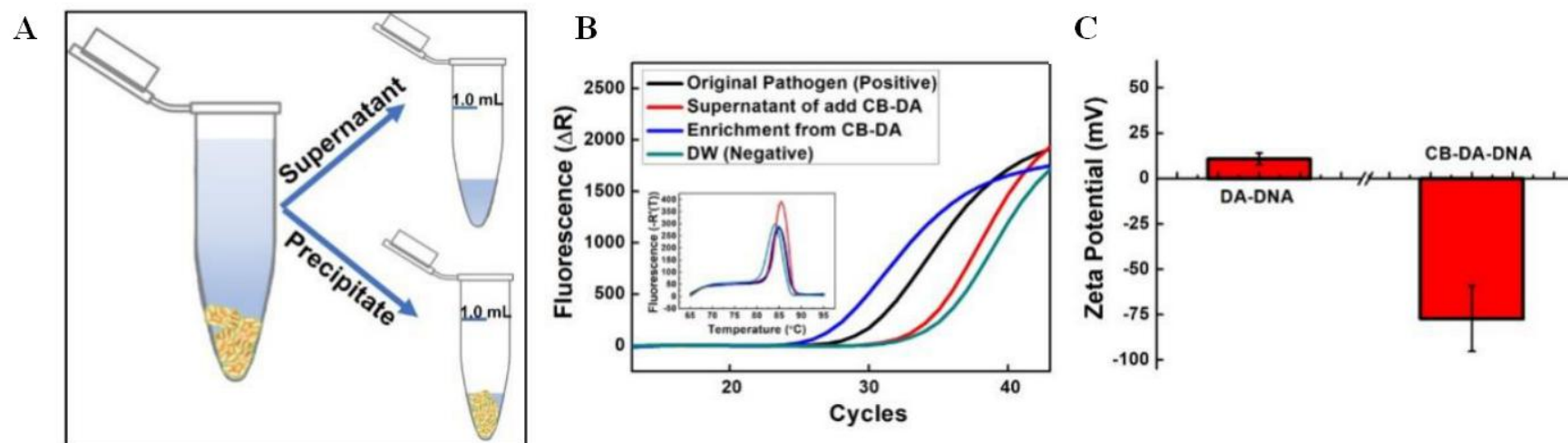


**Figure 1.3.5. NA isolation using the biocompatible composite.** (A) A diagram of the supernatant and precipitate from the enrichment system. (B) Fluorescence signals from real-time PCR analyses of amplified DNAs extracted from the supernatant and precipitate following *E. coli* enrichment (CFU  $10^4$ , 1 mL) using a Qiagen kit (100  $\mu\text{L}$  of the tested sample). The inside figure shows the melting-curve plots representing the amplification products from the systems. Black line:  $10^4$  CFU in 100  $\mu\text{L}$  as a positive control; Red line: supernatant with CB-DA addition, 100  $\mu\text{L}$ ; Blue line: enrichment from CB-DA (100  $\mu\text{L}$  of precipitate); Green line: DW as a negative control. (C) Zeta potential-based comparison of the nucleic acid capture efficiencies of the composites, i.e., DA-DNA and CB-DA-DNA.

### 1.4.3 CONCLUSION

In chapter 3, an efficient fabrication method for supermolecular modified diatom composite (CB-DA) is presented, and this CB-DA composite was then used for efficient sample enrichment and in-situ nucleic acid preparation from enriched prokaryotic and eukaryotic cells. The well-known amino functionalization technology was improved, as verified by surface charge characterization. APDMS modification, which involves diethyl groups, requires two sites for modification, while APTES modification, which involves triethyl groups, requires three sites for modification. Our results show that the latter approach leads to a higher density of amino modification. Our results also show that supermolecule formation was maximized in the CB-DA composite, and that the encapsulation performance of the composite was improved via enhanced dispersion. We also showed that the novel CB-DA composite achieved a 90% capture efficiency within 3 mins even at an *E. coli* concentration of only 10<sup>6</sup> cfu/mL. We also observed that real-time PCR analysis of amplified DNA isolated using the CB-DA enrichment system showed a 4-fold enhancement of the early signal, which might be useful for sample preparation to support early diagnosis. This study provides new insight into amino functionalization and lays a foundation for further development of sample preparation techniques for human disease diagnostics and molecular encapsulation in drug delivery systems.

## **SECTION 2 NANOMATERIALS ON TREATMENT**

## 2.1 INTRODUCTION

### 2.1.1 Challenges of the Nanotechnology (NTC) in treatment

Nanomedicine and nano delivery systems are a relatively new but rapidly developing science where materials in the nanoscale range are employed to serve as means of diagnostic tools or to deliver therapeutic agents to specific targeted sites in a controlled manner.[77-79] NTC offers multiple benefits in treating chronic human diseases by site-specific, and target-oriented delivery of precise medicines.[80-81] Nowadays, resistance to and the toxicity of antibiotics are a concern due to the rising incidence of microbial infections with serious side effects in world healthcare settings. Particularly, infections caused by multidrug-resistant bacteria (super bugs), fungi, Gram-negative bacteria, or Methicillin-resistant *S. aureus* (MRSA), remain difficult to treat due to their resistance to multiple antibiotics.[82-85] In addition to fungal infection, these conditions debilitate the human immune system, which leads to increased mortality from fungal infection among cancer patients and transplant recipient. The opportunities and challenges of nanomedicines in drug delivery from synthetic / natural sources to their clinical applications are regarding the trends and perspectives in nanomedicine area.[86-88]

Invasive Aspergillosis infection (IAI) is a more frequent direct cause of death than mortality from other diseases.[76, 89] Especially, the treatment of IAI by *Aspergillus fumigatus*, *Candida albicans*, and *C. glabrata* are constrained due to the toxicity of the agents, drug resistance, and low efficacy.[90-91] *Aspergillus* species kill up to 80% of infected patients. Therefore, the ubiquitous and harmful *Aspergillus*, which can be found in the dust in your home (moldy walls, molds on foods), can induce lesions without clear symptoms and has been set as an experimental subject. According to the statistical reports, around 75% of antibiotics were consumed not by humans, but by livestock, and many developed countries have no restrictions on this use.[92-95] Generally, drugs with antifungal activity that are used to treat patients with IAI are azoles, polyenes, and echinocandins. Among these drugs, amphotericin B



is one of polyenes, used to break the membrane of fungi by binding with ergosterol, which subsequently leads to cell death.[96-97] Itraconazole is a tolerated azole antifungal drug, affecting the cell membrane directly or after its metabolism.[98] However, the clinical use of these drugs is extremely limited since they have serious side effects, such as nausea, diarrhea, abdominal pain, rash, headache, and organ damage due to their high toxicity, insolubility, and sensitivity to pH. Hence, there is an urgent demand to find better antibiotics, which could have enhanced efficacy and persistence with relatively less toxicity.[99-100]

### **2.1.2 The introduction of studied materials**

To address these challenges, numerous nanotechnologies based on nanomaterials have emerged for effective therapy in the field of the nano-medicines. The emerging nanomaterials exhibit unique physical, chemical, and biological properties that are widely studied in various clinical applications.[27, 101-102] However, many side effects have been noted when moving these technologies from the bench to the bedside due to insufficient effective and timely infection eradication, and toxicity against the surrounding normal cells.[103-105] Therefore, the development of non-toxic composites that substitute for or assist the antibiotics, which can provide a concrete direction for further clinical use in the medical therapy market, is essential. Referred the recent study of the bio-molecular interactions on homobifunctional imidoester (HI) which is one of the most specific acylating groups available for the modification and involved in good biocompatibility.[106] And due to the minimal cross reactivity toward other nucleophilic groups in proteins and does not alter the surface charge of the protein, potentially retaining the native conformation and activity of the protein, the HI including dimethyl adipimidate (DMA), dimethyl pimelimidate (DMP), dimethyl suberimidate (DMS), and 3,3'-dithiobispropionimidate (DTBP) etc. has been exploited in biomedical applications, such as disease diagnostics and drug delivery. [107-108]

Diatomaceous earth (DE) has an extraordinary 3D porous structure with micro- to

nanoscale dimensions that has allowed it to be successfully employed in photonics, sensing, biosensing, filtration, adsorption, microfluidics, catalysis, drug delivery, and nanofabrication.[73, 109] The high biocompatibility, reproducibility, and low production cost of DE makes it attractive for many applications, and its highly modifiable surface is a significant advantage for nano-sorbents.[48, 51] However, exploration of pure DE as a commercial sorbent has been limited by the loading capacity due to its size. Furthermore, repeated usability (and preferably cyclic utilization) is essential for eco-friendly wastewater treatment systems.[50, 52] Therefore, considerable research effort has been invested in modifying the DE structure into technologically more suitable functional materials. To expand the usefulness of DE and overcome its inherent limitations, two types of materials have emerged as promising candidates: super-molecular cucurbiturils (CBs) with high molecular absorption properties, and magnetic materials with potential for treating wastewater at a large scale within a short time due to facile collection with an external magnet.[110-112] Pumpkin-shaped CBs are important in host–guest chemistry and have been employed for molecular encapsulation, water treatment, surface adhesion, biomarker-targeted theranostics, and drug delivery.[113-115] Driven by a diverse range of inter- and intramolecular interactions, CBs are ideal hosts for charged amphiphilic guests due to ion-dipole stabilization and possible hydrogen bonding inside the CB cavity.[116] Although the great potential of CBs has been highlighted in many studies, three major performance limitations remain to be addressed: (1) unexplained poor solubility in aqueous solutions, (2) unsuccessful functional group modification, and (3) unclarified ion effects in CB applications. Especially, poor solubility poses a serious obstacle for the development of CB-based applications, and much research effort has been expended to overcome these limitations by developing new water-soluble host/guest systems with a synergistic blend of supra-molecular assemblies and nanomaterials.[117-119] Additionally, magnetic nanocrystals are of importance in various applications, as they can be used for both tracing and diverse valence configurations in colloid interface science and functional materials.[120] Meanwhile, mesoporous materials have attracted much attention for years because of

their beneficial uses as catalysts, catalysis supports, drug carriers, electric materials, and adsorbents. For example, mesoporous magnetite ( $\text{Fe}_3\text{O}_4$ ) nanomaterials have been widely utilized in many fields including sensing agents, catalysis, electrical devices, energy storage devices, and biomedical drug loading and delivery.[121-123] However,  $\text{Fe}_3\text{O}_4$  nanoparticles often suffer from poor stability and dispersity, which represents a barrier to advanced applications.[124-125]

### **2.1.3 Overview of our related researches**

Here, aim at studying high efficiency drugs we explored the treatment applications of nano composites (DE, ZnO etc.) with surface modification to optimize their properties. In the present study (chapter 1), CB was coated on diatomaceous earth (DE) to maximize the efficiency of CB in the removal of polluting dyes and pathogens from aqueous solutions. DE is a promising biosilica for use in synthetic nanomaterials due to its low environmental impact, high biocompatibility, and significant advantages in terms of scalability, structural reproducibility, and low production costs. As such, it has been successfully employed in various fields, such as sensing, optoelectronics, energy conversion, and storage. We modified the surface of DE with amine groups and then coated CB onto the modified DE (DA), producing a nanocomposite referred to here as CB-DA. We investigated the possible mechanisms behind the role of CB in improving the stability of DE by preventing self-aggregation. We also applied the CB-DA composite in the treatment of both tap water and water samples from the Han River in Seoul, Korea to test its practical utility. We found that the CB-DA nanocomposite had an efficiency that was 100 times greater than that of CB alone and it exhibited high stability in the encapsulation and removal of dye molecules and pathogens. When we applied the CB-DA nanocomposite to a filtration system, water was able to be purified within 2 min. Therefore, a CB-DA platform can be employed for molecular encapsulation in water treatment and in a broad range of biological systems that require rapid results and high stability.

In chapter 2, we prepare a novel adsorbent consisting of mesoporous magnetic

nanomulberry-shaped  $\text{Fe}_3\text{O}_4$  (MNM) on the surface of DE and CB (MNM-DE-CB) via a facile two-step method. Subsequent characterization demonstrated the ability to synergize the stability and solubility of the adsorbent for pollutant removal and encapsulating molecules in aqueous solution. MNM-DE-CB can be easily collected and recycled due to its strong magnetic properties, reducing reagent costs. The structural characteristics of the MNM-DE-CB composite, adsorption capacity, and influence of metal ions and pH were evaluated. Finally, the 3D adsorbent was subjected to cytotoxicity testing using a cancer drug to demonstrate drug delivery applications.

Inspired by the character that Homobifunctional Imidoester (HI) is one of the most specific acylating groups available for biocompatible modification and has minimal cross reactivity toward other nucleophilic groups in proteins, in chapter 3 we design an efficient and advanced anti-Invasive Aspergillosis Infection (IAI) composite into intravenous administration. Shuttle shaped semiconductor nanomaterials (ZnO NSs) was synthesized readily, followed by HI modification for enhanced antifungal effect and reduced toxicity. The covalently acylating groups involved in good biocompatibility which has minimal cross reactivity toward other nucleophilic groups in proteins and does not alter the surface charge of the protein, potentially retaining the native conformation and activity of the protein. Thereby, the increased surface charge and solubility gathering with the shuttle structure of ZnO NSs-HI showing powerful anti-coagulation in blood which could solve the mainly agglomerate limitation of the efficiency of nanomaterials intravenous. The results of its antifungal efficiency, enhanced antibiotic (Itraconazole) synergistic effect and biocompatibility in vitro blood test and vivo intravenous study suggest that the ZnO NSs-HI is not only an effective anti-(IAI) composite but also an proper candidate of medical system where advocate to reduce the usage of antibiotic.

In chapter 4 we report a novel non-toxic composite with enhanced antibiotic efficacy and persistence against fungi and Gram-negative bacteria. The non-toxic composites are fabricated with in-house synthesized ZnO and biocompatible frustules DE, called DE-ZnO composites. Toxicity and persistence of antibiotics are important issues for

reducing the side effects in patients who suffer from various infectious diseases. Thus, we conducted phenotypic and genetic analysis for both in vitro and in vivo testing of DE-ZnO as an antibiotic agent with negligible toxicity, not as a carrier for drug delivery. Through specific attention to its mechanism of action, we showed that DE-ZnO breaks fungal and bacterial cellular networks by its physical and chemical properties, such as the shape of DE-ZnO and high levels of production of reactive oxygen species (ROS). In addition, we demonstrated that DE-ZnO has a long persistence of its antibiotic effect against fungal (*A. fumigatus*) and Gram-negative bacterial (*E. coli* and *S. enterica*) infections. Furthermore, we showed DE-ZnO has an antifungal synergistic effect against *A. fumigatus* when used in combination with amphotericin B and itraconazole. Therefore, we believe that the ability of DE-ZnO to enhance the efficacy and persistence with non-toxicity indicates it could be useful as a possible antibiotic agent, as well as an enabler for combination therapy with existing drugs in various antimicrobial applications.

## 2.2 EXPERIMENT SECTION

### 2.2.1 Chemicals and Reagents

All reagents were of analytical grade and used without further purification. We ordered biocompatible diatomaceous earth DE powder, suitable for most filtration applications, from Sigma-Aldrich (St. Louis, MO, USA). (3-aminopropyl) triethoxysilane (APTES, 98%), cucurbit[5]uril hydrate ( $C_{30}H_{30}N_{20}O_{10}$ , 545198-100MG), cucurbit[6]uril hydrate ( $C_{36}H_{36}N_{24}O_{12}$ , 94544-1G-F), cucurbit[7]uril hydrate ( $C_{42}H_{42}N_{28}O_{14}$ , 545201-100MG) and cucurbit[8]uril hydrate ( $C_{48}H_{48}N_{32}O_{16}$ , 545228-100MG) were also obtained from Sigma-Aldrich. Trypan blue (TB; 0.4%) was ordered from Gibco, a division of Life Technologies Corporation (Grand Island NY 14072 USA). Methylene blue ( $C_6H_{18}ClN_3S \cdot 3H_2O$ ) was obtained from Daejung Chemicals and Metal Co., Ltd (Gyeonggi-do, Korea) and rhodamine B ( $C_{28}H_{31}ClN_2O_3$ ) was purchased as R6626-25G 95% (HPLC) from Sigma-Aldrich. Magnesium chloride (M4880-100G, 97%), calcium chloride (383147-100G, 96%), and sodium chloride (S3014-500G, 98%) were supplied by Sigma-Aldrich. M111-100 mL of sodium dodecyl sulfate (SDS; 10%) manufactured by VWR International LLC, Life Science was used. 2',7'-dichlorofluorescein (Lot # BCBZ6854), zinc oxide nanoparticles (Cat. No. 721077-100G), amphotericin B from *Streptomyces* sp. (Cat. No. A2411-250MG), Itraconazole (Cat. No. I6657-100MG), and 2',7'-Dichlorofluorescein (DCF) (Cat. No. BCBZ6854) were purchased from Sigma-Aldrich (St. Louis, MO, USA). Hexadecyltrimethylammonium bromide ( $C_{19}H_{42}BrN$ , > 98%, CTAB) was purchased from Tokyo Chemical Industry Co., Ltd. (Tokyo, Japan). Dulbecco's Modified Eagle's Medium (DMEM; Life Technologies, Carlsbad, CA, USA) was used for cell culture. LB medium was used for the bacterial cultures. Sabouraud dextrose agar with chloramphenicol media (Cat. No.:C6781; Lot no: 437412) for the fungi culture was purchased from Santa Maria-USA. Milli-Q water and phosphate-buffered saline (PBS, 10 $\times$ , pH 7.4) were used in all experiments. The other two silica materials used were silica gel (pore volume 0.43 cm<sup>2</sup>/g, 28-200

mesh) produced in Germany by Sigma-Aldrich and silica sand (Cat. No. 37549-01, Tokyo Japan). Milli-Q water with a resistance greater than 18 M $\Omega$ , 99% ethyl alcohol, phosphate-buffered saline (PBS, 10 $\times$ , pH 7.4), and streptavidin-coupled magnetic beads (Thermo Fisher Scientific, Waltham, MA, USA) were used in all experiments.

### **2.2.2 Biological samples**

a) L929 (mouse C<sub>3</sub>H/An connective tissue) and eukaryotic cells (HCT-116 colorectal cancer cells) were maintained in culture dishes with high-glucose DMEM supplemented with 10% fetal bovine serum (FBS) at 37 °C in a 5% CO<sub>2</sub> atmosphere. b) The prokaryotic species *E. coli* (ATCC25922) and *Salmonella* (ATCC14028) were inoculated into either nutrient broth medium or LB medium and were incubated overnight at 37 °C with shaking. c) *Aspergillus* fungi (ATCC36607) were grown in Sabouraud dextrose agar at 25 °C for 5 d. After culturing, the *Aspergillus* fungi were resuspended in PBS and quantified by using a hemocytometer.

## **2.2.3 Functionalized materials**

### **2.2.3.1 Preparation of magnetic diatomaceous earth (MNM-DE)**

Pure DE and functionalized DE (3-aminopropyl triethoxysilane modification (DA), DA and cucurbit[X]uril modification, CB[X]-DE and CB[X]-DA) were prepared for this study. Gravity-powered washing was used to wash out any fragments in the commercial DE and the uniformity of the DE was confirmed using DLS based on particle size patterns. This included three steps. First, 3 g of DE was dissolved in 150 mL of deionized water (DW) in a 250-mL flask, followed by stirring at 500 rpm for 10 mins. After standing for 1 min, the precipitate was removed and the supernatant collected in a 50-mL tube. This was then centrifuged at 1400 rpm, after which the supernatant was removed and the precipitate collected. Secondly, 99% EtOH was used instead of DW and the above process was repeated to dissolve contaminating ions. Thirdly, following the stirring and washing of DE (500 rpm) with 100 mL DW, the supernatant was removed and the precipitate collected after 30 seconds of standing. The sizes of the particles were measured using DLS, until a relatively uniform pure DE solution was obtained. The DE was then dried in a drying oven and stored in a reagent bottle.



### **2.2.3.2 Preparation of magnetic MNM-DE**

Magnetic nanomulberry-diatomaceous earth (MNM-DE) was synthesized using a typical hydrothermal method. Firstly, DE was purified by gravity settling in deionized (DI) water, and 1.0 g  $\text{FeCl}_3 \cdot 6\text{H}_2\text{O}$  and different amounts of pure DE (0.3 g, 0.2 g, or 0.1 g) were added to 20 mL EG and stirred for 30 min to generate three brownish-yellow solutions. Following addition of 3.0 g  $\text{C}_2\text{H}_3\text{NaO}_2$  and 10 mL EDA, the mixture was stirred for 30 min with shaking at 1000 rpm, and then sealed in a 100 mL Teflon-lined stainless-steel autoclave at  $200^\circ\text{C}$  for 8 h and allowed to cool to room temperature. The resulting black products were washed several times with water, collected by a magnet, and dried at  $50^\circ\text{C}$  in a vacuum oven. Finally, 0.7 g MNM-DE was obtained from each reaction (~60–75% of coating ratio).

### 2.2.3.3 Preparation of magnetic MNM-DE-CB

Preparation of MNM-DE-CB was performed by the microwave method. Briefly, 5 mg MNM-DE was dissolved in 1 mL DI water to form a 5 mg/mL MNM-DE solution. A 25 mg sample of CB[6] was then added to 500  $\mu$ L DI water and sonicated for 1 min using an ultrasonic instrument. Subsequently, 25  $\mu$ L of the 50 mg/mL CB solution was added dropwise to 2 mL MNM-DE solution and heated in a microwave oven for 1 min. APTES-functionalized diatomaceous earth (DA) was prepared following the process described in our previous study<sup>26</sup>. In short, 2 mL of APTES was added drop-wise into 100 mL of 95% ethanol solution while stirring at 400 rpm for 3 min at room temperature (RT). After this, 500 mg of DE was dispersed into this solution under stirring (600 rpm) for 4 h. The precipitate was washed twice with ethanol to remove any free silanol. The DA was collected via centrifugation and subsequently dried in a vacuum overnight at RT and stored in a reagent bottle. Finally, cucurbit[X]uril modified DE and DA were prepared. Due to the different solubilities of the four members of the CB family (CB[X]; X = 5, 6, 7, or 8), we used the same molar concentration for CB[X]. The DE or DA precipitate was dissolved in DW (100 mL), then a certain amount of CB[X] was added under stirring at 500 rpm for 40 mins. After several cycles of washing with DW, the precipitate was collected, dried in a drying oven, and stored in a reagent bottle.

#### **2.2.3.4 Preparation of the ZnO NMS and DE-ZnO composites**

a) A modified hydrothermal method has been used to synthesize ZnO NMS crystals in alkaline medium. Briefly, 1 mL of 1 M CTAB was added to 98 mL of Milli-Q water in a 250 mL flask, and magnetically stirred at 500 rpm at 90 °C. Then 1 mL of 1 M Zn NO<sub>3</sub>6H<sub>2</sub>O was added and it was stirred for 50 mins. Under steady stirring and incubation conditions, 2 mL of ammonium hydroxide solution was added into the reaction mixture drop-wise. As the white precipitates were produced, we transferred the flask into an ice box to stop the reaction. The white precipitates were collected by centrifugation and washed with Milli-Q water three times to wash away the residual ions. Then, the white precipitates were dried in a 56 °C oven overnight. b) The bio-semi-composites (DE-ZnO) were synthesized by a typical nanoengineering particle surface method. The porous DE acted as a well matrix that supplied a sufficient surface area for the ZnO. Briefly, DE was purified by gravity settling in deionized (DI) water, the uniform DE (0.5 g) was then dissolved in 98 mL of Milli-Q water in a 250 mL flask. Then, 1 M Zn NO<sub>3</sub>6H<sub>2</sub>O and 1 mL of 1 M CTAB were added to the DE solution. Under magnetic stirring at 500 rpm at 90 °C for 50 mins, the activated Zn<sup>2+</sup> diffused and anchored on the surface of the DE by van der Waals forces. Our modified hydrothermal method for synthesis of ZnO NMS has been carried out here, with the ZnO NMS growing in a crystal direction. As we can see, the color of reaction solution changed from brick-red (DE) to pink-white, then we transferred the flask into an ice box to stop the reaction. The produced precipitates were collected by centrifugation and washed with Milli-Q water three times to wash away the residual ions. Furthermore, a gravity settling method was used to wash out the unbonded ZnO NMS. Finally, the precipitates were dried in a 56 °C oven overnight.

### 2.2.3.5 Preparation of the ZnO NSs and ZnO NSs-HI

a) The ZnO NSs crystals were synthesized by the hydrothermal method in alkaline medium. Briefly, 1 mL of 1 M  $\text{Zn}(\text{NO}_3)_2 \cdot 6\text{H}_2\text{O}$  (Sigma, 228737-100G) and 1 mL of 1 M cetyltrimethylammonium bromide (CTAB, DaeJung Chemicals, 2544-4105) was added to 98 mL Milli-Q water in a 250 mL flask. The system was magnetically stirred (500 rpm) along with heating at 95 °C for 50 min. Subsequently, under steady stirring conditions, 2 mL ammonium hydroxide solution (DaeJung Chemicals, 1065-3300) was added drop-wise to the reaction mixture. With stirring, the milky colloidal solution appeared. To stop the growth of ZnO NSs, the reaction flask was placed in a 0 °C freezer immediately. After about 10 min, we transferred the product into 50 mL tube and centrifuged. Then removed the supernatant and re-suspended the precipitation with Milli-Q water to wash out the residual ions (3 times repetition). Finally dried the precipitation by Drying Oven (Yamato, DX312C) at 56 °C overnight.

b) In order to enhance the stability of ZnO NSs and conjugate associates the characteristics with biological activities, a homobifunctional Imidoester (HI) modification has been executed. Here, two kinds of HI (DMP or DMS) have been used in tests. Briefly, 4mg ZnO NSs (40mg/ mL, 100  $\mu\text{L}$ ) and 4mg HI (DMP or DMS, 10mg/mL, 400 $\mu\text{L}$ ) have dissolved in a 1.5mL EP tube within a total 500  $\mu\text{L}$  solution. The mixture has been oscillated by the Oscillating machine (Magic-mixer TMM-5). After 12 hours, the mixture was centrifuged at 12000rpm for 5min (Mini-Centrifuge, Labogene). Removed the supernatant and the precipitation was washed by Milli-Q water (2 times washing). Finally, 400 $\mu\text{L}$  Milli-Q water was used to re-suspension the precipitation to obtain 10mg/ mL ZnO NSs-HI solution. Otherwise, we dried the precipitation by drying Oven (Yamato, DX312C) at 56 °C overnight.

#### **2.2.4 Characterization**

The morphology of the ZnO nanomaterials (commercial or synthesized), DE-ZnO, and related biological samples were characterized using Field Emission Scanning Electron Microscopy (FE-SEM) on a JSM-7500F instrument (JEOL) to confirm the reaction and surface materials. Zeta potentials of the materials were measured using dynamic light scattering (DLS) on a DynaPro NanoStar instrument (Wyatt). Fourier-transform infrared spectroscopy (FTIR) analysis was performed using a JASCO 6300 instrument (JASCO) on bare ZnO-C (100 ~5000 nm), (ZnO-S (~300 nm), and DE-ZnO to obtain information on the chemical modifications. In addition, the elements present in the composite materials were analyzed using EDX, while UV/visible spectrophotometer measurements were used to determine the composite materials.

### 2.2.5 Dye removal (adsorption)

A standard stock solution of TB dye was prepared via dilution with deionized water to a final concentration of 40 mg/L. The dye solution exhibited maximum absorbance at a wavelength of 598 nm. The concentrations were calculated using the Beer-Lambert equation:

$$\text{Absorbance} = \epsilon * C_s * l,$$

where  $\epsilon$  is the molar absorptivity,  $C_s$  is the concentration of the sample, and  $l$  is the thickness of the absorbing medium (1 cm). The amount of absorbed dye was calculated from the difference between the initial and final concentrations at 20 min intervals. Adsorption levels were assessed using duplicated mini-quantity experiments: 40-100  $\mu\text{L}$  (50 mg/mL) of DE materials (D, DA, CB[X]-DE, CB[X]-DA) were tested with 1 mL (40 mg/L) of TB. After the batch adsorption process, the absorbance of TB in the residual solution was estimated using a UV/visible spectrophotometer. Adsorption of the dye onto the materials was determined in terms of distribution coefficients ( $K_d$ ) and percentage adsorption (%). The percentage adsorption and  $K_d$  were estimated using the equations

$$\text{Dye removal (\%)} = (C_i - C_r) / C_i * 100,$$

where  $C_i$  and  $C_r$  are the concentrations of the dye in the initial and real-time solutions, respectively, and

$$K_d = (\text{Adsorbent dye} / \text{residual dye}) * (V / m) [\text{mL/g}],$$

where  $V$  is the volume of the dye solution (mL), and  $m$  is the weight of the adsorbent. The efficiency of CB is limited by its poor solubility. In particular, the poor solubility results in the coagulation shown in Fig. S4A. Solubility was estimated using the homogenous surface contact in SEM ( $a_1$ : CB[6],  $10^{-5}$  mol and  $a_2$ : CB[6],  $10^{-5}$  mol with TB dye). Therefore, a dose concentration of  $2 \times 10^{-4}$  mmol/L for CB[6] was selected for further testing. The fit of the results of the experimental data to the pseudo-first order, pseudo-second order, and intraparticle diffusion models for natural and modified DE was investigated. The  $q_m$  and  $K_x$  rate constants from the slope and intercept were calculated. The Langmuir equation in linear form is expressed as

$$C_{\infty} / q_{\infty} = C_{\infty} / q_m + 1 / (q_m K_x),$$

where  $q_m$  represents the maximum adsorption capacity of the nanocomposite in mg/g,

and  $K_x$  is the Langmuir constant related to the affinity of the binding sites in L/mg.

The plot of  $C_{\infty}$  vs  $q_{\infty}$  and the linear plot of  $C_{\infty} / q_{\infty}$  vs  $C_{\infty}$  provide the values of  $q_m$  and  $K_x$  from the slope and the intercept of the curve, respectively.

### 2.2.6 Adsorption equilibrium experiment

For dye adsorption, Methyl Blue (MB) and Trypan Blue (TB) were tested. Different amounts of MNM-DE-CB were added to 1 mL dye solution at a defined concentration in a 1.5 mL tube. The mixture was shaken continuously for 1 h at room temperature, and adsorbents were collected with a magnet. The concentration of residual dye remaining in solution was analyzed by UV-Vis spectroscopy on a UV-2550 instrument (Shimadzu) by measuring the absorbance at the wavelength of maximum absorption. The % removed ( $R$ ) and adsorption capacity ( $q_e$ ) were calculated using the following equations:

$$R = \frac{(C_o - C_e)}{C_o} \times 100\%$$
$$q_e = \frac{(C_o - C_e) V}{m}$$

where  $C_o$  and  $C_e$  are the initial and equilibrium concentrations of dyes (mg/L),  $q_e$  is the equilibrium adsorption capacity (mg/g),  $m$  is the mass of MNM-DE or MNM-DE-CB (g), and  $V$  is the volume of solution (L). For regeneration measurements, recycled adsorbents were washed with 10% SDS, collected using a magnet, and used for subsequent adsorption experiments.

For drug testing, MNM-DE-CB (40 mg) was added to 5 mL ZnPC/EtOH solution (2 mM) at room temperature. The mixture was shaken for 24 h, and drug-loaded composites were separated and tested by MTT assay.



### 2.2.7 In vitro cytotoxicity assay

i) A colorimetric assay kit (Cell Counting Kit-8) was used to measure the cytotoxicity of our materials. Firstly, L929 and HCT-116 cells were cultured in DMEM medium supplemented with 10% FBS at 37 °C in an atmosphere with 5% CO<sub>2</sub> and 95% relative humidity. Cells were seeded on 96-well plates at a density of  $5 \times 10^4$  cells/well for 24 h to allow cell attachment. The medium was removed and the cells were washed once with PBS. The test materials (optimized ZnO modification ratio test) at certain concentrations in DMEM were added to separate wells in quadruplicate and incubated with the cells for another 24 h. Corresponding samples of DE-ZnO at concentrations of 0.5, 1.0, 1.5, 2.0, 2.5 and 3.0 mg in DMEM were subjected to the same process. After 24 h incubation, the suspensions were removed and the wells were washed once with PBS. A 100 µL sample of WST-8 (0.5 mg/mL in culture medium) was then added, being careful to not introduce bubbles into the wells, since they interfere with the O.D. reading. Then, the plates were incubated for 4 h at 37 °C in 5% CO<sub>2</sub> prior to analysis. We measured the absorbance at 450 nm using a micro-plate reader (BioTek, US). Absorbance values for the untreated cells were taken as controls (100% survival).

Cell viability was then calculated according to the following equation:

$$\text{Cell Viability (\%)} = \frac{\text{OD}_{\text{Treatment}}}{\text{OD}_{\text{No Treatment}}} \times 100\%$$

The biocompatibility of the ZnO nanomaterials and DE were confirmed through cell viability using an MTT assay.

### 2.2.8 ROS detection

A DCFDA Cellular ROS detection assay kit and a modified DCFH-DA (2',7'-Dichlorofluorescein diacetate) method were used for measurement of reactive oxygen species in cellular and non-cellular settings, respectively. i) Cellular study: following the DCFDA kit's manufacturer's instructions, L929 cells (10,000 cells per well) were cultured in 96-well micro-plates and incubated at 37 °C in a 5% CO<sub>2</sub> atmosphere for 24 h to allow adherence. Cells were washed with 1× buffer and then we added the tested materials (DE-ZnO). Meanwhile, we stained the cells with 100 µL DCFDA (25 µM, in 1× kit dilution buffer) for 45 min at 37 °C in a humidified 5% CO<sub>2</sub> incubator. Then, the DCFDA solution in the well was replaced with 1× buffer. The basal ROS production was detected by recording the fluorescence (Ex/Em: 485/535 nm) with a micro-plate reader. ii) Non-cellular study: 4 mg dichlorofluorescein (DCF) was added to 1 mL of phenol at 1/1000 DW dilution to obtain a concentration of 10 µM DCF. Then, 100 µL of DCF was added to the wells in dark, clear bottom 96-well microplates. Fluorescence readings were taken after 1 h incubation at 37 °C in a humidified 5% CO<sub>2</sub>. Then, we added the test materials (DE-ZnO) and fluorescence readings were taken every 30 mins during incubation at 37 °C in a humidified 5% CO<sub>2</sub> atmosphere. Relative fluorescence units (RFU) were calculated from all measurements. The plates were kept at 37 °C in a humidified 5% CO<sub>2</sub> incubator in the dark between readings. Fluorescence was measured using the following settings: excitation (Ex) at 495 nm, emission (Em) at 530 nm; temperature 37 °C; reading mode: bottom) including the background as negative controls. Each experiment was repeated on three separate occasions (n = 3). Relative fluorescence units (RFU) were calculated from all measurements. The plates were kept at 37 °C in a humidified 5% CO<sub>2</sub> incubator in the dark between readings.

### 2.2.9 Antibacterials

A suspension of bacteria (*E. coli*, *S. enterica*) was used to evaluate the antibacterial activity of different types of zinc oxides and composites. Before the assay, the bacteria were grown aerobically in LB medium for 16 h at 37 °C in 210 rpm shaking incubator. Then, the bacterial cells were harvested by centrifugation at 2000 rpm for 5 min and the bacterial cells were resuspended in LB. The bacterial suspension was appropriately diluted (up to 10<sup>6</sup>) and a 100 µL aliquot was transferred to the agar plate. The bacteria were then evenly distributed on the agar plate surface using a plastic rod. After 16 h of incubation, colonies were counted. The counting colony forming units (CFU/mL) were calculated for the original bacteria sample. The bacterial suspension was then adjusted to a fixed concentration of 1×10<sup>7</sup> CFU/mL. Thereafter, different amount of the test nanomaterials were placed into a tube containing 0.1 mL of 1×10<sup>7</sup> CFU/mL bacterial suspension and 2mL LB medium. After incubating for 16 h at 37 °C shaking at 210 rpm, we measured the absorbance of each sample at OD 600 nm. The bacteria survival rate of each sample was calculated by the equation:

$$\text{Bacteria Survival Rate(\%)} = \frac{(\text{OD}_{\text{ZnO}} - \text{OD}_{\text{Negative}})}{(\text{OD}_{\text{Positive}} - \text{OD}_{\text{Negative}})} \times 100\%$$

### 2.2.10 Antifungal Assay via Radial Growth

To determine the effect of the tested nanomaterials on fungi, *Aspergillus* was used. Dextrose agar culture media for fungi were prepared to perform the antifungal assay. Specific solid medium containing different amounts of the tested nanomaterials were established. Before being used in Petri dishes, the different treatments were mixed to ensure a good dispersion of the tested nanomaterials in the culture medium. We punched a 1 cm diameter hole in the middle of every solidified culture medium. In order to gain homogeneity and reproducibility in the experiment, the fungal spores were collected from the same 15 Day old *Aspergillus* fungi parent. Subsequently, 1000 conidia in 50  $\mu$ L PSB were added to the center hole of each Petri dish containing the culture medium for each of the described treatments. The dishes were moved to the culture oven, which was held constant at 25 °C. From the fifth Day, a photographic record was taken for each fungi sample. These records were analyzed with Image-J to measure the growth area, and we analyzed the growth rate of each treatment in comparison to the control sample. In addition, the synergy of the nanomaterials with the commercial antibiotics (amphotericin B and itraconazole) were studied. First of all, we tested the optimized concentration of pure antibiotics, and then 0.5 mg/L amphotericin B and 6.0  $\mu$ g/mL itraconazole were used as the basis for the enhancement study.

$$\text{Growth Rate of ZnO Treatment(\%)} = \frac{\text{Growth of ZnO Treatment}}{\text{Growth of Control}} \times 100\%$$

### **2.2.11 In vitro blood test**

Our designed fluid chip (Length~45 cm, volume~350 ) supplied with automatic pump were using for blood simulation test. As the ZnO nanomaterials added into 1 mL fresh sheep blood, the parallel contrast tests carried in both tube (blood R1) and the fluid chip (blood R2). In the tube test, we checked the precipitation and superstratum after keeping in standing for 30 mins. Meanwhile, we flowed the materials-blood mixture into the fluid chip under the speed control by automatic pump. And we collected the output and detected the absorbance of ZnO nanomaterials by Uv-is spectroscopy (Libra S22). The upright microscope (SAM-KYUNG ) was using for observing the blood cells' condition.

### 2.2.12 In vivo toxicity assay

ICR mice (6 weeks old, 15 males and 15 females) were purchased from Koatech (Gyeonggi-do, Korea). The mice were maintained at room temperature ( $22 \pm 2$  °C) with a 12/12 h light/dark cycle and were fed ad libitum. Thirty mice were randomly divided into three groups as follows: group I (control group); group II (LD-DE-ZnO), which received the LD-DE-ZnO; and group III (HD-DE-ZnO), which received the HD-DE-ZnO. Each group ( $n = 10$ ) contained an equal number of male and females. Mice of each sex were administered 300  $\mu$ L of DE-ZnO solution at dosages of 2 mg/mL (low dosage), 20 mg/mL (high dosage), or Milli-Q water (control group) by oral gavage. After administration, the animals were weighed and observed daily to detect any signs of toxicity over 14 d. After 14 d, the animals were euthanized using Zoletil (Virbac Korea, South Korea) and blood samples were collected from the aorta ventralis. The biochemical measurements consisted of analyses of the following: alanine aminotransferase (ALT), aspartate aminotransferase (AST), total bilirubin (T-Bil), blood urea nitrogen (BUN), creatinine, total protein (TP), albumin, albumin/globulin (A/G) ratio, total cholesterol (TC), triglyceride (TG), glucose, and phosphorous. Biochemical analysis of plasma samples was carried out by using commercially available kits according to the manufacturer's instructions. After collection of the blood samples, the body surface, all orifices, the head, all internal organs of the abdominal and thoracic cavities, and their contents were visually observed for any signs of gross abnormalities. Body and organ weights were measured for each mouse. For grouped organs, the sum of those organs was used. After collection of the organs, including the brain, heart, lung, liver, kidney, spleen, testicle, or ovary, they were preserved in 10% phosphate-buffered formalin solution for histopathologic examination. Liver sections of 3  $\mu$ m thickness were stained with hematoxylin and eosin (H&E). The slides were *observed* under an optical *microscope* (BX51, Olympus, Tokyo, Japan). The experimental protocol and this study were approved by the Institutional Animal Care and Use Committee of the Laboratory Animal Center, Osong Medical Innovation Foundation (KBIO-IACUC-2020-011).

## **2.3 RESULTS AND DISCUSSION**

### **CHAPTER 1 Cucurbituril-based Reusable Nanocomposites for Efficient Molecular Encapsulation**

#### **2.(3-1).1 CB-coated amine-modified DE for pathogen removal.**

Fig. 2.1.1 presents an illustrative diagram of the cucurbituril-coated diatomaceous earth (CB-DA) nanocomposite for use in dye and pathogen removal that improves the solubility of CB in water. CB-DA was produced by coating CB onto DE which had undergone amine group modification of its surface. Amine groups surround the inner and outer surfaces of the DE skeleton after APTES treatment, enhancing its chemical stability, allowing it to be used for extended periods, and leading to a robust coating of saline due to covalent bond formation. In addition, the C=O bonds on the edge of the CB molecule possibly react with the  $\text{NH}_2$ , suggesting that the amine group of the APTES-modified diatom (DA) might be an anchoring site for CB. In addition, the C-N bond ( $1089.9\text{ cm}^{-1}$ ) indicates that the oxygen atoms, which are located along the edges of the CB molecule, also bond with the amine group from the DA (Fig. 2.1.1). The ion-dipole interaction between the hydrogen bonds and the alkyl chain might also influence the anchoring of CB to the DA. Due to the increased surface area of DE after amine-group modification and the well-dispersed CB on the DA, the absorbency efficiency of the CB-DA conjugate in its interaction with other molecules is enhanced by covalent bonding, physical adsorption, electrostatic interaction and surface binding.

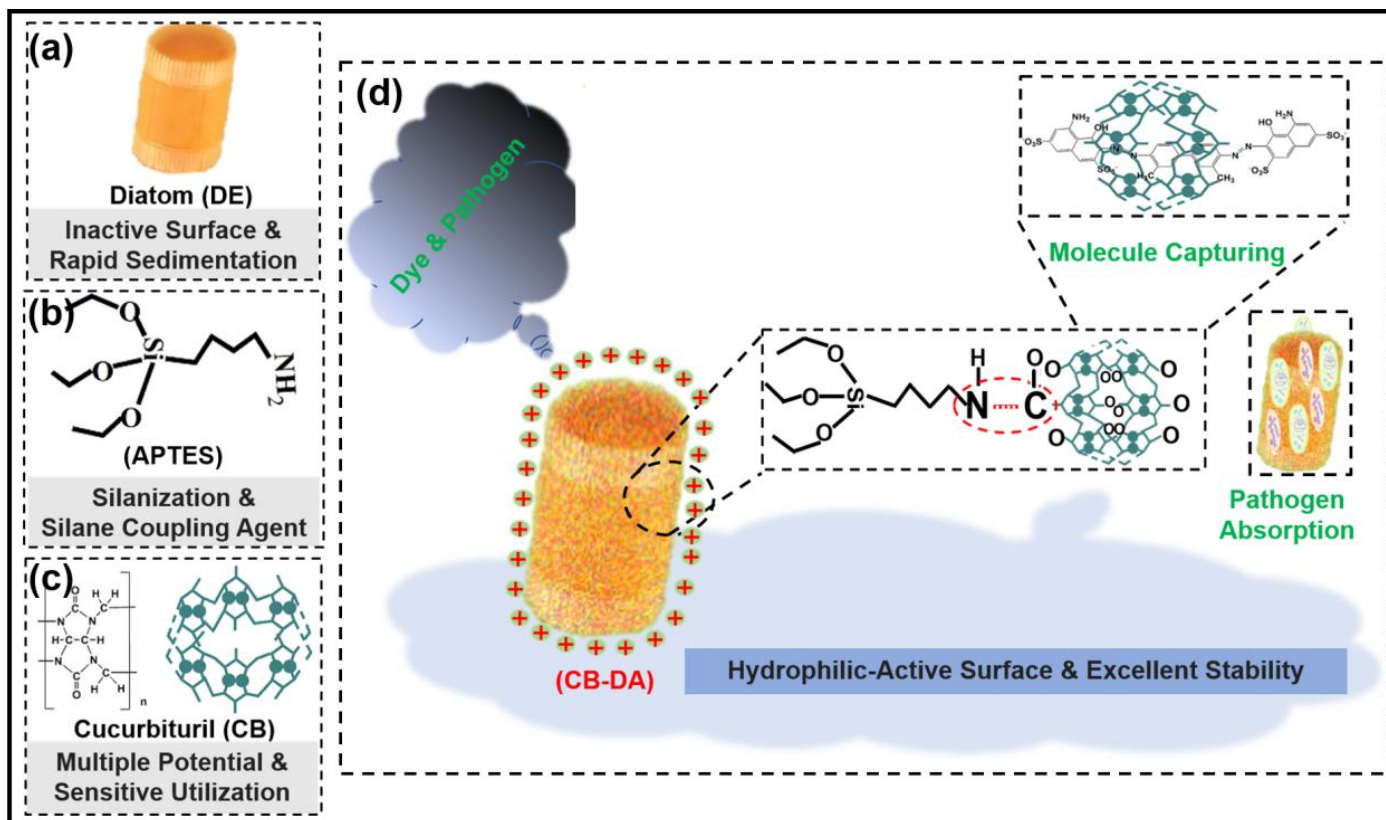


**Figure 2.1.1. Illustrative diagram of CB-coated amine-modified DE (CB-DA) for dye and pathogen removal**

CB-DA can capture dyes and pathogens via physical adsorption, electrostatic interaction, and heterogeneous surface binding



## **2.(3-1).2 The morphology of the materials**

To synthesize hydrophilic CB-DA with high absorbance, DE was first fragmented using gravity-powered washing<sup>32</sup>. The size distribution profile of the DE was then determined to be about 5 to 25  $\mu\text{m}$  using SEM and DLS. The specific surface area ( $1.4901 \text{ m}^2/\text{g}$ ) of the DE was estimated using the simple and rapid Brunauer-Emmett-Teller (BET) method. Subsequent calculations of the pore volume of the DE were conducted using Barret-Joyner-Harret (BJH adsorption/desorption) analysis (Fig. 2.1.2). The absorption/desorption curves reveal a slender hysteresis loop, which is characteristic of the high specific surface area of DE (Fig. 2.1.2.A-B). We confirmed that the thickness of the DE was around 20 nm (Fig. 2.1.2.C), and the diameter of its pores was less than 100 nm (Fig. 2.1.2.D).

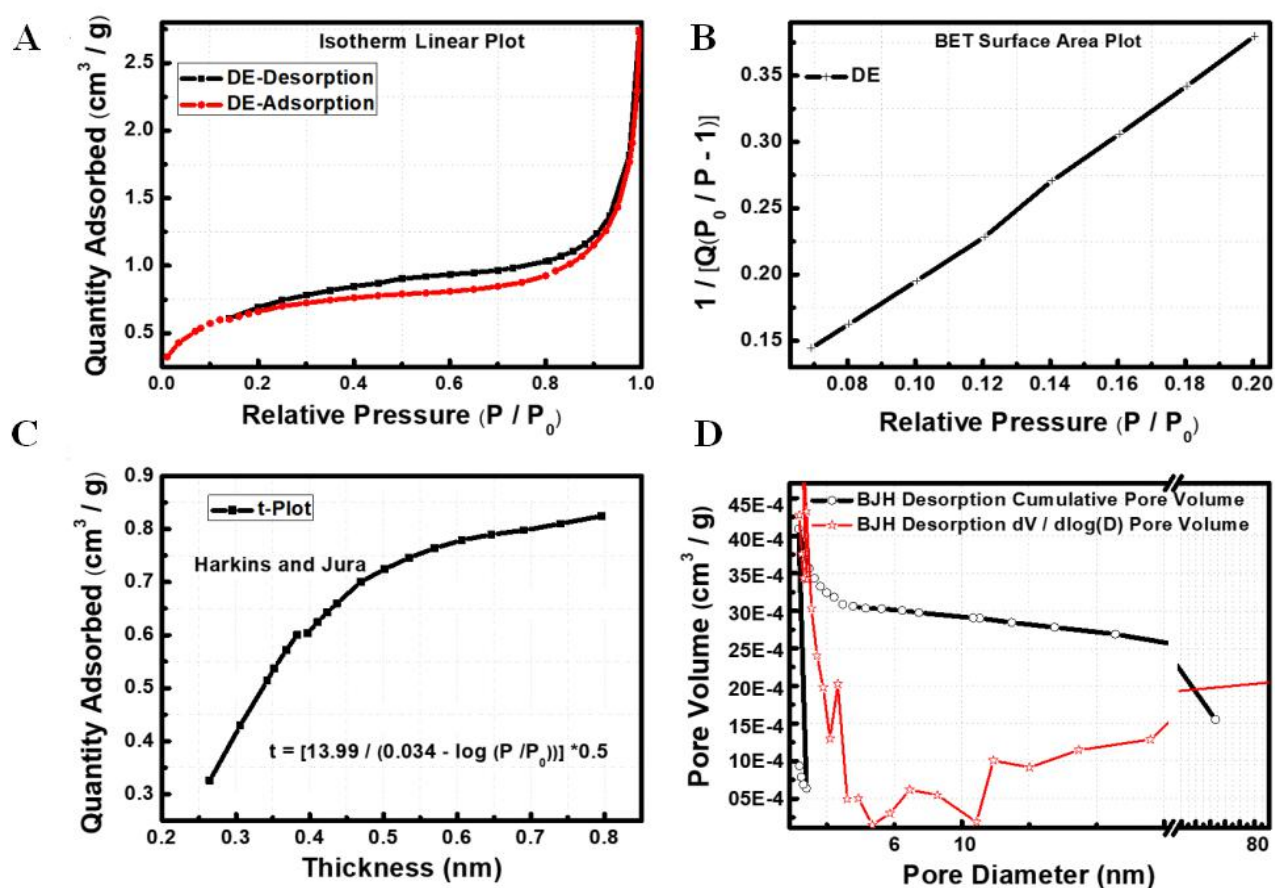


**Figure 2.1.2. Characterization of the surface of DE**

Brunauer-Emmett-Teller (BET) analysis of the specific surface area ( $1.4901 \text{ m}^2/\text{g}$ ) of DE. (A) Obtained absorption/desorption curves. (B) BET surface area plot. (C) t-plot of the quantity adsorbed (Harkins and Jura method). (D) Pore volume as a result of BJH desorption.

### **2.(3-1).3 The zeta potential of the materials**

After the fragmentation of the DE, CB was then coated on the DA using simple stirring for 20 min. To assess the electrostatic properties of CB-DA in solution, the zeta potentials of the test materials were measured (Fig. 2.1.3.A). DE alone, CB alone, and a CB-DE conjugation were confirmed to be poorly soluble with weak zeta potentials. On the other hand, DA exhibited good solubility due to the amine groups on its surface<sup>34</sup>. Notably, the CB-DA conjugation exhibited a higher zeta potential than did the DA (Fig. 2.1.3.A). These results indicate that the CB coated the surface of the DA well, with a subsequent increase in potential charge. Previous research has reported that materials with a weak zeta potential in solution tend to easily coagulate, while those with a high zeta potential are electrically stable. Hence, CB-DA is easily dispersed in solution due to its high zeta potential, and it can be distinguished from DA only by human eyes. Although we could not investigate why the zeta potential of CB-DA composites was increased, we confirmed that the CB-DA composites were stable and well dispersed in solution compared to other materials.

## 2.(3-1).4 Dye removal testing

To test the absorbance of CB-DA in the removal of TB dye from solution, the adsorption capability of the test materials was compared. The dye removal efficiency of CB-DA was 100 times higher than those of the other materials (Fig. 2.1.3.B) at 0.115 Abs/mg. In Fig. S2, the absorbance curves indicate that CB-DA exhibited good aggregation with the dye within 4 h, but CB on its own in the dye solution produced a different characteristic peak due to self-aggregation or aggregation with the dye. Amplified SEM images of the testing materials before and after the dye removal test are presented in Fig. S3; a clear change in the surface can be observed.

To optimize the synthesis of CB-DA, the optimal concentrations of CB and DA were determined. The curve in Fig. 2.1.3.C indicates that the efficiency of CB on its own was limited due to its poor solubility. This low efficiency was confirmed by homogenous surface contact analysis using SEM (a<sub>1</sub>: CB, 10<sup>-5</sup> mol and a<sub>2</sub>: CB, 10<sup>-5</sup> mol with TB dye). Therefore, a CB dose concentration of 2 x 10<sup>-4</sup> mmol/L was selected for further testing. Because solubility varies considerably between the members of the CB family, we examined CB[5-8] with DA using the optimized synthesis protocol. CB[8]-DA demonstrated the highest dye removal rate compared to the other CBs, with approximately 92% within 4 hours (Fig. 2.1.3.D).

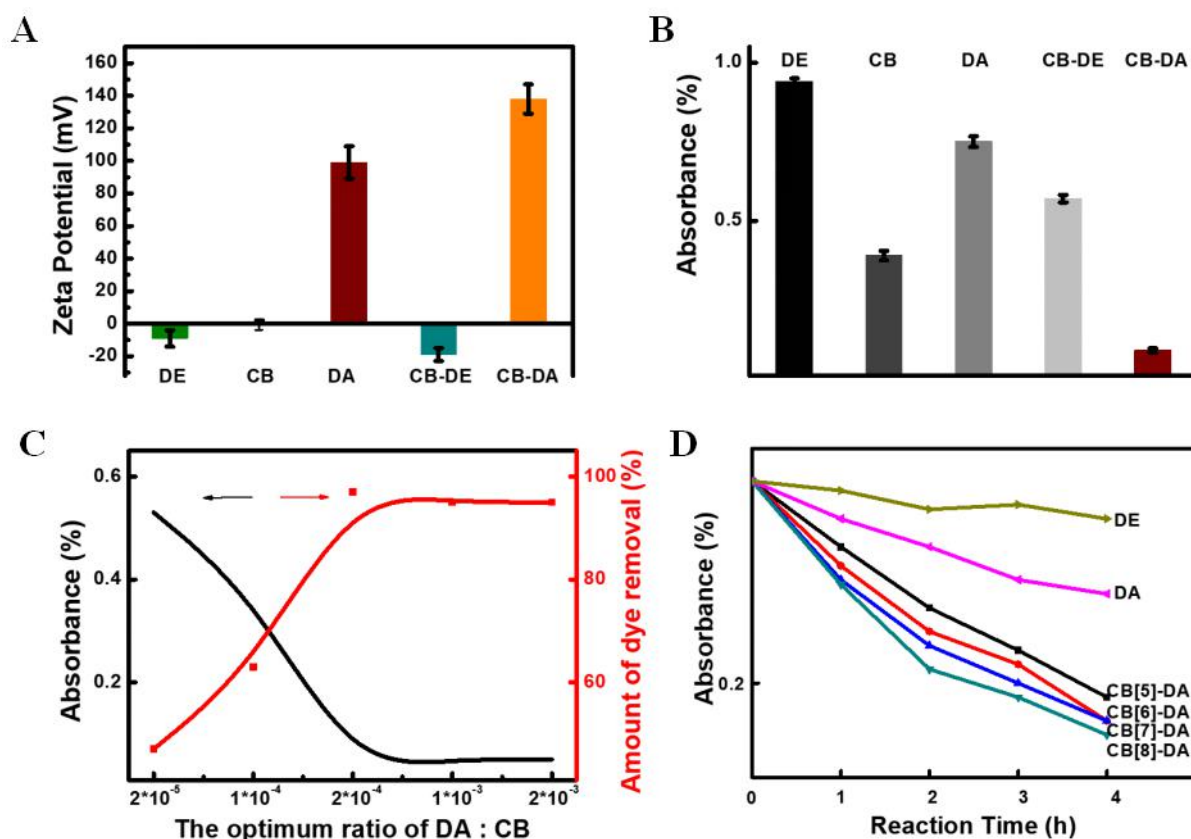


**Figure 2.1.3. Cucurbituril (CB) coating of amine-modified diatomaceous earth (DE) in an aqueous medium.**

(A) Zeta potential of the prepared materials: pure DE (DE), pure cucurbituril (CB), amine-modified DE (DA), the complex of pure DE with CB (CB-DE), and CB coated on amine-modified DE (CB-DA). The error bars indicate the standard deviation from the mean based on at least three independent replications. (B) The adsorption capacity of the materials for dye removal. The error bars indicate the standard deviation from the mean based on at least three independent replications. (C) The optimum concentration ratio of DA to CB. (D) The absorbance of supernatant after treatment with different CBs (CB[5], CB[6], CB[7] and CB[8]) with DA for dye removal.

## 2.(3-1).5 Dye removal mechanisms

Heterogeneous surface binding analysis: The chemical mechanisms and complex stability of host-guest CB-based materials are still under investigation. Chemical-optical spectrum analysis was performed to determine why CB-DA improved TB dye removal in solution. Following Fourier transform infrared (FTIR) spectrum analysis of pure DE (Fig. 2.1.4.A, black curve), the absorption peak at  $1450\text{ cm}^{-1}$  can be ascribed to the asymmetric stretching vibrations of Si-O-Si, and the peak at  $1410\text{ cm}^{-1}$  is a result of the Si-CH<sub>2</sub> bond. In addition, the absorption peaks at  $3295$  and  $1180\text{ cm}^{-1}$  can be attributed to Si-OH and C-N, respectively, on the surface of the pure DE. On the other hand, FTIR analysis of the pure CB found peaks at  $1705\text{ cm}^{-1}$ , which can be ascribed to C-H stretching vibrations and those at  $1152$  and  $1680\text{ cm}^{-1}$  to C-N stretching vibrations due to the amine groups directly bonded to the DE. After the surface modification of DA and CB, the well-defined absorption bands at  $1100\text{ cm}^{-1}$ ,  $2250\text{ cm}^{-1}$ , and  $2720\text{ cm}^{-1}$  represent C-C-C bonding, C-H bonding, and O-H bonding, respectively. The stretching vibrations at  $2850\text{--}3000\text{ cm}^{-1}$  (CH, CH<sub>2</sub>, and CH<sub>3</sub>) and aldehyde (C-H) at  $2720\text{ cm}^{-1}$  in the CB-DA group (blue curve) verified the presence of a super-molecule, and the bending vibrations at  $1680\text{ cm}^{-1}$  (C-N),  $1450\text{ cm}^{-1}$  (S=O), and  $1180\text{ cm}^{-1}$  (S=O) in CB-DA with the TB dye group (green curve) indicate bonding with the TB dye (Fig. 2.1.4.A). Furthermore, the comparison of the optical spectra for pure DE, pure CB, DA, and CB-DA presented in Fig. 2.1.4. Through using surface-enhanced Raman scattering (SERS) found that the SERS intensity for all molecular vibration frequencies decreased when the coverage of silica increased. In the CB-DA group, the intensity decreased due to the covered super-molecule (CB) with vibrational mode assignments. The silanol group of the DE is very active and can react with many polar organic compounds and various functional groups. Hence, after the TB dye is used as a hosting molecule in the CB-DA group, the TB dye reacts with the silanol groups spread over the surface of the DE. The missed silica vibration shift indicates that the molecule was subject to intense field enhancement on the dye due to the CB junctions.

Electrostatic interaction analysis: It was confirmed that electrostatic interaction was the mechanism behind the removal of the TB dye by CB-DA. Dissociation assays were employed using DW, ethyl alcohol (EtOH), and sodium dodecyl sulfonate (SDS). The amphiphilic SDS dissociated all of the dye molecules from the CB-DA-TB dye complex, while the DW and EtOH did not. We examined which individual elements were associated with the proposed mechanisms at play in dye removal by CB-DA, including inorganic matter (principally magnesium) and other minor constituents such as  $\text{Na}^+(\text{NaCl})$ ,  $\text{Ca}^{2+}(\text{CaCl}_2)$  and  $\text{Mg}^{2+}(\text{MgCl}_2)$  in 10  $\mu\text{L}$  (1 mmol/L) of solution. The ion time-absorbance plots are presented in Fig. 2.1.4.C, revealing that competing ion complexation disrupts dye removal. It was found that the sorption of divalent cations ( $\text{Ca}^{2+}$ ,  $\text{Mg}^{2+}$ ) was more effective than was that of monovalent cations ( $\text{Na}^+$ ). We observed that the free ions enhanced the efficiency of CB-DA in terms of dye removal (Fig. 4C). To determine whether DE was unique in its ability to enhance the solubility of the CB nanocomposite, two other silica materials (silica sand and silica gel) were modified using the same method as for CB. Fig. 2.1.4.D indicates that CB-DA had a stronger effect than the other silica materials on TB dye removal. These results confirmed that high electrostatic interaction is an important factor in CB-DA dye removal and the natural diatom material supplies numerous ion elements that enhance its molecule-capturing properties.

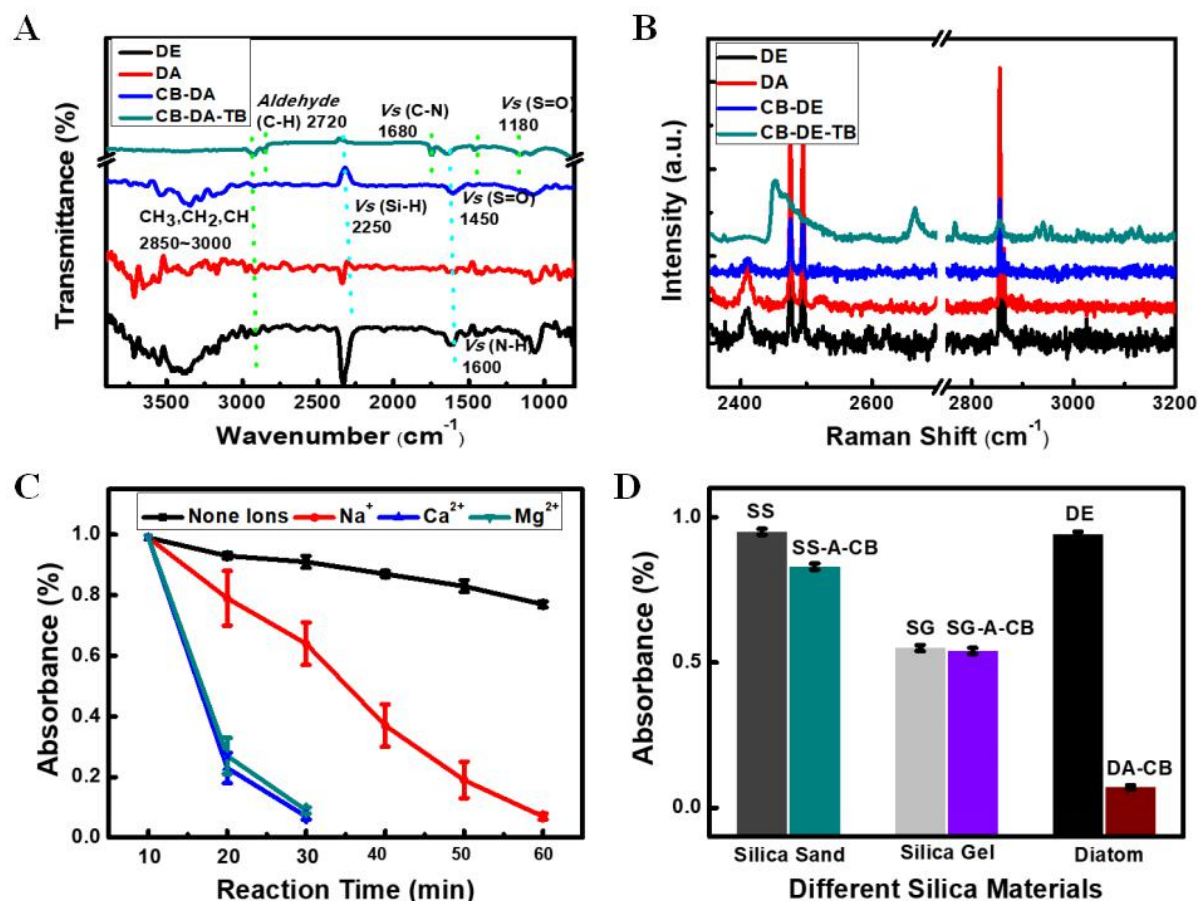


**Figure 2.1.4. Characterization of CB-DA**

(A) Fourier transform infrared (FTIR) spectrum analysis of the materials with dye. Pure DE (DE, black line), amine-modified DE (DA, red line), cucurbituril coated on amine-modified DE (CB-DA, blue line) and CB-DA with trypan blue dye (CB-DA-TB, green line). (B) Surface-enhanced Raman scattering (SERS) spectrum analysis of the materials with dye. (C) Ion time-absorbance plots to test the effect of ions on TB dye absorption. The error bars indicate the standard deviation from the mean based on at least three independent replications. (D) The absorbance of other silica materials with CB. Silica sand (SS), CB coated on SS (CB-SS), silica gel (SG), CB coated on SG (CB-SG), pure DE (D) and CB-DA. The error bars indicate the standard deviation from the mean based on at least three independent replications.



### **2.(3-1).6 Dye and pathogen removal testing**

To test the CB-DA conjugation with various dyes and pathogens, we used a mixed solution containing two dyes, rhodamine B and methylene blue. The absorbance curves for the amount absorbed per unit weight of CB-DA (Abs/mg) for the dye mixture are presented in Fig. 2.1.5.A. The CB-DA was effective at capturing the two types of dye molecule. Additionally, the CB-DA exhibited greater pathogen capturing ability compared to DE and DA only (Fig. 2.1.5.B). In particular, CB[8]-DA had the highest and most stable pathogen capturing ability. This similarity to the dye removal results indicates that the bulk capturing ability of CB-DA is related to the portals and cavity size of the CB molecules.

### **2.(3-1).7 Time-saving loading design**

As described above, CB-DA can be utilized for dye and pathogen removal within 4 h in aqueous applications. However, reducing the reaction time is an important factor in real-world water purification. Therefore, we applied 2 mg of CB-DA composites to a commercialized filter (1- $\mu$ m pore size) system in order to improve the purification time (Fig. 2.1.5.C-D). We added CB-DA to the surface of the filter with a pipette. The dye solution was then added to the filter. Separation clearly occurred within 2 min (Fig. 2.1.5.D). The absorbance rate and sedimentation time curves in Fig. 2.1.5.D confirm that CB-DA removed the dye rapidly and efficiently.

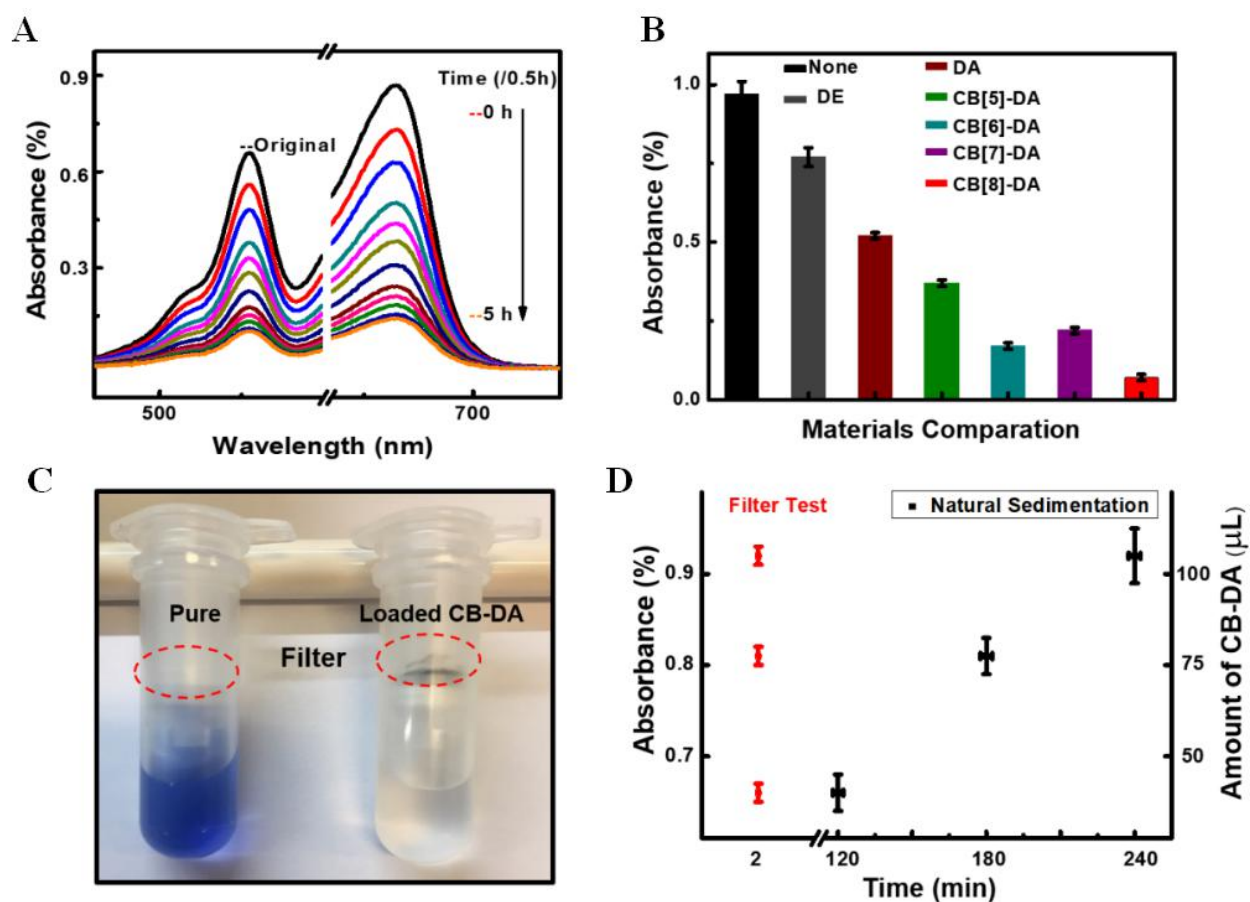


**Figure 2.1.5. Applications of CB-DA**

(A) Absorbance curves of the amount absorbed per unit weight of CB-DA (Abs/mg) for a mixture of rhodamine B and methylene blue dye. (B) The absorbance of supernatant after treatment with different CBs (CB[5], CB[6], CB[7] and CB[8]) with DA for pathogen removal. The error bars indicate the standard deviation from the mean based on at least three independent replications. (C-D) CB-DA applied to a filter system. This platform can remove dyes and pathogens within 2 mins. (D) Comparison of the CB-DA filter after 2 min and natural sedimentation after 4 h. The error bars indicate the standard deviation from the mean based on at least three independent replications.

**Table 3.** Comparison with other researches: the  $K_L$  , the absorbance constant, pH effect and reaction condition for the materials.

Material <sup>[a]</sup>	Tested	$K_L$ , <sup>[b]</sup>	Abs(%) <sup>[c]</sup>	pH effect	RC <sup>[d]</sup>
DE	MB, RB, RY	125 to 106	19~50%	--	48 h
CB[6]	PIC	6.1 to 3.6	39~80%		at 80 °C
CB[7]	PIN	2.7 to 3.0			
CB[7]	RhB	0.94 to 0.18	74~81%	Sensitive	at 88 °C
CB[8]	RB19	0.99 to 0.61	--		7 h
CB[6]					
CB-DA	TB	0.99 to 0.07	~92%	Stable	2 min at RT <sup>[e]</sup>
	MB, RhB		( RT )		
	Pathogen	--	~97%		

[a] Materials reference and our study CB-DA. [b] Langmuir constant (L/mg). [c] Absorbance constant of tested materials. [d] Reaction Condition. [e] Room Temperature.

(MB: Methylene Blue, RB: Reactive Black, RY: Reactive Yellow, RhB: Rhodamine B, PIC: Pseudoisocyanine, PIN: Pinacyanol, TB: Trypan Blue)

## 2.4.1 CONCLUSION

In summary, we developed a novel nanocomposite of highly stable, water-dispersible cucurbituril (CB) with amine-modified diatomaceous earth (DA) for use in molecular encapsulation in water purification. The CB coating the diatomaceous earth (DE) prevents the self-aggregation of CB due to its insolubility and enhances the ability of CB to capture molecules in solution. The key to the success of this approach is the presence of well-coated CB on the surface of the DA (CB-DA). This proposed approach leads to strong molecule host-guest interactions and an efficiency that is 100 times higher in terms of TB dye and pathogen removal, with excellent stability, recycling, and reusability. These properties of CB-DA, when applied to a filtration system, offer new avenues of development for water purification in terms of the rapid removal of unwanted molecules. Altogether, these useful properties suggest that the use of CB-DA-based filtration systems could be a promising platform for combining various CBs with DA of a controlled size. This proposed system could prove useful for many applications in aqueous solutions.

## **CHAPTER 2 An enhanced recyclable 3D adsorbent for diverse bio-applications using biocompatible magnetic nanomulberry and cucurbituril composites**

### **2.(3-2).1 Principle of MNM-DE-CB**

A novel two-step fabrication of MNM-DE-CB was developed (Fig. 2.2.1) to extend the usefulness of natural DE. First, DE with a uniform particle size distribution (10–25  $\mu\text{m}$ ) was thoroughly washed and combined with magnetic material using the traditional hydrothermal synthesis method. The structure and high magnetization of the synthesized magnetic nanomulberry-shaped CB on DE (MNM-DE) were confirmed by TEM in Fig. 2.2.1.A. Although an increase in the surface area of MNM-DE composites was expected, no significant changes occurred due to the facile coagulation of MNM-DE composites in solution (Fig. 2.2.1.B) possibly caused by interactions between magnetic forces on neighboring magnetized compounds. Further surface modification of MNM-DE was then implemented using super-molecular cucurbit[6]uril (CB[6]) to enhance the functionality of nanomaterial composites in aqueous solution. CB[6] solution was mixed with the prepared MNM-DE and boiled for 1 min using a microwave. After two-step fabrication, the structure of MNM-DE-CB was confirmed using SEM (Fig. 2.2.1.C). MNM-DE-CB dispersed much better in aqueous solution (Fig. 2.2.1.D) than MNM-DE (Fig. 2.2.1.B). In addition, the novel porous structure of MNM-DE-CB gained magnetization and enhanced the surface area of the composites. To confirm the improvements for MNM-DE-CB, we deduced that CB[6] powder gradually dissolved due to interactions with hydrophilic groups on the surface of MNM when insoluble CB[6] encountered MNM-DE in solution. A delicate dynamic system between CB and MNM-DE was evident, which also verified the improved dissolvability and dispersibility of MNM-DE-CB composites in aqueous solution.

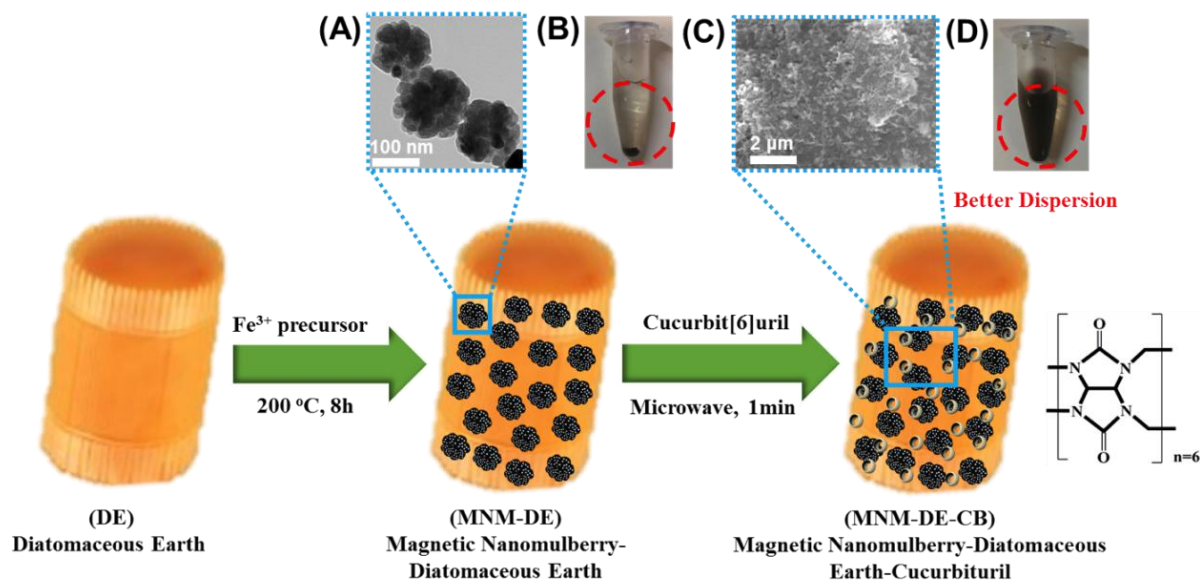


**Figure 2.2.1. Schematic illustration of the preparation of magnetic nanomulberry-diatomaceous earth-cucurbituril (MNM-DE-CB)**

(A) Transmission electron microscopy (TEM) image of MNM. Scale bar = 100 nm. (B) MNM-DE in aqueous solution. (C) Scanning electron microscopy (SEM) image of MNM-DE-CB. Scale bar = 2  $\mu$ m. (D) MNM-DE-CB in aqueous solution.

## 2.(3-2).2 Characterization and analysis of MNM-DE-CB

Next, the optimal synthetic ratio of Fe<sup>3+</sup> to DE was investigated to achieve good morphology, high magnetization, and an improved surface area for MNM-DE. A MNM-DE composite with a high magnetic saturation ( $M_s$ ) value and surface area was obtained (Fig. 2.2.2.A). Using a ratio of 0.2 (0.2 g of pure DE added to a 20 mL reaction system) Fe<sup>3+</sup> to DE for fabrication, we achieved MNM-DE composites with a maximum  $M_s$  value of 42.667 emu g<sup>-1</sup> and a maximum surface area of 27.67 m<sup>2</sup>/g (Fig. 2.2.2.A). The intensity of the magnetism of MNM-DE composites in a 0.1 ratio reaction system was higher than in a 0.3 ratio system, but overgrowth of MNM-DE caused self-aggregation, leading to mass adhesion and a decrease in the surface area of composites (Fig. 2.2.2.A). FTIR was employed to confirm the structural

composition of MNM-DE-CB. FTIR spectra of DE (Fig. 2.2.2.B, red curve) exhibited strong peaks at  $1088\text{ cm}^{-1}$  and  $796\text{ cm}^{-1}$ , representing stretching vibrations for Si-O-Si and vibrations for O-H<sup>38</sup>. After conjugation of MNM and DE, a peak appeared at  $588\text{ cm}^{-1}$  (Fig. 2.2.2.B, green curve), corresponding to Fe-O vibrations of MNM<sup>39</sup>. In spectra of pure CB (Fig. 2.2.2.B, black curve), peaks at  $2998\text{ cm}^{-1}$  and  $2922\text{ cm}^{-1}$  corresponded to stretching vibrations of C-H bonds for methylene. The peak at  $1470\text{ cm}^{-1}$  corresponded to methylene bending vibrations of C-H bonds. Finally, after conjugation of MNM-DE and CB, the aliphanyl C=O peak at  $1739\text{ cm}^{-1}$  for pure CB was shifted to  $1730\text{ cm}^{-1}$ , which implied the existence of hydrogen bonding between CB and MNM-DE<sup>40</sup>. Taken together, these results confirmed that the MNM-DE surface was successfully coated by CB. Next, the surface area and pore volume of MNM-DE-CB composites were characterized by N<sub>2</sub> sorption measurements at 77.3 K (Fig. 2.2.2.C). On one hand, the surface area and pore volume of MNM-DE-CB were calculated to be  $46.34\text{ m}^2/\text{g}$ , which was much larger than DE ( $2.05\text{ m}^2/\text{g}$ ) and MNM-DE ( $11.46\text{ m}^2/\text{g}$ ). On the other hand, the pore volume of DE ( $0.99\text{ m}^3/\text{g}$ ) was much larger than the pores volume of MNM-DE ( $0.06\text{ cm}^3/\text{g}$ ) and MNM-DE-CB ( $0.14\text{ cm}^3/\text{g}$ ) which confirmed that the MNM surface modification has filled the pore volume successfully. Although the surface area of MNM-DE was increased compared with DE alone, the useful surface area of MNM-DE was decreased due to facile aggregation by magnetic adsorption and surface physical adsorption. The surface area of MNM-DE-CB was therefore markedly increased by CB, which leads to improved stability and dispersibility of the 3D MNM-DE-CB complex in water. Meanwhile, nitrogen adsorption-desorption isotherm curves of DE (black line), MNM (red line), and MNM-DE-CB (blue line) confirmed differences in adsorption quantities (Fig. 2.2.2.D). All samples exhibited hysteresis loops at P/P<sub>0</sub> ranging from 0.4 to 1.0, indicating the existence of a mesoporous structure in the composites. By contrast, the blank hysteresis loop indicated few mesoporous structures in the pure DE samples. According to the typical type IV isotherm (IUPAC classification, blue)<sup>43</sup>, MNM-DE-CB composites are composed of mesoporous structures, resulting in the enhancement of water dispersibility and surface area.

Next, we measured the intensity of magnetism and the Zeta potential of MNM-DE-CB. The magnetic properties of MNM-DE, MNM-DE-CB, MNM-DE-CB-dye, and MNM-DE-CB (after washing with SDS) were investigated by VSM at room temperature (Fig. 2.2.2.E). The results revealed superparamagnetic behavior and minimal hysteresis, remanence, and coercivity because composites consisted of ultrafine magnetite nanocrystals.  $M_s$  values were 42.667, 40.052, 36.457, and 38.039 emu/g for MNM-DE, MNM-DE-CB, MNM-DE-CB-dye, and MNM-DE-CB (SDS wash), respectively. The  $M_s$  value for MNM-DE-CB (green curve) was slightly lower than that of MNM-DE (black curve), which might be due to the density of MNM in composites after modification with CB. It is worth noting that the modified composites still displayed strong magnetization (Fig. 2.2.2.E, inset), indicating high water dispersibility and stability for MNM-DE-CB during magnetic separation and targeting. In addition, the Zeta potentials of MNM-DE and MNM-DE-CB were measured by DLS (Fig. 2.2.2.F). The MNM-DE surface was coated by negatively charged ions, but MNM-DE-CB possesses positively charged ions on the surface. Based on these properties, the mesoporous structure of MNM-DE-CB may increase the physical adsorption of dye molecules. The positive charge distribution on MNM-DE-CB increased the uptake of dye molecules via electrostatic adsorption. In addition, the magnetic properties of the mesoporous magnetic nanomulberry-shaped  $\text{Fe}_3\text{O}_4$  make the MNM-DE-CB composites more useful in solution. Taken together, the results confirmed the advantages of MNM-DE-CB composites compared with other composites such as MNM-DE.



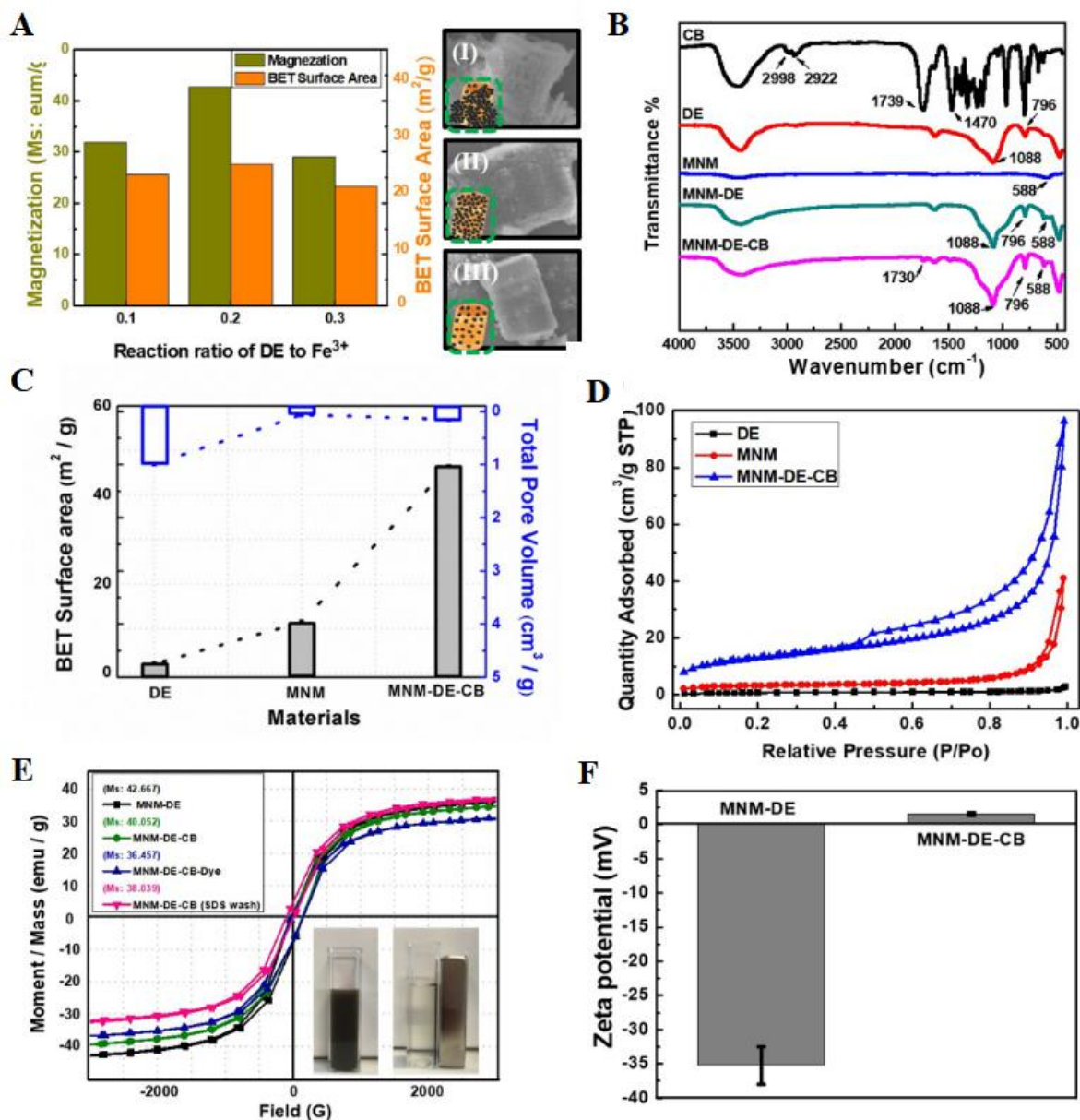


**Figure 2.2.2. Characterization of MNM-DE-CB**

(A) Magnetization, BET surface area, and SEM images of MNM-DE at three different reaction ratios of DE to Fe<sup>3+</sup>: 0.1 (I), 0.2 (II), and 0.3 (III). Samples of 0.3 g, 0.2 g, and 0.1 g pure DE were added to a 20 mL reaction system to obtain the desired ratio. (B) FTIR spectroscopy analysis of CB, DE, MNM, MNM-DE and MNM-DE-CB. (C) BET surface area and total pore volume of pure DE, MNM, and MNM-DE-CB. (D) Nitrogen adsorption-desorption isotherm curve analysis of prepared DE, MNM and MNM-DE-CB. (E) Magnetic hysteresis loops of MNM-DE, MNM-DE-CB, MNM-DE-CB-dye and MNM-DE-CB. (F) Zeta potential of MNM-DE and MNM-DE-CB.

### 2.(3-2).3 Efficient dye removal by MNM-DE-CB

To test the usefulness of MNM-DE-CB in aqueous solution, the dye removal efficiency of MNM-DE and MNM-DE-CB composites was investigated. For multiple dye removal experiments, dye solutions were measured using UV-visible spectroscopy after treating with MNM-DE or MNM-DE-CB for 1 h and rapid collection of composites by a magnet (Fig. 2.2.3.A). The adsorption efficiencies toward MB ( $C_0(\text{MB}) = 75 \text{ mg/L}$ ) and TB ( $C_0(\text{TB}) = 20 \text{ mg/L}$ ) for MNM-DE-CB composites were 6–7 times higher than those of MNM-DE. This indicates two interaction mechanisms between dyes and MNM-DE-CB, such as host–guest interactions and physical adsorption. The MNM-DE surface was found to be negatively charged (Fig. 2.2.2.F), which indicates that negatively charged MB and TB could not be adsorbed due to electrostatic repulsion. Therefore, the slight decrease in dye solution absorption intensity may be attributed to physical adsorption by the mesoporous structure of MNM-DE. On the other hand, the dye removal efficiency of MNM-DE-CB was higher than that of MNM-DE. Thus, the dye removal efficiency of positively charged MNM-DE-CB for negatively charged MB and TB could be enhanced due to electrostatic interactions.

Additionally, the distinct cavity structure may possess the ability to capture dye molecules in the presence of CB. To explore optimal conditions for MNM-DE-CB, the effects of metal cations on dye removal were examined (Fig. 2.2.3.B). Due to the range of effects of metal cations and pH on Trypan Blue (TB), we used the certain amounts of composites, and increased the initial concentration of TB. Various types of metal ions such as 0.01 M NaCl,  $\text{CaCl}_2$ , and  $\text{MgCl}_2$  were added to 1 mL MB (75 mg/mL) and TB (34 mg/mL) solutions containing MNM-DE-CB composites. All metal cations enhanced the dye removal efficiency of MNM-DE-CB composites, and sorption of  $\text{Ca}^{2+}$  cations proved most effective for removal of both dye molecules. Although we could not determine the specific reason, the removal efficiency of TB was improved (from 65.23% to 97%) much more than that of MB (from 78.86% to 85.39%; Fig2.2.3.B).

Furthermore, pH also plays a role in dye removal in aqueous solution. Since the color of MB changes from blue to red and eventually transparent between pH 9 and 14, we tested the removal rate of TB at different pH values. The adsorption efficiency of MNM-DE-CB gradually increased with decreasing pH from 10 to 2 (Fig. 2.2.3.C). This could be due to a switch from a positive to a negative charged surface of MNM-DE-CB from acidic to alkaline conditions, consistent with the Zeta potential values at different pH values (Fig. 2.2.3.D). In acidic and alkaline conditions, electrostatic interactions were more obvious due to significant changes in surface charge, resulting in an increase in adsorption capacity under acidic conditions, and a loss under alkali conditions.

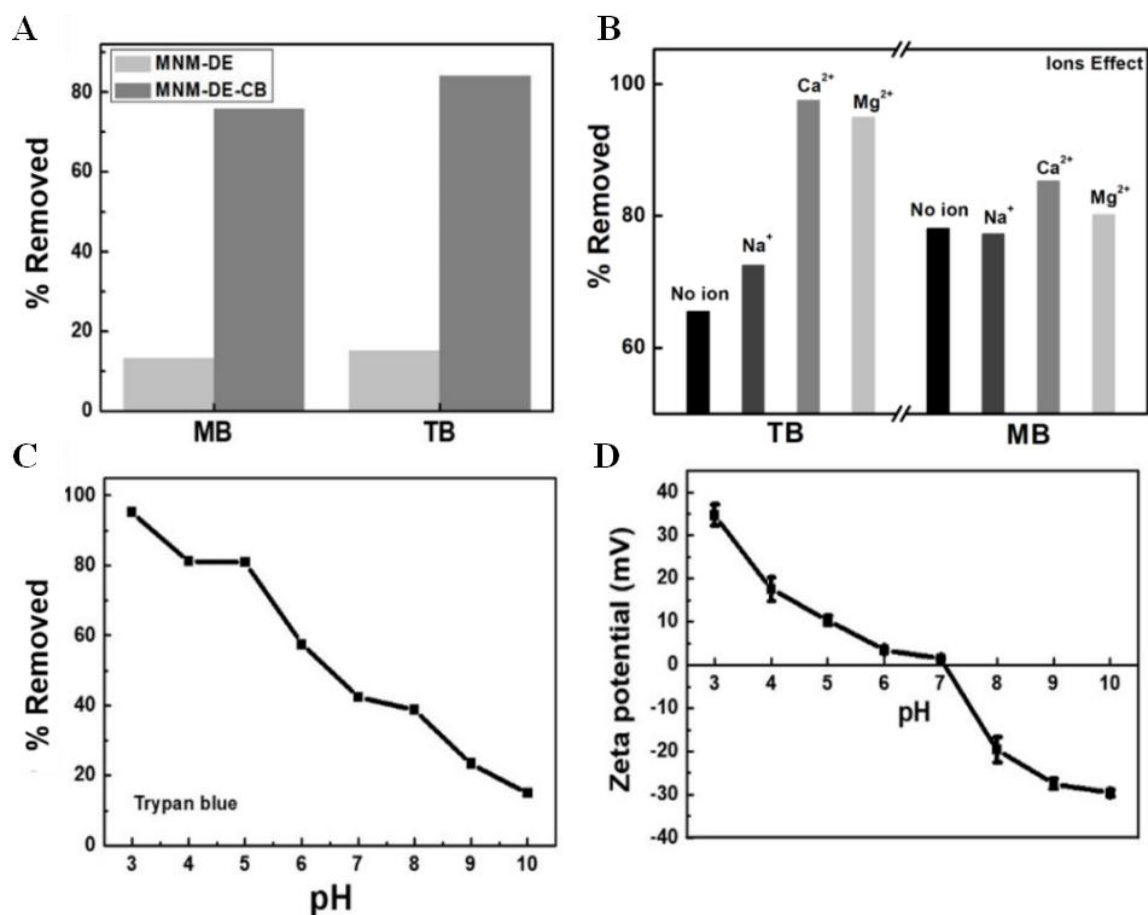


**Figure 2.2.3. Verification of MNM-DE-CB**

(A) Comparison of MNM-DE and MNM-DE-CB for dye removal:  $C_0(\text{MB}) = 75$  mg/L,  $C_0(\text{TB}) = 20$  mg/L, absorbent mass = 2 mg, pH = 7, volume = 1 mL, temperature = 25°C, contact time = 1 h. (B) Effect of metal cations on dye removal:  $C_0(\text{MB}) = 75$  mg/L, absorbent mass = 2 mg, pH = 7, volume = 1 mL, temperature = 25°C;  $C_0(\text{TB}) = 34$  mg/L, absorbent mass = 6 mg, pH = 7, volume = 1 mL, temperature = 25°C, 0.01 mL 0.01 M NaCl, CaCl<sub>2</sub>, MgCl<sub>2</sub>. (C) Effect of pH on TB removal:  $C_0(\text{TB}) = 73$  mg/L, absorbent mass = 8 mg, volume = 1 mL, temperature = 25°C, contact time = 1 h. (D) Zeta potential of MNM-DE-CB at different pH values. Error bars indicate standard deviation from the mean based on five independent replicates.

Next, we evaluated the effect of adsorbent dosage on dye removal. The removal rates for MB and TB were increased gradually with an increasing amount of adsorbent (Fig. 2.2.4.A-B). The maximum removal rates for MB (75 mg/L, 92.60%) and TB (20 mg/mL, 97.10%) were achieved in the presence of 5 mg and 10 mg MNM-DE-CB. The adsorption time for each dye was also evaluated (Fig. 2.2.4.C). The adsorption of both MB and TB was >90% within 1 h, and saturated within 6 h. The adsorption capacity ( $q_e$ ) of MB and TB was calculated to be 186.24 mg/g and 7.88 mg/g, respectively, using Eq. (2). The removal efficiency for TB was dramatically decreased with increasing temperature, but there was only a slight decrease for MB. These results are consistent with those of a previous report<sup>44</sup>. Adsorption of CB was not properly conducted at higher temperature because host–guest interactions are strongly exothermic (Fig. 2.2.4.D).

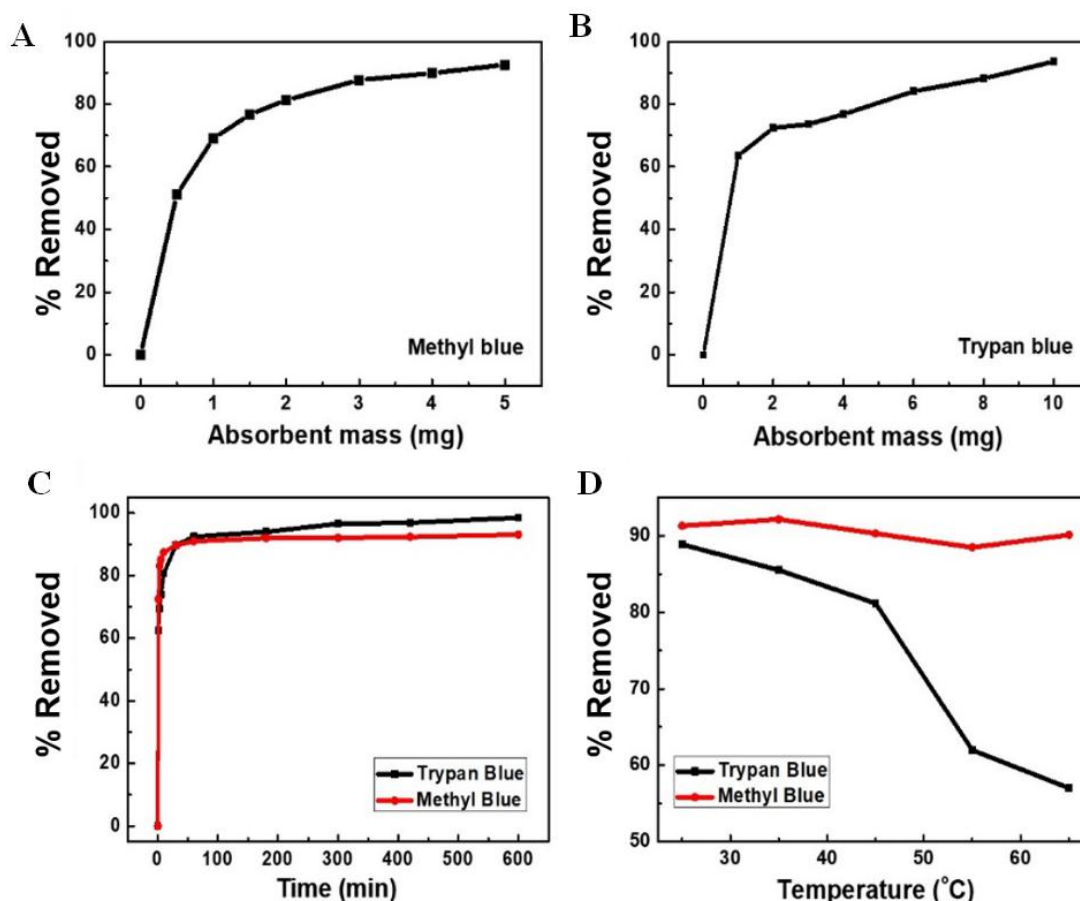


**Figure 2.2.4. Application of MNM-DE-CB**

Effects of dosage of MNM-DE-CB composites on dye removal for (A) Methyl Blue (MB) and (B) Trypan Blue (TB):  $C_0(\text{MB}) = 75 \text{ mg/L}$ ,  $C_0(\text{TB}) = 20 \text{ mg/L}$ ,  $\text{pH} = 7$ , volume = 1 mL, temperature =  $25^\circ\text{C}$ , contact time = 1 h. (C) Kinetics of MB/TB removal by MNM-DE-CB:  $C_0(\text{MB}) = 75 \text{ mg/L}$ , absorbent mass = 3 mg,  $\text{pH} = 7$ , volume = 1 mL, temperature =  $25^\circ\text{C}$ ;  $C_0(\text{TB}) = 67 \text{ mg/L}$ , absorbent mass = 8 mg,  $\text{pH} = 7$ , volume = 1 mL, temperature =  $25^\circ\text{C}$ . (D) Effects of temperature on dye removal:  $C_0(\text{MB}) = 75 \text{ mg/L}$ , MNM-DE-CB mass = 4 mg,  $\text{pH} = 7$ , volume = 1 mL, contact time = 1 h;  $C_0(\text{TB}) = 34 \text{ mg/L}$ , absorbent mass = 8 mg,  $\text{pH} = 7$ , volume = 1 mL, contact time = 1 h.

#### **2.(3-2).4 Reproducibility and large volume testing of MNM-DE-CB**

Due to the magnetic properties of the adsorbent, pollutants can be rapidly collected by a magnet, and adsorbed dyes and other molecules can be dissociated from the adsorbent using SDS. Fig. 2.2.5.A shows the process of absorption, dissociation, and efficient recycling with minimal secondary pollution and low energy loss. The reusability of MNM-DE-CB was evaluated using 10% SDS as the desorbing agent (Fig. 2.2.5.B). The dye removal efficiency was slightly decreased from 93.66% to 73.25% for TB, and from 92.60% to 74.25% for MB, after three uses due to incomplete dye removal from the surface of MNM-DE-CB. Meanwhile, the magnetic properties of the adsorbent did not change significantly after three times reuse, the  $M_s$  values showing in Fig. 2.2.5.C. we figured out that the MNM-DE-CB were good stability.

In addition, we performed MB removal testing at a larger volume scale (50 mL) to confirm the potential usefulness in various industries (Fig. 2.2.5.D). A 30 mg sample of MNM-DE-CB was used for MB dye (75 mg/L) removal. After reaction of MB and the adsorbent for 5 min, the adsorbent was collected using a magnet for 5 min. Within this time, the MB dye solution was almost 96% cleared ( $Abs_0$  from 1.057 to 0.094) at the 50 mL scale, indicating that the adsorbent achieved high water dispersibility and dye removal efficiency in the increased volume. These results demonstrate the acceptable reproducibility of MNM-DE-CB, as well as rapidity, simplicity, and low cost at a larger scale.

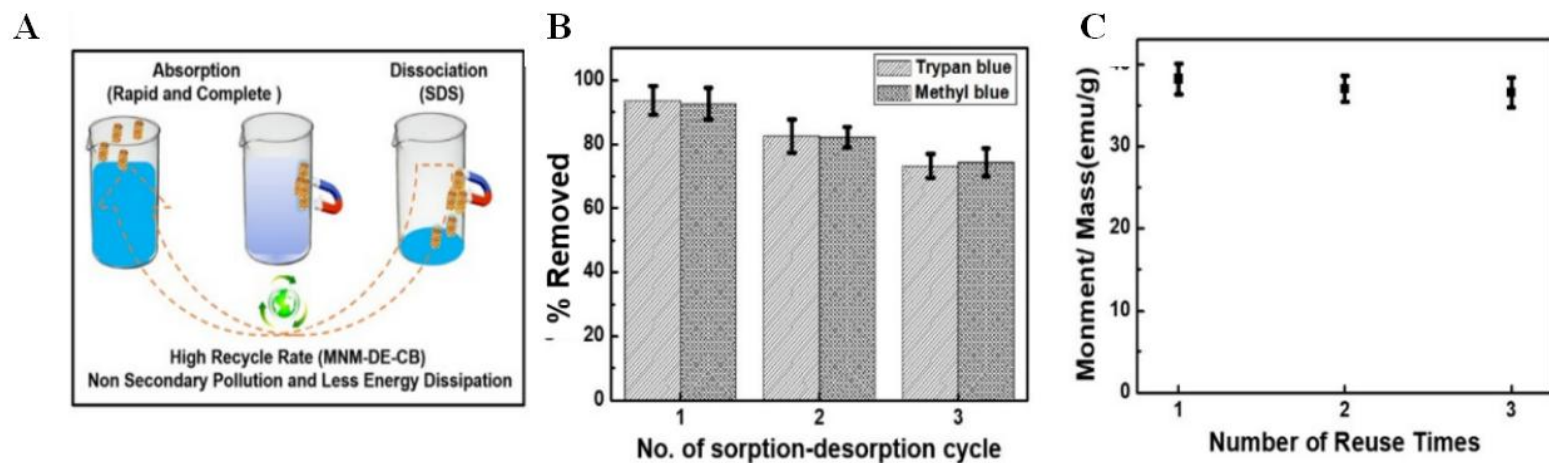


**Figure 2.2.5. Reproducibility and 50 mL volume testing of MNM-DE-CB composites**

(A) Diagram of dye removal and recycling by MNM-DE-CB. (B) Cyclic regeneration of MNM-DE-CB composites for TB and MB removal with 10% SDS as the desorption solvent. (C) Ms value of MNM-DE-CB following reuse.



D

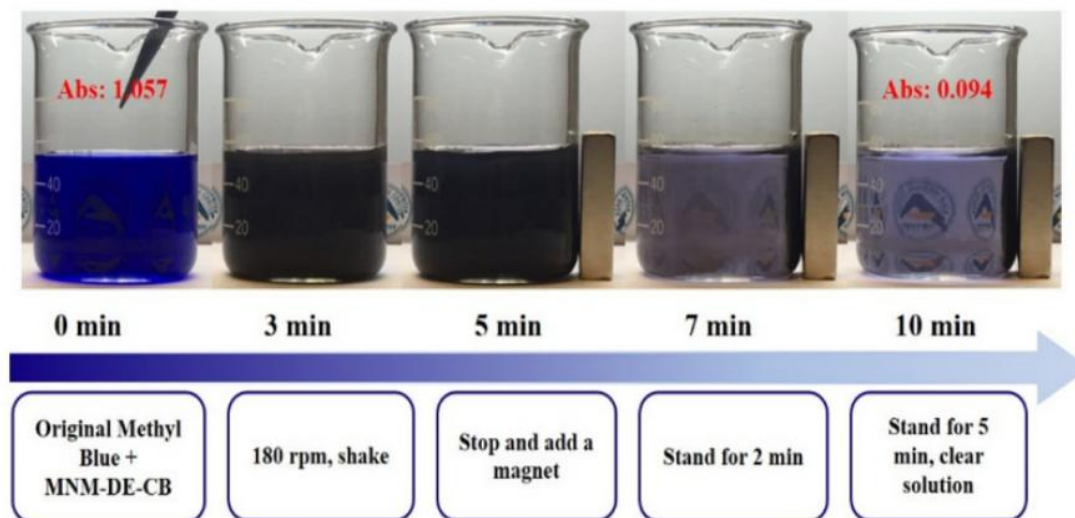


**Figure 2.2.5. Reproducibility and 50 mL volume testing of MNM-DE-CB composites**

(D) Dye removal by MNM-DE-CB: MB = 75 mg/L, absorbent mass = 30 mg, volume = 50 mL, temperature = 25°C.

### 2.(3-2).5 Biocompatibility and drug testing of MNM-DE-CB

The biocompatibility of nanomaterials is an essential property for biomedical applications, especially inherent toxicological issues<sup>45</sup>. In the present study, the cytotoxicity of MNM-DE and the MNM-DE-CB was evaluated using MTT assays in colorectal adenocarcinoma HCT-116 cells. A series of concentrations of MNM-DE and MNM-DE-CB ranging from 50 to 1000  $\mu\text{g/mL}$  were incubated with HCT-116 cells for 24 h. Cell viability was not adversely affected (83–97%) at concentrations up to 1 mg/mL for both composites (Fig. 2.2.6.A).

Meanwhile, to demonstrate the drug delivery applicability of MNM-DE-CB, we employed this adsorbent as a drug carrier with zinc phthalocyanine (ZnPC) as a drug delivery model. The absorption and release efficiencies for ZnPC with MNM-DE-CB were 81.89% and 96.84%, respectively (Fig. 2.2.6.B). When MNM-DE-CB-ZnPC was added to HCT116 cells, the viability of cancer cells was significantly decreased compared with MNM-DE-CB alone. Thus, MNM-DE-CB is a biocompatible and non-toxic material that could prove useful as a drug delivery system in clinical applications.

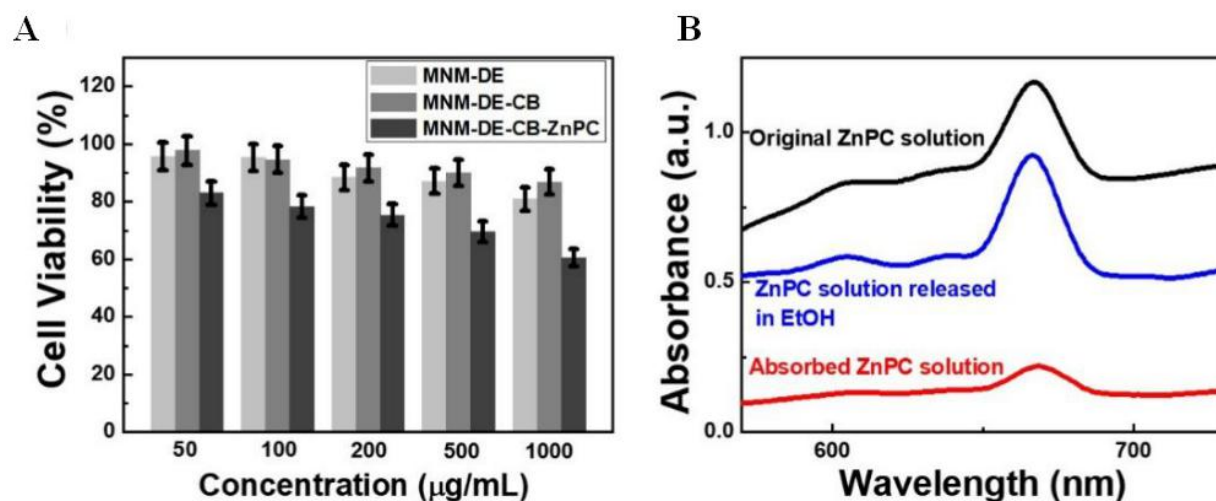


**Figure 2.2.6. Biocompatibility testing of MNM-DE-CB**

(A) Cytotoxicity testing based on cell viability after incubating with different concentrations of MNM-DE or MNM-DE-CB (B) ZnPC drug loading-release testing.

## 2.4.2 CONCLUSION

We herein demonstrate the synthesis of an adsorbent composed of magnetic functionalized DE and CB composites possessing rapid absorption ability and high solubility in aqueous solution. The MNM-DE-CB composite was synthesized by a two-step method that involved growing magnetic rods on the surface of DE, followed by CB coating through hydrogen bonds, which improved the solubility of MNM-DE in aqueous solution. The MNM-DE-CB composite is a highly water-dispersible and efficient adsorbent for the removal of dyes (MB and TB), possesses an increased surface area, and operates via three effective mechanisms: physical adsorption, electrostatic interactions, and host–guest interactions. Various potentially influential factors were investigated, and MNM-DE-CB displayed high adsorption capacity in acidic solution and in the presence of metal cations at room temperature. Using this novel adsorbent has a rapid turnaround time due to the ability to recover using a magnet, making it suitable for large sample volumes. Thus, it is a promising alternative for the removal of toxic pollutants in several industries including environmental remediation and drinking water preparation. In addition, *in vitro* cytotoxicity assays were performed to confirm that MNM-DE-CB composites behaved in a dose-dependent manner, and no significant cytotoxicity was observed, making them good candidates for drug delivery. The synthesis of MNM-DE-CB in the present work was at the milligram scale, and further study at the gram scale is needed to prepare for various applications. We believe that this strategy for preparing MNM-DE-CB will open a new avenue for reducing magnetic self-precipitation and facilitate the efficient utilization of super-molecular CB in aqueous applications. Specifically, the biocompatibility and effective molecular encapsulation ability of MNM-DE-CB may lead to uses in drug delivery. Meanwhile, with the absorption property and magnetic, the MNM-DE-CB could be applied on the fixed-point drugs treatment, such as bone space therapy and local cancer therapy.

## **CHAPTER 3 Facile Homobifunctional Imidoester Modification on Advanced Semiconductor Nanomaterials for Enhanced Antibiotic Synergistic Effect and Biocompatibility**

### **2.(3-3).1 Characterization of the ZnO NSs-HI**

The ZnO NSs were prepared through facile hydro-thermal method (Fig. 2.3.1.A), the uniform spindle-shaped ZnO NSs have been obtained through controlling the reacted-reagents ratio and stirring speed precisely. The activation energies of ZnO crystal growth at the booting of surfactant CTAB, and the special elementary layers (including compositions and thicknesses) of ZnO in hydro-thermal alkali solution resulting in the sharp sides and bulging middle structure of Nano Spindle ZnO (ZnO NSs, SEM image in Fig. 2.3.1.B). The size distribution data of our studied materials were obtained by DLS detection, the size of our synthesized ZnO NSs is mainly distributed in the region of 180~200nm (Fig. 2.3.1.C). In order to study the properties of our synthesized materials, a comparative study was carried out with commercial zinc oxide nanoparticles (ZnO NPs). Firstly, the independent single peaks in range of 340 nm to 410 nm from the UV-visible absorption spectra study have confirmed that our synthesized ZnO NSs is as pure as the commercial standard. And the relatively broad shape of the ZnO NSs peak has implied those special elementary layers which formed the nano shuttle morphology (Fig. 2.3.1.D). Following, the stability of their solutions have been studied through zeta potential which quantifies the electrical potential in the interfacial layers of the dispersed particle. Here (Fig. 2.3.1.E), compare with the incipient instability of commercial ZnO NPs (-20~-25 mV), our synthesized ZnO NSs are moderate stability (about +30 mV). We proposed that the ZnO NSs would like to be surface modifiable rather than redissolved which has been confirmed in the subsequent homobifunctional imidoester (HI) modification. As shown in the graphical synthetic route, dimethyl pimelimidate (DMP) and dimethyl suberimidate (DMS) have been studied with both commercial ZnO NPs and our

synthesized ZnO NSs, following ZnO NPs-HI and ZnO NSs-HI. Hereby, our synthesized ZnO has been supposed to be  $\text{NH}_2^+$  encircled (positive surface zeta potential) which could form the covalent bond with the imidoester functional group (Fig. 2.3.1.A). Through the study on UV–visible absorption spectra, we observed a red shift on the HI modification of ZnO NPs which may cause by the energy loss from the HI modification and an enlarged width of peak range which implied the morphology change of particles melting or aggregation (Fig. 2.3.1.F). On the contrary, there is not only no obvious morphology melting but also energy obtained (blue shift) of the ZnO NSs-HI (Fig. 2.3.1.G). Furthermore, the zeta potential study on the HI modification materials have substantiated the analysis on UV–visible absorption spectra study and been summarized in Fig. 2.3.1.H: the apparent zeta potential of ZnO NPs-HI reached to - 10 mV and the ZNO NSs-HI increased to +40 mV which confirmed the energy shift after HI modification (more energy, more activity). And with the inside graphs of the soluble ZnO NPs-HI and ZnO NSs-HI after standing for 30 mins showing the ZnO NSs-HI in white emulsion is better solubility than the ZnO NPs-HI. Meanwhile in the same detection system, the conductivity of ZnO NSs-HI is  $10^{-1}$  mS/cm, while commercial zinc oxide is only  $10^{-3}$  mS/cm, which also verified the energy obtained of ZnO nSs-HI, theoretically with stronger anti-pathogen efficiency.

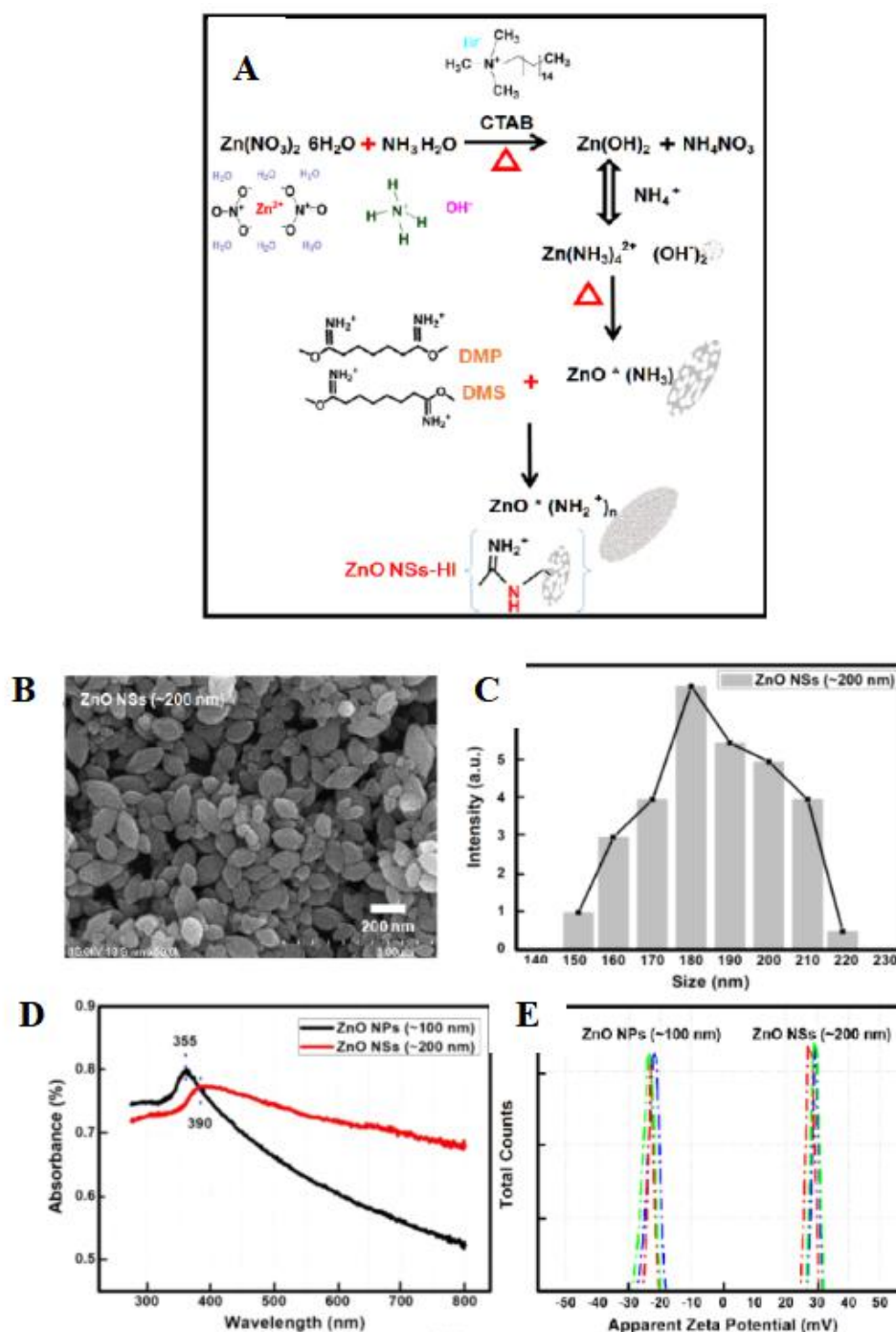
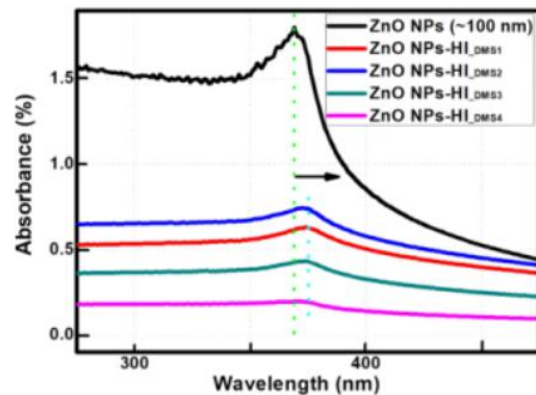


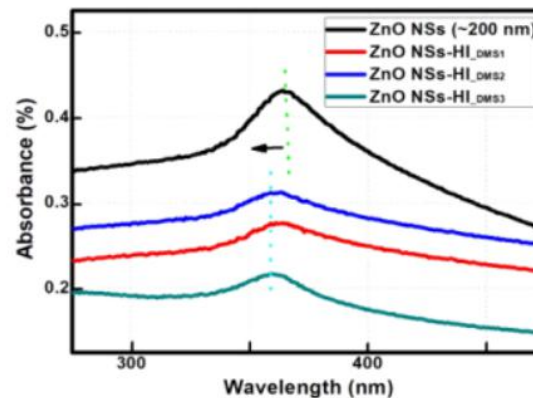
**Figure 2.3.1. Chemical characterization of our tested ZnO nanomaterials (ZnO NPs, ZnO NPs-HI, ZnO NSs and ZnO NSs-HI)**

(A) Schematic illustration of the structure and synthetic routine of ZnO NSs-HI; (B) SEM images of our synthesized in uniform nano-spindle structure, ZnO NSs (~200 nm); (C) DLS analysis of the size distribution of synthesized ZnO NSs; (D) UV-visible absorption spectra of our studied ZnO nanomaterials (ZnO NPs and ZnO NSs); (E) Zeta Potentials of our studied materials

F



G



H

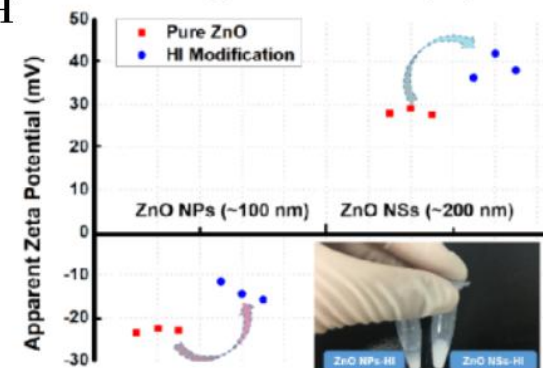


**Figure 2.3.1. Chemical characterization of our tested ZnO nanomaterials (ZnO NPs, ZnO NPs-HI, ZnO NSs and ZnO NSs-HI)**

(F) UV-visible absorption spectra of the ZnO NPs and the material after HI modification (ZnO NPs-HI) with a red shift; (G) UV-visible absorption spectra of the ZnO NSs and the material after HI modification (ZnO NSs-HI) with a blue shift. (H) Zeta Potentials study on the HI modification ZnO nanomaterials, inside with the graphs of the soluble material keep in standing for 30 mins.

## 2.(3-3).2 Bioapplications of the studied materials

Here the antibacterial efficiency of the ZnO NSs-HI has been confirmed with the model microorganisms (gram-negative bacteria *Escherichia coli* and *Salmonella*). The tested ZnO NPs, ZnO NSs and ZnO NSs-HI materials were added into the bacterial culture broth at different concentrations. After 12 hours of culture, the bacteria viability of each set has been studied in Fig. 2.3.2.A. The results show that the ZnO NSs-HI could inhibit the pathogen growth at concentration of 4 $\mu$ g/mL which is quite high efficiency in antibacterial system of ZnO nanomaterials (Fig. 2.3.2.A). By comparing the ZnO NPs and ZnO NSs groups, the antibacterial efficiency of ZnO NSs is better than that of ZnO NPs at the same concentrations, which may cause by the active surface property (positive surface charge is easily attract the bacteria) and physical form (sharp sides of the ZnO NSs pierces the bacteria). Those deductions have been reconfirmed by the observation of the lysis slides, the ZnO NSs fit closely with the *E.coli* cells (Fig. 2.3.2.B) instead of dispersed into the bacteria broth mixture like ZnO NPs.

In order to explore the antifungal efficiency and durability of the ZnO nanomaterials, two types of culture method have been executed on the fungi (*Aspergillus fumigatus*) in our study. Followed by our previous study, the same batch of *Aspergillus* has been diluted in 4 $\times$ 10<sup>4</sup> spores / mL and uniform standby. In the first drug-in agar method (Fig. 2.3.2.C), we mixed different concentrations of ZnO nanomaterials into the sterile agar, 200  $\mu$ L *Aspergillus* spores have been coated homogeneously. We traced the fungal colonization growing at 25 °C for 7 d, the drug concentration depended on fungal colony proportion has been summarized in Fig. 2.3.2.D. 4 types of ZnO nanomaterials (ZnONPs, ZnO NPs-HI, ZnO NSs and ZnO NSs-HI) have been added into the agar solution with concentration from 0.1 mg/mL to 1.0 mg/mL. The colony proportion of Day-7 showing that as increased of the drug concentration into agar, the viability of fungal spores decreased. The presence of drugs (ZnO NSs-HI) at a concentration of 0.4 mg/mL in agar exhibits an obvious inhibition and are even more effective than a higher concentration (0.6 mg/mL) of others. Moreover, the cultured



agar were bare at the concentration of 0.6 mg/mL ZnO NSs-HI (graphs in Fig. 2.3.2.C) which also demonstrated that the effect of ZnO nanomaterials is not only inhibited the growth of fungal spores but also killed the spores.

In another culture tested method, we mixed the drugs with the spores and spread plated in the normal agar plate. As shown in Fig. 2.3.2.E, the colony was planted in the center of agar and spread all around. Therefore, the growth rate of the fungal spores could be calculated by measuring the surface area of colony. Here we recorded the surface area of each tested colony (400 spores / dish with 0.01 mg/ mL drugs) day by day, the growth rate has been shown in Fig. 2.3.2.F. According to the growth rate of each drug (ZnONPs, ZnO NPs-HI, ZnO NSs and ZnO NSs-HI) treatment, the tendency showing that the vitality of the fungal spores within non-HI modification drug (ZnONPs and ZnO NSs) treatment was free from the inhibition as time goes on. However for the HI modification drugs (ZnO NPs-HI and ZnO NSs-HI), the growth rate is much slower than the others in the first 7 d and even come into a steady phase during the next 7 to 14 d. This phenomenon revealed that the antifungal property of ZnO nanomaterials are more durable after HI modification which may be caused by the activated surface energy. Meanwhile, it also verified that the enhanced surface energy from HI modification on ZnO nanomaterials is stable and permanently with high positive surface charge high conductive property (Fig. 2.3.2.H).

Furthermore, the SEM analysis (Fig. 2.3.2.D) confirmed the invasion of ZnO NSs-HI to fungal spores (surface contacting) and the possible ions attraction (non-contacting) which has visually the antifungal property of the bio ZnO NSs-HI.

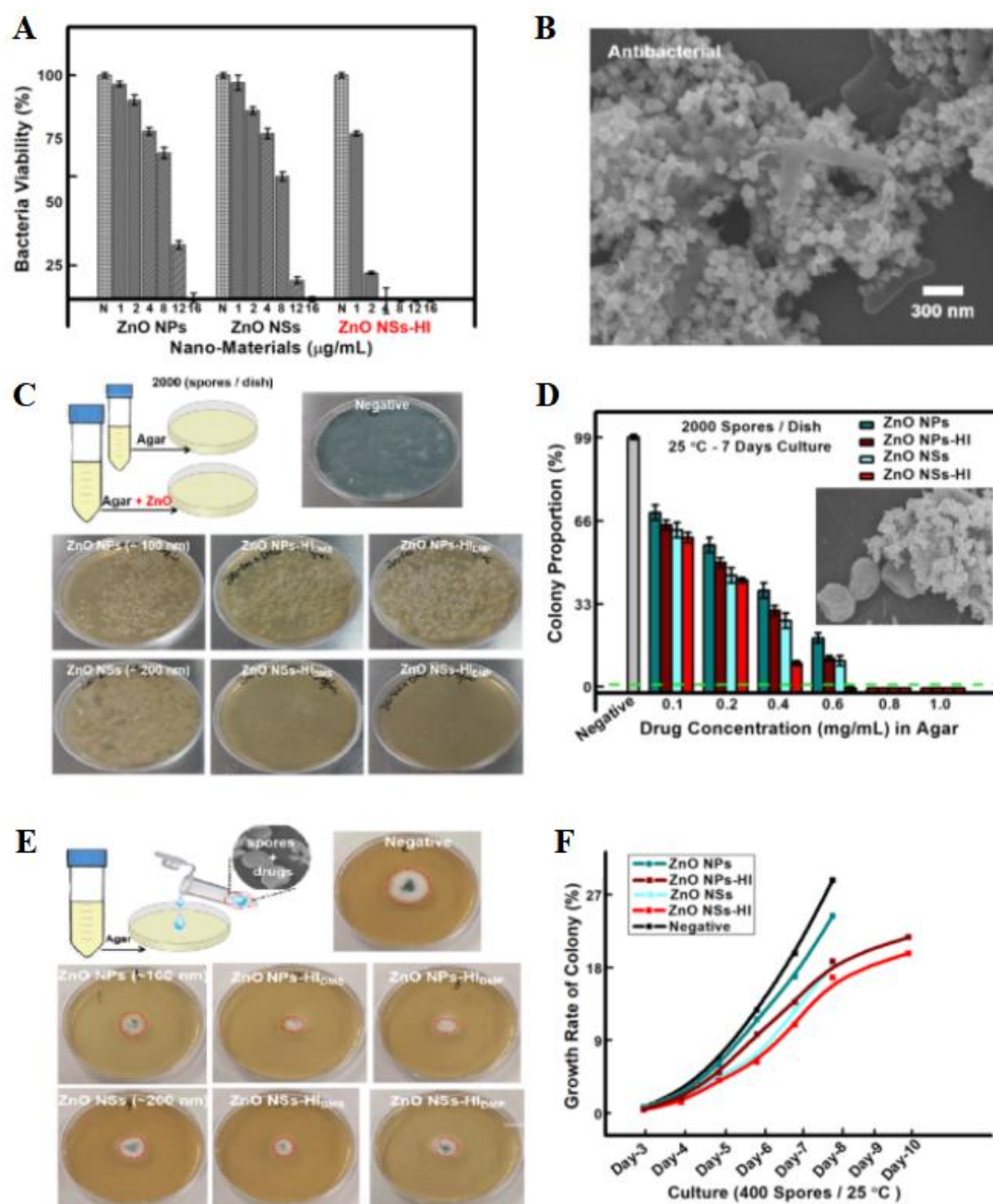


**Figure 2.3.2 Bioapplications (antibacterials and antifungal) of the studied materials (ZnO NPs, ZnO NPs-HI, ZnO NSs and ZnO NSs-HI).**

**Figure 2.3.2 Bioapplications (antibacterials and antifungal) of the studied materials (ZnO NPs, ZnO NPs-HI, ZnO NSs and ZnO NSs-HI).**

(A) Antibacterial efficiency of ZnO nanomaterials at different concentrations (1 ~ 16  $\mu\text{g/mL}$ ) tested on *E. coli* after 12 h incubation; (B) SEM image of ZnO NSs (~200 nm) lysis *E. coli*; (C-D) Illustration of the Spread Plate Method on studying the antifungal efficiency of ZnO nanomaterials (mg/mL, mix with agar plate), 2000 *aspergillus* spores / dish, 25 °C culture, after 7 d culture. (C) The graphs of the 7 days-cultured *aspergillus* colony with ZnO nanomaterials at 0.6 mg/mL; (D) The proportion summary of *aspergillus* colony at different concentrations (0.1 ~ 1.0 mg/mL) ZnO nanomaterials treatment; (E-F) Illustration of the Colony Formation Method on studying the antifungal efficiency of ZnO nanomaterials (0.2 mg/mL, 50  $\mu\text{L}$ ), 400 *aspergillus* spores / dish, 25 °C culture, tracking for 10 d culture. (E) The graphs of the Day-4 cultured *aspergillus* colony with ZnO nanomaterials; (F) The day-growth rate of *aspergillus* colony as tracked for 10 d. (Each data value means  $\pm$  SE of duplicate independent experiments)

### **2.(3-3).3 Antibacterial and synergistic antifungal effect of ZnO NSs-HI**

Firstly, refer to the mechanism study of nanomaterials on antibacterial that the semiconductor nanomaterials may cause oxidative stress by an effective antioxidant response in cellular we studied the cellular. Through the DCFAD-ROS kit test (Fig. 2.3.3.A), we found that i) the ROS intensity of our tested ZnO nanomaterials are 1.5 times higher than the normal cellular which is still in the safety cellular balance range of the oxidative stress; ii) after the HI (DMS and DMP) modification oxidative stress of L929 cellular is increased, but still in the adaptive cellular balance range. Growing evidence shows that the ROS caused by the ZnO nanomaterials (<2 times) is an adaptive balance in eukaryota cell due to the cellular stress response but it may cause mess in prokaryote cell.

Secondly, in order to study the ions effect on fungal growth, we designed the external ions assist experiment through subjoining the salt solutions as the effector with high (10 M, 10 $\mu$ L) and low (0.1 M, 10  $\mu$ L). Here the main object Zn<sup>2+</sup> has been provided through Zn (NO<sub>3</sub>)<sub>2</sub> and ZnCl<sub>2</sub>, the Na<sub>2</sub>CO<sub>3</sub> \ NaCl \ MgSO<sub>4</sub> \ (NH<sub>4</sub>)<sub>2</sub>CO<sub>3</sub> were set to eliminate interference. 1000 aspergillus spores per dish were cultured at 37 °C to simulate the biological environment, the Day 3 colonies have been summarized in Fig. 2.3.3.B, the result indicated that i) the Zn<sup>2+</sup> indeed plays an important effect in antifungal rather than the Na<sup>+</sup>, Mg<sup>2+</sup>, NH<sub>4</sub><sup>+</sup> etc and supplemented with high mol (10 M) of Zn<sup>2+</sup> is about double efficacy of the pure ZnO NSs; ii) the less effect of salt solution in low mol (0,1 M) reveals the self-protection of fungal spores. Meanwhile, we also tested the ions effect on ZnO NSs-HI, the Zn<sup>2+</sup> ions effect is not as obvious as on ZnO NSs which may cause by the coordinate covalent bonds between the imidoester functional groups and the acid radical ions (that could prolong the activity of Zn<sup>2+</sup>). The parallels happened in the pH effect, where we adjusted the broth with high acid, the antifungi efficient of ZnO NSs-HI was eliminated initiative (Fig. 2.3.3.C). However, when the pH test was arranged in agar medium, both the ZnO NSs

and ZnO NSs-HI maintained the excellent antifungal property. Three simulated pH under human body environmental conditions have been set as pH7.5 (Blood), pH 4.5 (Intestine) and pH 2.5 (Gastric). The superior antifungal activity of ZnO NSs-HI was demonstrated in each pH gradients substantiated that the ZnO NSs-HI could be potential medical ointment on the wound surface to innerendothecium (Fig. 2.3.3.D). Meanwhile, the maintained activity under the neutral blood pH medium also suggested the possibility of intravenous administration.

As the principle showing in Fig. 2.3.3.E, except the normal physical damage, we believe that the remarkable enhanced antifungal property of ZnO NSs-HI owes to activity imidoester functional groups which could help extend the life time of ROS and  $Zn^{2+}$  and damage the spore wall / membrane irreversibly. Compared with the traditional azole antibiotic (Itraconazole) which could inhibit the fungal growth through refraining the membrane to form cell membrane directly and easily causing antibiotic resistance, the broken in through the wall / membrane of ZnO NSs-HI has provided the new medical vision to enhance the efficiency of antibiotic and cut down the usage to decrease the probability of resistance mutation. The principle has been confirmed in the synergistic effect study of ZnO NSs with Itraconazole. After pretesting the efficiency of Itraconazole, we chose mild concentration (6  $\mu\text{g/mL}$ ) as the precursor to study whether the synergistic effect happens in cooperating with 0.1  $\text{mg/mL}$  ZnO nanomaterials. The diameter of *Aspergillus* colonies has been recorded day by day and shown in Fig. 2.3.3.F (the graphs of the aspergillus colony at Day 6) and Fig. 2.3.3.G (the growth trend chart). The results revealed that cooperating not only enhances antifungal efficiency but also shows persistence inhibition after 9 d of culture. Among, the ZnO NSs-HI showing better efficiency than ZnO NPs-HI which may be caused by the dynamic positive surface and large pores size of the synthesized ZnO NSs. Especially, the growth ratio booming after 6 d culture with both pure Itraconazole and pure ZnO nanomaterials respectively implied that those pure drugs lose their effectiveness to inhibit the newborn spores growing. However, the synergistic effect is remarkable between the ZnO NSs-HI and antibiotic Itraconazole also inspire that the ZnO NSs-HI solution could be the protection buffer or solvent

to lower the loss from solubility and adhering on container wall. Certainly, the assessment of its biocompatibility and toxicity would be the high impact factor for further medical application, such as ointment smear, orally and intravenous etc drug delivery systems.

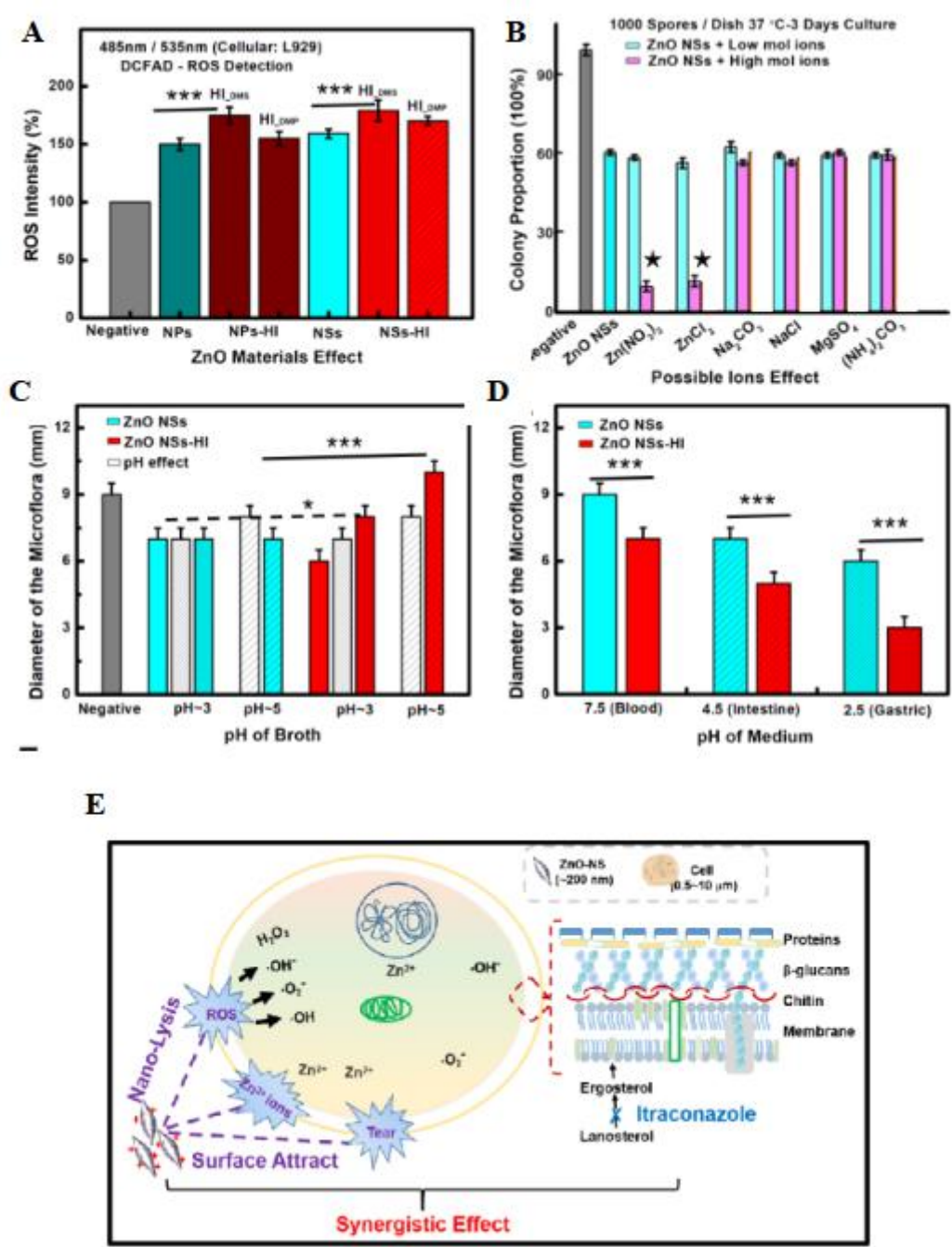
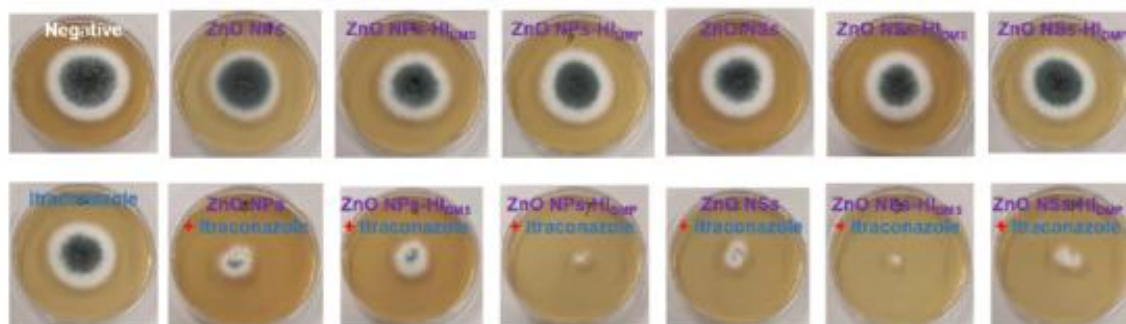
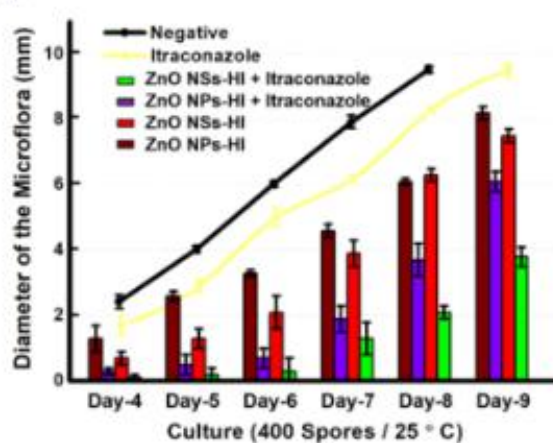


Figure 2.3.3. The bio-mechanism of ZnO NSs-HI with the antifungal properties

**F**



**G**



**Figure 2.3.3. Study on the bio-mechanism of ZnO NSs-HI with the antifungal properties**

(A) Cellular ROS detection assay of ZnO nanomaterials with L929. (B) Ions effect on the antifungal properties of the ZnO NSs through Colony Formation Method, 1000 aspergillus spores / dish, (0.1 mg/mL, 50  $\mu$ L) at 37  $^{\circ}$ C culture, after 3 d of culture. (C) Acid effect ( $H^{+}$ ) on the antifungal properties of the ZnO NSs and ZnO NSs-HI in Broth. (D) Modeling of the internal environment with pH medium. (E) Scheme of the hypothesized the antifungal mechanism of ZnO NSs-HI and proposed the synergistic effect with traditional antibiotic Itraconazole; (F-G) The synergistic effect study of ZnO NSs with Itraconazole. (F) The graphs of the aspergillus colony; (G) Day-record on the diameter of aspergillus colony as tracking for 9 d, 400 spores/Dish (ZnO nanomaterials: 0.1 mg/mL, Itraconazole: 6  $\mu$ g/mL, in 50  $\mu$ L), 25  $^{\circ}$ C -7 d of culture. (Each data value means  $\pm$  SE of duplicate independent experiments)

## **2.(3-3).4 Biocompatibility study with vitro blood and mice vivo test**

Dosage depended has been reported in many cellular toxicity studies of ZnO nanomaterials along with size effect and morphology effect. Although the ROS balance between the electron transport chain and the rate of scavenging by intracellular antioxidant pathways, blood biochemistry including platelet coagulation and subacute toxicity as an important indicator of biocompatibility study can not be ignored. As we mentioned, the imidoester functional group from HI modification involved in good biocompatibility which has minimal cross reactivity toward other nucleophilic groups in proteins and does not alter the surface charge of the protein, potentially retaining the native conformation and activity of the protein. Hereby, we investigated the vitro blood test to study the compatibility of HI modified ZnO nanomaterials where we used our designed fluid chip to simulate the endovascular environment and tested the materials with the fresh sheep blood (Fig. 2.3.4.A). The ZnO nanomaterials (NPs-HI and NSs-HI) have been added into the blood and kept the tube in silence for 10 mins. We found that the ZnO NSs-HI was precipitated into the tube (Right tube) while the ZnO NPs-HI tube was unclear (Left tube). Without clear precipitation indicated that the ZnO NPs-HI looks like fusion with the blood cell which may result in cell toxicity and coagulation blocking. Meanwhile, we flowed the mixture through the flexible and thin fluid chip (Length: 45 cm; Volume: 350  $\mu$ L) and detected the amount of ZnO loss during the flowing through the Uv-vis spectroscopy (Biochrom, Libra S22). Referred to the lowest velocity of human venous flow ( $\sim$ 7 cm/s), we set the pump at 500  $\mu$ L/min to get a lower flowing speed at 1 cm/s. The collected data shown in Fig. 2.3.4.B, there was less loss in the ZnO NSs-HI system than the ZnO NPs-HI system. We inferred that the HI modification helps the ZnO NSs-HI more neat within the thick blood plasma and the fairshaped lets the ZnO NSs-HI lower flow resistance and flow flexibly. Furthermore, we observed that ZnO NSs-HI coagulated with the blood cells and lots of ZnO NPs-HI attached to the cells in the superstratum under the upright microscope (Fig. 2.3.4.C), however the cell condition of the ZnO NSs-HI were quite fine and clear (Fig. 2.3.4.D). Therefore, we



confirmed that the HI modification and special shape of ZnO NSs-HI lets it be a good biocompatibility candidate in the intravenous administration.

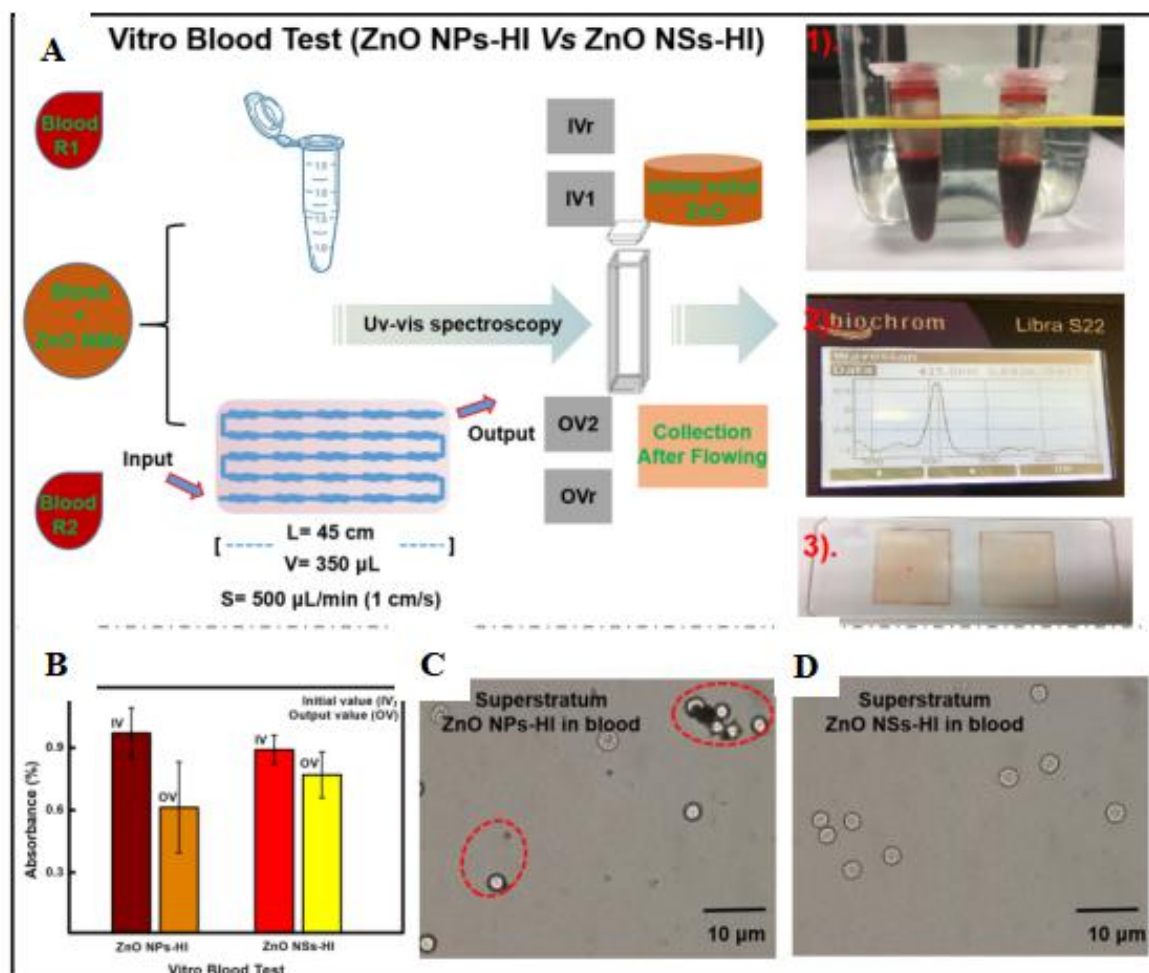


**Figure 2.3.4. Study on the biocompatibility and toxicity of ZnO NSs-HI in vitro blood test.**

(A) Scheme of the vitro blood test; (B) The absorbance of the initial value and output value of ZnO nanomaterials after the vitro blood test; (C-D) The upright microscope images of the superstratum in ZnO NPs-HI and ZnO NSs-HI system. (Each data value means  $\pm \text{SE}$  of duplicate independent experiments)

We next evaluated the in vivo toxicity of the ZnO NSs-HI with compliance of the local ethics committee. After intravenous administration, the clinical signs of toxicity including tremors, convulsions, salivation, nausea, vomiting, diarrhea and body weight change of the mice have been recorded for 14 d. There was no death that occurred at both dosages. And also there is no significant alteration in weight and toxicity symptom of all the mice with both low dosage and high dosage administration groups (Fig. 2.3.5.A-B). In particular, the condition of the remarkably toxins-elimination organs have been evaluated carefully in Fig. 2.3.5.C (kidneys) and Fig. 2.3.5.D (livers), both of them were in health conditions. The blood biochemistry study of the sacrificed mice shown that there were no big waves of both Alanine Transaminase (ALT) and Aspartate Aminotransferase (AST) which are reliable tests for liver damage; Bilirubin test for the bile; Blood Urea Nitrogen (BUN) and Creatinine (Crea) are in a relationship with the working well of kidneys. Meanwhile, Total Protein (TP), Albumin and the ratio of albumin/ globulin (A/G) which are useful to estimate qualitative change of lipoproteins and keep the blood from leaking out of blood vessels, stable means health (Fig. 2.3.5.E); and the wave changes of Total Cholesterol (T-Chol), Triglyceride (TG), Glucose and Phosphorus etc are in normal means (Fig. 2.3.5.F). All of these results indicated that there were no signs of toxicity in the mice treated with low or high doses of ZnO NSs-HI by intravenous administration in vivo. These findings suggest the ZnO NSs-HI composites are relatively safe for biomedical applications.

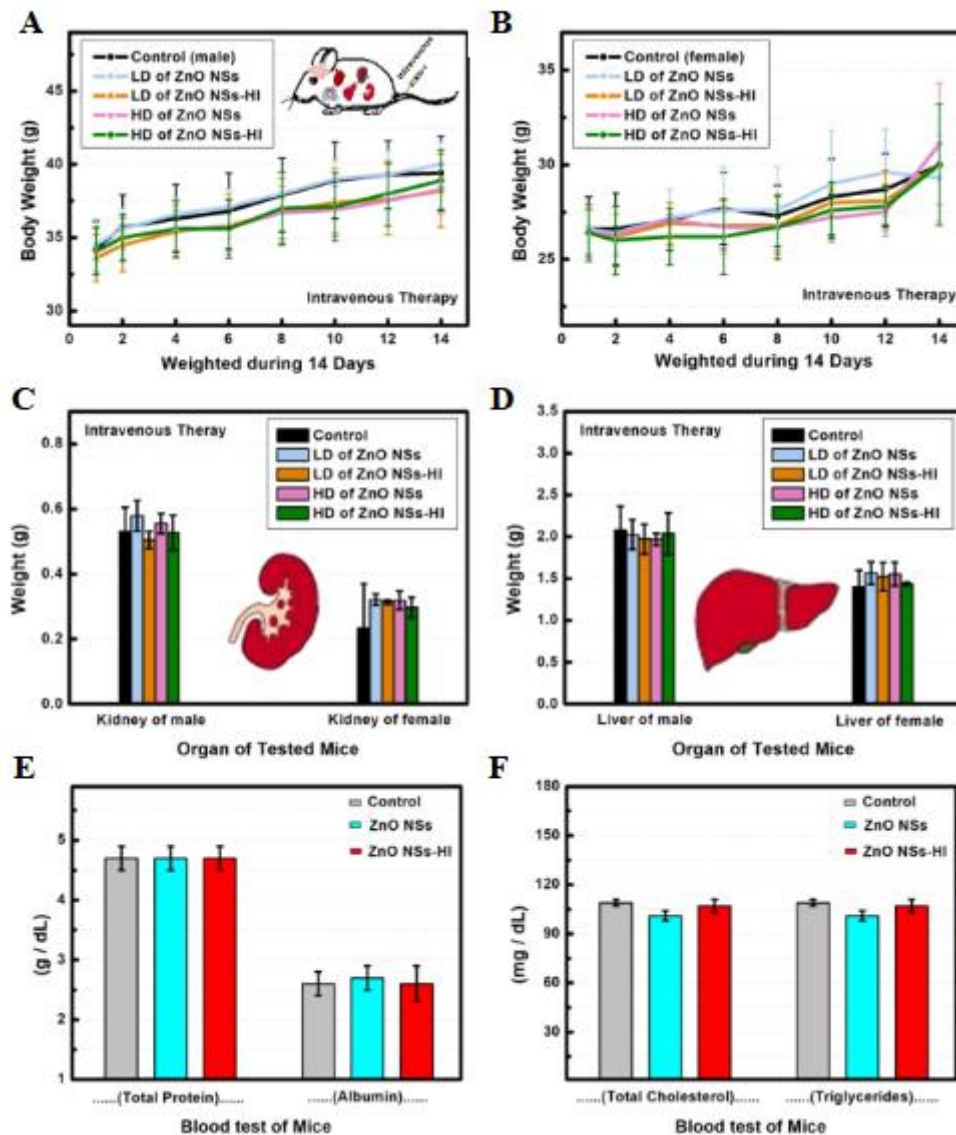


**Figure 2.3.5. Study on the biocompatibility and toxicity of ZnO NSs-HI in vivo.**

(A-B) Body weight changes of the mice treated with LD and HD of ZnO NSs or ZnO NSs-HI by intravenous administration, monitored for 14 d, A: male; B: female;

(C-D) Major organs weight changes of (C) kidney and (D) liver of mice after 14 d of intravenous administration with LD and HD of ZnO NSs or ZnO NSs-HI;

(E-F) The blood biochemistry study of the sacrificed mice (E) Total Protein (TP), Albumin and (F) Cholesterol (T-Chol), Triglyceride (TG). (Each data value means  $\pm$  SE. (n = 10 mice per group). Abbreviations: LD, low dosage; HD, high dosage)

### 2.4.3 CONCLUSION

In this study, we synthesized the facile homobifunctional imidoester modified semiconductor composites (ZnO NSs-HI) and demonstrated the antibiotic efficacy and persistence of ZnO NSs-HI against fungi and Gram-negative bacteria. Based on our study of its morphological changes, we observed that the ZnO NSs-HI composites strongly bound to the pathogen's membrane and disrupted its membrane morphology and the specific acylating groups available from biocompatible HI modification has minimal cross reactivity toward other nucleophilic groups in proteins. Under with multiple experiments of ions control and condition effect, we demonstrated several possible mechanisms whereby ZnO NSs-HI enhances antibiotic activity and persistence against fungi (*A. fumigatus*) and Gram-negative bacteria (*E. coli*) and summary in Figure 3E. Generally, disruption of the fungal cell wall is more difficult than for other pathogens, which subsequently leads to low antibiotic effects. However the remarkable enhanced antifungal property of ZnO NSs-HI owes to activity imidoester functional groups which could help extend the life time of ROS and  $\text{Zn}^{2+}$  and damage the spore wall / membrane irreversibly. Compared with the traditionalazole antibiotic (Itraconazole) which could inhibit the fungal growth through refraining the membrane to form cell membrane directly and easily causing antibiotic resistance, the broken in through the wall / membrane of ZnO NSs-HI has provided the new medical vision to enhance the efficiency of antibiotic and cut down the usage to decrease the probability of resistance mutation.

Meanwhile, we evaluated the toxicity of ZnO NSs-HI through the designed vitro blood test and blood biochemistry study after intravenous administration to mice. While further studies are desirable to fully establish the safety of ZnO NSs-HI in mice and humans, we observed the composite was safe at experimental dosages when administered to mice for two weeks. Their organs had normal weights and their blood chemistry was normal as compared to the controls.

Our results have shown that this non-toxic ZnO NSs-HI can be used as an antibiotic agent against fungi and Gram-negative bacteria in a clinical setting. Moreover, the

ZnO NSs-HI has a porous structure, which can be efficiently loaded with another antibiotic agent, so they can also be used as carriers for drug delivery. Hence, given recent advances in the surface chemistry of nanomaterials, future study will focus on drug delivery systems containing ZnO NSs-HI to develop efficient therapies against target sites in various clinical applications. Therefore, we envision ZnO NSs-HI can be used to enhance the mode of action of antibiotics against fungi and bacteria, and thus will be useful as novel antibiotic agents for fighting antimicrobial infections.

## **CHAPTER 4 A Diatom Earth Framework Semiconductor Composite Assisted Antibiotic with Enhanced Efficacy and Therapy Persistence in Nano-therapy**

### **2.(3-4).1 Synthesis and characterization of the DE-ZnO**

First, in order to synthesize ZnO-S (~300 nm) through facile hydro-thermal method (Fig. 2.4.1.A), we optimized the one-pot method which reduce the cost of synthesis production using the zinc contains with 98% SiO<sub>2</sub>. The properties of our synthesized ZnO-S (~300 nm) were referred to commercial ZnO nanomaterial [named ZnO-C (~100 nm) and ZnO-C (~5000 nm)]. Through UV-visible absorption analysis (Fig. 2.4.1.B), the characteristic peak at 381 nm confirmed the ZnO and the half-peak angles of the black (ZnO-C ~100 nm) and red (ZnO-S ~300 nm) spectrum show the uniform structure form. The morphology of these nanomaterials (ZnO-S in Fig. 2.4.1.C) was confirmed by scanning electron microscopy (SEM). Then, the surface performance of these nanomaterials was confirmed by Zeta potential (Fig. 2.4.1.D). The special positive surface charge of the synthesized ZnO-S occurred by coating it with NH<sub>4</sub><sup>+</sup> groups.

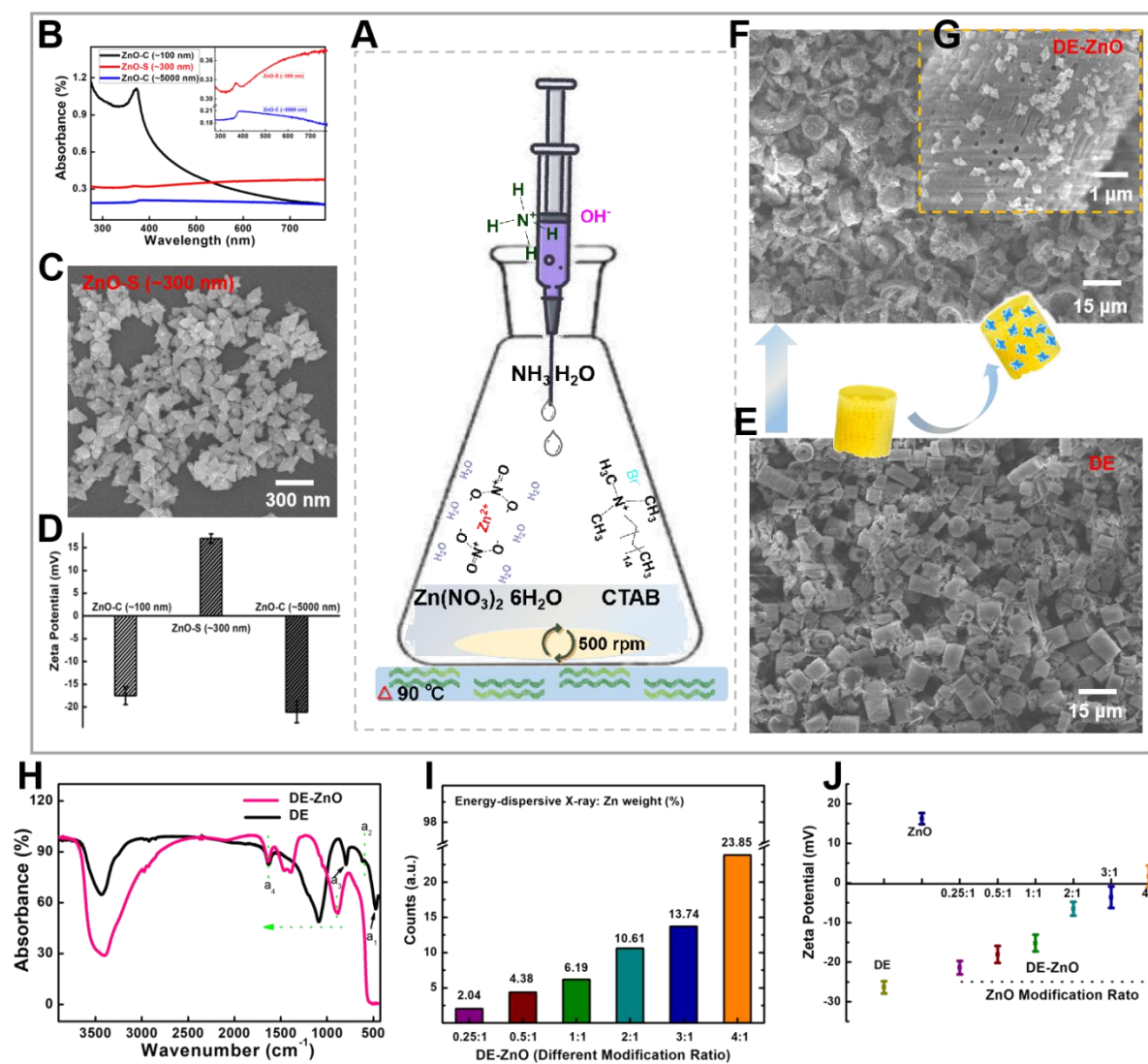


Figure 2.4.1. Mild-simple synthesis procedure and chemical characterization of the bio-inspired semiconductor nano-composite (DE-ZnO).

**Figure 2.4.1. Mild-simple synthesis procedure and chemical characterization of the bio-inspired semiconductor nano-composite (DE-ZnO)**

(A) Illustration of the mild-simple synthesis procedure of DE-ZnO in middle of the graphic and surrounding with the property characterization. (B) UV-visible absorption spectra for ZnO nanomaterials (ZnO-S, commercially available ZnO nanomaterials; ZnO-C (~100 nm) and ZnO-C (~5000 nm)). (C) SEM images of ZnO-S (~300 nm). (D) Zeta potential of the ZnO nanomaterials. (E) SEM image of the precursor diatomaceous earth (DE). (F) SEM images of the product semiconductor nano composites DE-ZnO, inside (G) is the amplification SEM image of the DE-ZnO surface. (H) FTIR spectra of DE-ZnO nanocomposites and pure DE. (I) Energy-dispersive X-ray of DE-ZnO at different modification ratios of ZnO:DE = 0.25:1; 0.5:1; 1:1; 2:1; 3:1; and 4:1, the percentage of ZnO are 2.04%, 4.38%, 6.19%, 10.61%, 13.74% and 23.85%, respectively. (J) Zeta potentials of DE-ZnO composites depend on the different ratios of ZnO on DE (ZnO:DE = 0.25:1, 0.5:1, 1:1, 2:1, 3:1, and 4:1). Error bars indicate the standard error of the mean based on at least three independent experiments.



Finally, to maximize the efficacy and persistence of its antibiotic activity, we designed a novel non-toxic composite (called DE-ZnO) combined with ZnO-S and frustules diatomaceous earth (DE, Fig. 2.4.1.E), which has a naturally assembled amorphous silica architecture with countless nanosize pores and abundant active hydroxyl groups on its substantial surface. A DE framework semiconductor composite (DE-ZnO) is obtained due to the precursor  $\text{Zn}^{2+}$  settling on the DE due to the surfactant (CTAB) using the facile hydro-thermal method (Fig. 2.4.1.F). The ZnO-S is well distributed across the surface of DE (Fig. 2.4.1.G). Hence, several *in vitro* and *in vivo* tests were conducted to verify the performance of the DE-ZnO composites. To confirm the properties of the bio-inspired DE-ZnO composites, the FTIR of the DE and DE-ZnO composites was tested (Fig. 2.4.1.H). The missed peaks of DE-ZnO at  $a_1$  495  $\text{cm}^{-1}$ ,  $a_2$  650  $\text{cm}^{-1}$ , and  $a_3$  750  $\text{cm}^{-1}$  as compared with DE were caused by modification with the  $\text{NH}_4\text{OH}$  reaction. On the other hand, the interaction between the grown ZnO and DE framework were confirmed with the red shift. The decreased wavenumber shows that the DE-ZnO (1152  $\text{cm}^{-1}$ ) composites are much more active than pure DE (1152  $\text{cm}^{-1}$ ). Next, to optimize the reaction ratio between the ZnO and DE, the parallelism reaction ratios of  $\text{ZnO:DE} = 0.25:1$ ;  $0.5:1$ ;  $1:1$ ;  $2:1$ ;  $3:1$ ; and  $4:1$  were examined. The energy-dispersive X-ray of the DE-ZnO showed that the percentages of ZnO on the DE are 2.04%, 4.38%, 6.19%, 10.61%, 13.74%, and 23.85%, corresponding to each parallelism reaction ratio (0.25, 0.5, 1, 2, 3, and 4), respectively (Fig. 2.4.1.I). Meanwhile, the parallelism zeta potential of the DE-ZnO composites confirmed that the surface charge of the DE-ZnO was positive and correlated with the amount of coated ZnO-S (Fig. 2.4.1.J). Due to the well-washed DE having a negative surface charge and the synthesized ZnO-S having a positive surface charge, the DE-ZnO composites can be changed to a positive charge by adding a sufficient amount of ZnO-S. Thus, the integral surface charge of the DE-ZnO composites could be neutralized between the substrate DE (-) and the growing ZnO-S (+), which were mainly owing to the natural stable property of the DE and the semiconductor properties of ZnO-S. Based on these results, the DE-ZnO composites were well-conjugated.

## 2.(3-4).2 Antibacterials study of DE-ZnO

Using the DE-ZnO composites, we tested their antibacterial effect against Gram-negative bacteria (Fig. 2.4.2.A). For these tests, a suspension of Gram-negative bacteria (*E. coli* and *S. enterica*) was used to evaluate the antibacterial activity of 10 µg/mL DE-ZnO with a parallelism reaction ratio. The DE-ZnO composites were added into a medium tube containing  $1 \times 10^7$  CFU/mL bacteria (*E. coli* or *S. enterica*) suspension. After incubation for 16 h at 37 °C shaking at 210 rpm, the optical density of each sample at OD 600 nm was measured to check for bacterial viability. The results showing that the antibiotic effect of DE-ZnO composites were enhanced as the ratio of ZnO increased, the higher ratio of the DE-ZnO composites showed higher antibacterial properties than the others. In Fig. 2.4.2.B, the DE-ZnO composites absorbed the bacteria entirely which could facilitate to break the cell membrane in a minimum area.

Due to the high toxicity of commercial drugs, the effective treatment of patients with fungal and bacterial infections has been extremely limited. Thus, we investigated the cytotoxicity of DE-ZnO at different modification ratios through Cell counting Kit 8 method with the non-cancerous L929 cell (Fig. 2.4.2.C). The cell viability is relatively stable (70~60%) at the 10.61% (2:1) ratio of DE-ZnO and is little affected at amounts up to 3 mg (Fig. 2.4.2.D), which is the higher dosage of of the DE-ZnO composite for *in vitro* study. In order to further explore the efficiency and biocompatibility of DE-ZnO, we performed a DCFDA-DA Cellular ROS detection assay for measurement of ROS in cellular and non-cellular environments containing the DE-ZnO composites. A simple schematic diagram showing in Fig. 2.4.2.E for cellular environment testing, esterases cleave DCFH-DA at two ester bonds, which could produce a relatively polar and cell membrane-impermeable product (H<sub>2</sub>DCF), this non-fluorescent molecule accumulates in cells and subsequent oxidation yields the highly fluorescent product DCF. In non-cellular environments, when reverse detection was applied, a fluorescent DCF solution was prepared and its fluorescence intensity was protected in the presence of ROS. The redox state of the sample can be monitored

by detecting the intensity of the fluorescence in the presence of ZnO-S. We observed that the ROS from DE-ZnO composites can be induced when it interacts with cells (Fig. 2.4.2.F). In the non-cellular study, the pure DE did not affect the fluorescence of DCF, but the presence of DE-ZnO composites did slow down the speed of fluorescence quenching (Fig. 2.4.2.g). Then, the DE-ZnO composites with different ratios of ZnO modification ( $\text{ZnO:DE} = 0.25:1, 0.5:1, 1:1, 2:1, 3:1, \text{ and } 4:1$ ) were compared, and the ZnO amount-effect on ROS release was verified (Fig. 2G). We performed a non-cellular DCF fluorescence study with the DE-ZnO (0.1 to 2.5  $\mu\text{g/mL}$ ) composites (Fig. 2.4.2.e) and the pure ZnO-S (0.05 ~1.0  $\mu\text{g/mL}$ ) to check the amount-effect for 30 min. As the fluorescence effect plots show, the fluorescence intensity from 0.5  $\mu\text{g/mL}$  ZnO-S was similar to that of 1.0  $\mu\text{g/mL}$  DE-ZnO (Fig. 2.4.2.H). Then, certain amounts of pure ZnO-S (0.5  $\mu\text{g/mL}$ ) and DE-ZnO (1.0  $\mu\text{g/mL}$ ) were applied to the time linear record test of the DCF fluorescence. Obvious fluorescence quenching was detected and the fluorescence quenching of the DE-ZnO composites was slower than that of the pure ZnO (Fig. 2.4.2.I). This phenomenon indicated that the ions and ROS released from the DE-ZnO composites have been through an ‘absorb-release’ course from the porous framework, which has prolonged the active process.

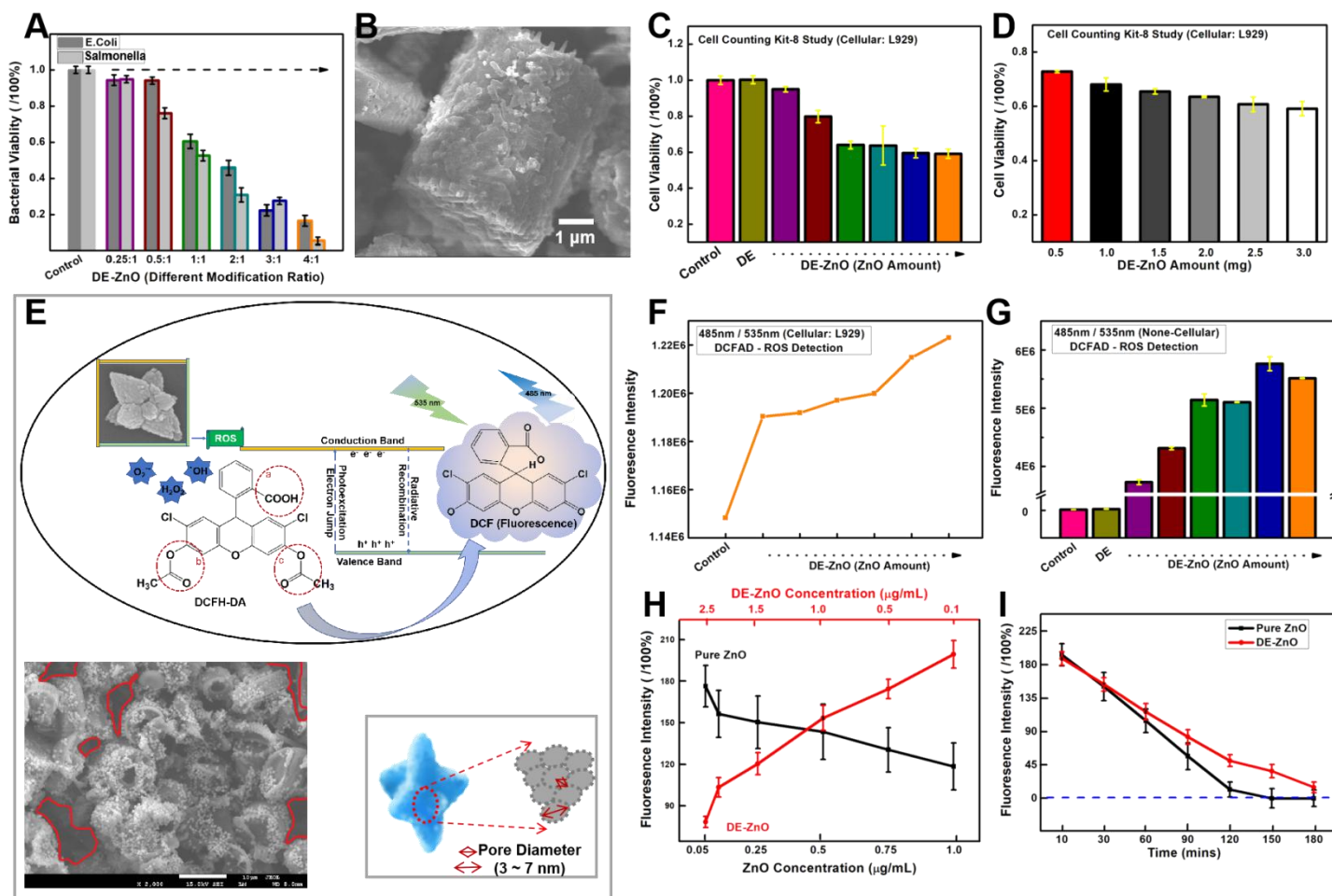


Figure 2.4.2. Antibacterial activity and bio-safety dosage study of bio-inspired DE-ZnO.

**Figure 2.4.2. Antibacterial activity and bio-safety dosage study of bio-inspired DE-ZnO.**

(A) Antibacterial efficiency of DE-No against Gram-negative bacteria (*E. coli*, *S. enterica*) at a concentration of 10  $\mu\text{g/mL}$ . (B) The SEM image showing the surface of DE-ZnO composites after meeting / absorbing pathogen. (C) Cell viability study of the cytotoxicity of DE-ZnO at different modification ratios with dosage of 0.25 mg in one hole through Cell counting Kit 8 method. (D) Dosage depended cytotoxicity study of DE-ZnO. Each data value is mean  $\pm$  SE of three independent experiments. (E) Schematic illustration of the Reactive oxygen species (ROS) detection. (F) Cellular ROS detection assay using DE-ZnO with different ratios of ZnO modification. (G) Non-cellular ROS detection assay using DE-ZnO with different ratios of ZnO modification. (H-I) The mechanisms of the delay ions/ROS ‘quenching’ related antifungal property of DE-ZnO. (H) Non-cellular ROS detection assay using ZnO and DE-ZnO with different concentrations of nanomaterials. (I) Time-dependended study of the effect from ROS protection, explaining the ‘quenching’.

(Abbreviations: DCF, 2',7'-Dichlorofluorescein; DCFH-DA, 2',7'-Dichlorofluorescein diacetate, Error bars indicate the standard error of the mean based on at least three independent experiments).

### 2.(3-4).3 Antifungal study of DE-ZnO

Next, the treatment problem of the fungal infection inspired us to study the antifungal efficacy with the DE-ZnO semiconductor composites. As we previously reported, ZnO induces the generation of reactive oxygen species (ROS:  $O^{2-}$ ,  $\cdot OH$ ,  $H_2O_2$ ) that react with the peptidoglycan layer and break the glycosidic bonds in a biological manner. Here, we tested the DE-ZnO (2:1, 10.61% of ZnO) with different concentration ranges from 0.5 to 4.0 mg/mL on *A. fumigatus* plates (1000 conidia, 25 °C). We monitored the fungal growth condition in 14 d, the diameter of the grown microflora at the 7th Day was measured (Fig.2.4.3.A). Under the culture condition, the fungi were barely growing at 4.0 mg/mL of the DE-ZnO composites. Thus, the DE-ZnO composites were not only inhibit the fungal growing, but also kill the fungal activity due to break the cell wall of fungal.

Furthermore, to investigate the effect of DE-ZnO on antifungal, we added the DE-ZnO composite into the fungal spore solution for 3 min. The DE-ZnO is well absorbed the fungal spores (Fig.2.4.3.B) due to the capture enrichment property of DE-ZnO composite, which is an important advantage for its antifungal property. For more insights into this highly cooperative relationship and synergistic effect of the DE-ZnO, we treated fungi cultures with pure DE, pure ZnO, ‘pure DE+pure ZnO’ and DE-ZnO composites (Fig.2.4.3.C). The radial growth estimations indicate that i). The colony growth when treated with pure ZnO and DE-ZnO composites are well matched with the fluorescence quenching study, with a significant synergy effect of the DE-ZnO composites showing “1+1>2” performance; and ii). The antifungal effect of ‘pure DE+pure ZnO’ is less than the DE-ZnO composites, even less than the same amount of pure ZnO (“1+1<1”), and this phenomenon is consistent with a prior report of N dopants into hierarchically porous composites (Fig.2.4.3.C). Based on the results, we summarized the antifungal property of DE-ZnO composites as a scheme (Fig.2.4.3.D). First, the capture-enrich step between the cell wall of fungal and the activated surface of DE-ZnO composite can be achieved through the surface charge adsorption and van der waals forces. Second, the nano-lysis step of the DE-ZnO can

be achieved to the fungi by breaking the cell membrane. Taken together, the DE-ZnO composites are promising and are good candidates for antifungal and antibacterial treatment.

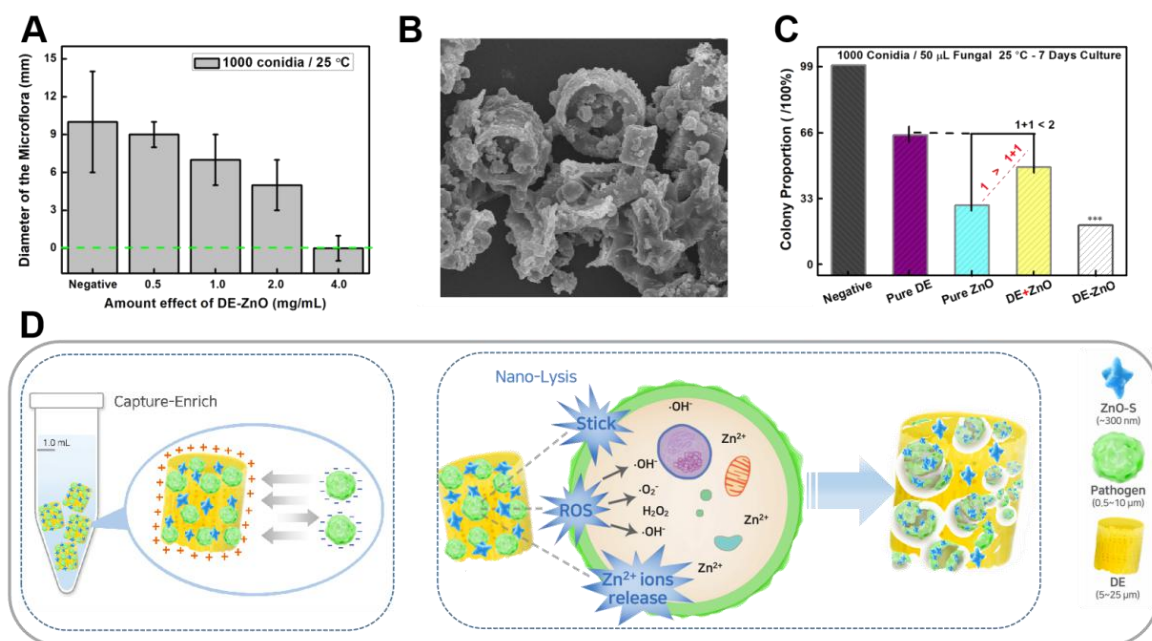


**Figure 2.4.3. Antifungal activity study of bio-inspired DE-ZnO**

(A) Amount effect of DE-ZnO on anti-fungal activity (1000 conidia, 25°C, culture for 3 d). Each data value is mean  $\pm$  SE of duplicate independent experiments with 3 d culture. (B) SEM image of fungal aspergillus absorbed on the DE-ZnO composites. (C) Growth tendency of fungi with a synergy effect between DE+ZnO and pure ZnO showing a “1+1<1” preference. Each data value is mean  $\pm$  SE of duplicate independent experiments. (D) Scheme of the antifungal mechanism of DE-ZnO composite.

## 2.(3-4).4 Synergistic and persistence of DE-ZnO composites

Nowadays, it has become harder for antibiotics to break cell membranes, due to the development of resistance by the cell wall that keeps antibiotics out of fungi and Gram-negative bacteria. Thus studies designed to combat the resistance of fungal, we tested the synergistic effect and persistence of DE-ZnO composites in combination with commercial antibiotics (amphotericin B and itraconazole) for their antifungal activity (Fig.2.4.4). For a more detailed investigation into the synergistic effect between the DE-ZnO composites and the commercial drugs, 2.0 mg/mL DE-ZnO with either 0.5 mg/L amphotericin B or 6.0  $\mu$ g/mL itraconazole were used as the initial concentrations. We showed significant enhancements in both the i) DE-ZnO with itraconazole (Fig.2.4.4.A) and ii) the DE-ZnO with amphotericin B groups (Fig.2.4.4.B). The mechanisms of the antifungal activity by the antibiotics have been previously demonstrated Itraconazole disrupts the conversion of lanosterol to ergosterol, which disrupts the growth process, and amphotericin B actively penetrates the cell membrane.

To gain insight into the antibiotic persistence of the DE-ZnO composites, long term culture of the fungi was investigated. The growth of colonies from the negative control, antibiotic drug treatment only, and DE-ZnO with antibiotic drug groups was evaluated and the growth rates on Day 7 ( $a_1 \sim c_1$ ) and 15 ( $a_2 \sim c_2$ ) have been recorded (Fig. .2.4.4.C). According to the slopes of the groups for the growth rate, “ $a_1 > b_1 > c_1$ ” demonstrated that the DE-ZnO composites enhanced the antifungal performance of those antibiotics. “ $a_2 > a_1 ; b_2 > b_1$ ” indicated that the fungi were growing faster after 7 d of culture in both the negative and antibiotic treatment only groups. However, the DE-ZnO composites combined with the antibiotic exhibited a striking long-enduring inhibition, with “ $c_2 < c_1$ ”, which suggests a strong synergistic effect.

Thereby, the antibiotic efficacy and synergy effect of DE-ZnO composites with the commercial drugs (Fig. 4d) showing that the long-term effect as an antifungal is due to the delayed release of ions and ROS reactions. Therefore, we concluded that the synergistic effect and persistence of DE-ZnO composites could be used as a



promising antifungal agent to solve the inconvenience caused by the requirement for multiple doses of insoluble antibiotics. To a certain extent, the nano-therapy open a way for antibiotic treatment to be reduced the of usage of antibiotic and decelerated the fungal mutations.

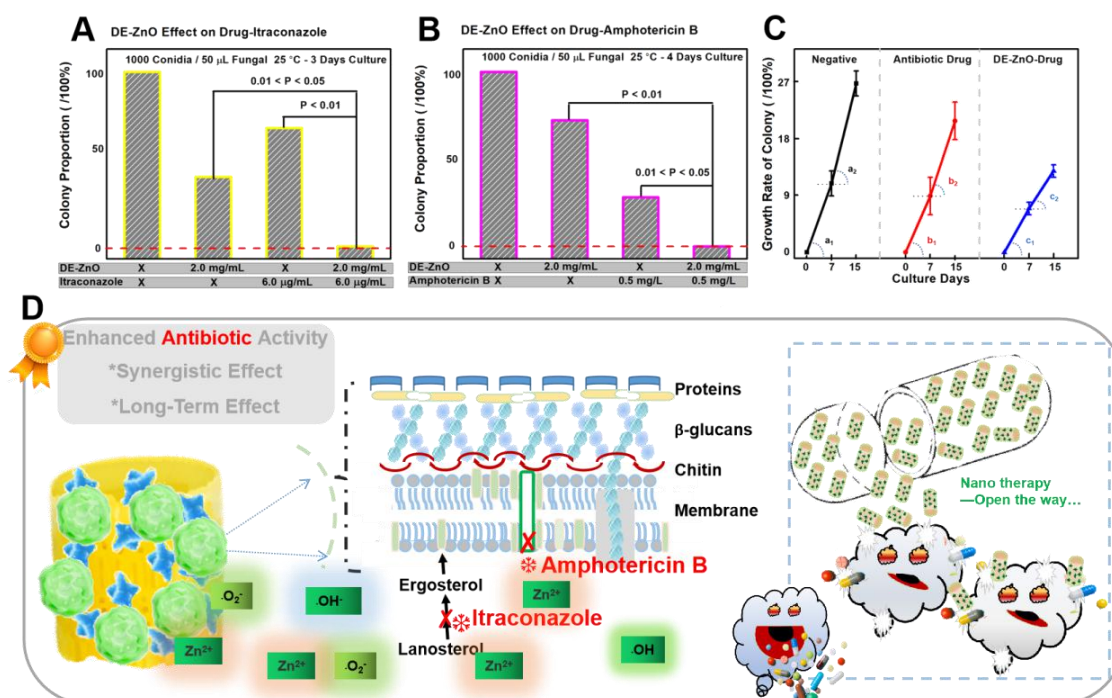


**Figure 2.4.4. Synergistic effect and persistence of bio-inspired DE-ZnO composites against fungal infection**

(A) Antifungal activity of the DE-ZnO composite, itraconazole, and combination groups up to 3 d of culture with 1000 conidia. (B) Antifungal activity of the DE-ZnO composite, amphotericin B, and combination groups up to 4 d of culture with 1000 spores. Each data value is mean  $\pm$  SE of duplicate independent experiments. (C) Long term (15 d) culture of the fungi; growth rate of the colony reflects the enhanced synergy effect of the DE-ZnO composites; growth tendency of the synergy effect between the DE-ZnO composites and commercial drugs (*Amphotericin B* and *Itraconazole*). (D) Scheme of synergistic effect from a combination of DE-ZnO and the existing drugs as a nano therapy way.

## **2.(3-4).5 Biocompatibility and toxicity DE-ZnO composites in vivo**

We next evaluated the *in vivo* toxicity of the DE-ZnO composites. After DE-ZnO administration, all animals were observed daily for clinical signs of toxicity, including tremors, convulsions, salivation, nausea, vomiting, diarrhea and body weight changes, and death, during the 14 d (Fig.2.4.5). There were no deaths at both dosages. There were no significant alterations of weight or any toxicity symptoms in both the low dosage (LD)-DE-ZnO and high dosage (HD)-DE-ZnO groups. Meanwhile, when we compared with same dosage of the nanomaterials, the toxicity of DE-ZnO (2:1) is 6 times lower using oral medication and the dosage amount of DE-ZnO is 3 times higher than the SiO<sub>2</sub>-ZnO. And the animals were sacrificed after 14 d, and their major organs including brain, heart, lung, liver, kidneys, spleen, testis or uterus were collected and weighed for males and females (Fig.2.4.5.A). There were no differences among the DE-ZnO and control groups. Meanwhile, examination of the organs as shown in Figure 5D showed that there were no abnormalities in any of the tested groups. Moreover, we did not observe any histopathological changes or damage in the liver of DE-ZnO treated mice (Fig.2.4.5.B-C). Furthermore, the results of the biochemical analysis conducted 14 d after the administration of the DE-ZnO are shown in Fig.2.4.5.D. There were no differences in the biochemical parameters of the DE-ZnO groups compared to the control group. These results revealed that there were no signs of toxicity in the mice treated with low or high doses of DE-ZnO by oral administration *in vivo*. These findings suggest the DE-ZnO composites are relatively safe for biomedical applications.

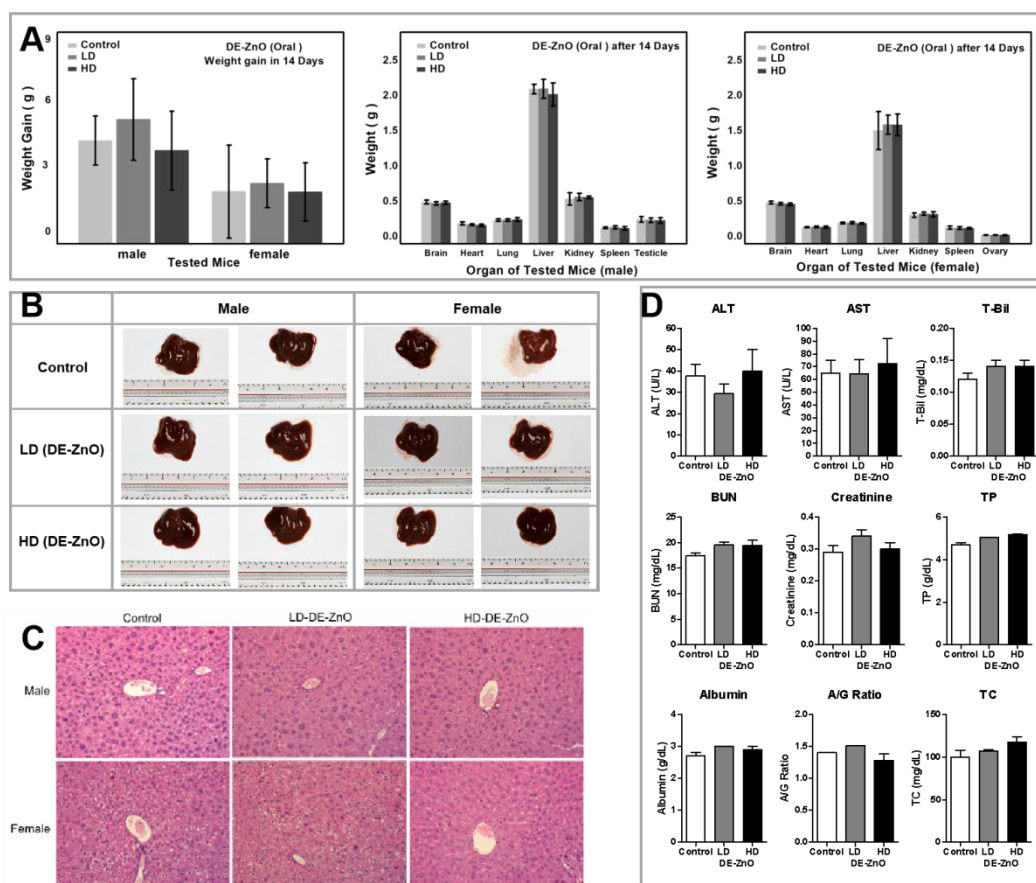


**Figure 2.4.5. The biocompatibility and toxicity of the bio-inspired DE-ZnO composites *in vivo***

(A) Body weight and major organs weight changes of the mice treated with LD-DE-ZnO or HD-DE-ZnO composites by oral administration, monitored for 14 d. male and female mice after 14 d of oral administration with DE-ZnO composites. (B) Liver morphology changes in the mice after 14 d of oral administration with DE-ZnO. (C) Biochemical parameters changes in mice treated with LD-DE-ZnO or HD-DE-ZnO composites by oral administration. c Histology analysis of liver tissue of mice treated with LD-DE-ZnO or HD-DE-ZnO composites by oral administration. (D) The sections were stained with hematoxylin and eosin (Magnification  $\times 200$ ). Histologic changes showed no differences among groups ( $n = 4$  mice per group). Each data value is mean  $\pm$  SE. ( $n = 4$  mice per group). Abbreviations: ALT, alanine aminotransferase; AST, aspartate aminotransferase; T-Bil, total bilirubin; BUN, blood urea nitrogen; TP, total protein; A/G, albumin/globulin; TC, total cholesterol; LD, low dosage; HD, high dosage.

## 2.4.4 CONCLUSION

In this study, we synthesized the facile natural semiconductor composites (DE-ZnO) and demonstrated the antibiotic efficacy and persistence of DE-ZnO against fungi and Gram-negative bacteria (perspective in nano-therapy, Fig.2.4.6). To the best of our knowledge, we are the first to synthesize a novel composite conjugated ZnO on the porous surface of DE for an optimal antibiotic effect with non-toxicity (Table 1). Based on our study of its morphological changes, we observed that the DE-ZnO composites strongly bound to the pathogen's membrane and disrupted its membrane morphology. Generally, disruption of the fungal cell wall is more difficult than for other pathogens, which subsequently leads to low antibiotic effects. Using multiple experiments, we demonstrated several possible mechanisms whereby DE-ZnO enhances antibiotic activity and persistence against fungi (*A. fumigatus*) and Gram-negative bacteria (*E. coli* and *S. enterica*): i) Increasing physical attraction. The surface charge of the composites is positive due to the combination of two physical functionalities by the sharp shape of the synthesized ZnO and the porous structured DE for enhancement of physical disruption and physical absorption, respectively. ii) Increased ROS production and long persistence. The DE-ZnO composites lead to increased ROS production, and the effect can enhance antibiotic activity at the cellular and non-cellular level for longer periods than other ZnO materials. iii) Excessive zinc ions ( $\text{Zn}^{2+}$ ).  $\text{Zn}^{2+}$  can directly rupture the cell wall when the composites bind to pathogens. Additionally, we evaluated the toxicity of DE-ZnO after oral administration to mice. While further studies are desirable to fully establish the safety of DE-ZnO in mice and humans, we observed the composite was safe at experimental dosages when administered to mice for two weeks. Their organs had normal weights and their blood chemistry was normal as compared to the controls. Next, we systemically investigated the synergistic effect between the DE-ZnO composites and existing antifungal agents (amphotericin B and itraconazole) using *A. fumigatus*. These antifungal agents have many limitations such as high toxicity, insolubility, sensitivity to pH, and severe side effects for patients with cancers and

transplants. The antifungal efficacy of DE-ZnO combined with either of these antifungal agents was significantly enhanced compared to that of the single treatment. Even though the existing antifungal agents are toxic to the organs in the mouse, a reduced dose of the existing antifungal agent made possible by the addition of DE-ZnO can reduce their toxicity and enhance their antifungal activity. Although further study is required to verify the ability of DE-ZnO to kill pathogens in infected mice and humans over the long-term, this synergistic therapy describing the potential of DE-ZnO to enhance antifungal activity alone or in combination therapy with lower doses of existing drugs has great clinical potential.

Our results have shown that this non-toxic DE-ZnO composite can be used as an antibiotic agent against fungi and Gram-negative bacteria in a clinical setting. Moreover, the DE-ZnO composites have a porous structure, which can be efficiently loaded with another antibiotic agent, so they can also be used as carriers for drug delivery. Hence, given recent advances in the surface chemistry of nanomaterials, future study will focus on drug delivery systems containing DE-ZnO composites to develop efficient therapies against target sites in various clinical applications. Therefore, we envision that DE-ZnO composites can be used to enhance the mode of action of antibiotics against fungi and bacteria, and thus will be useful as novel antibiotic agents for fighting antimicrobial infections.

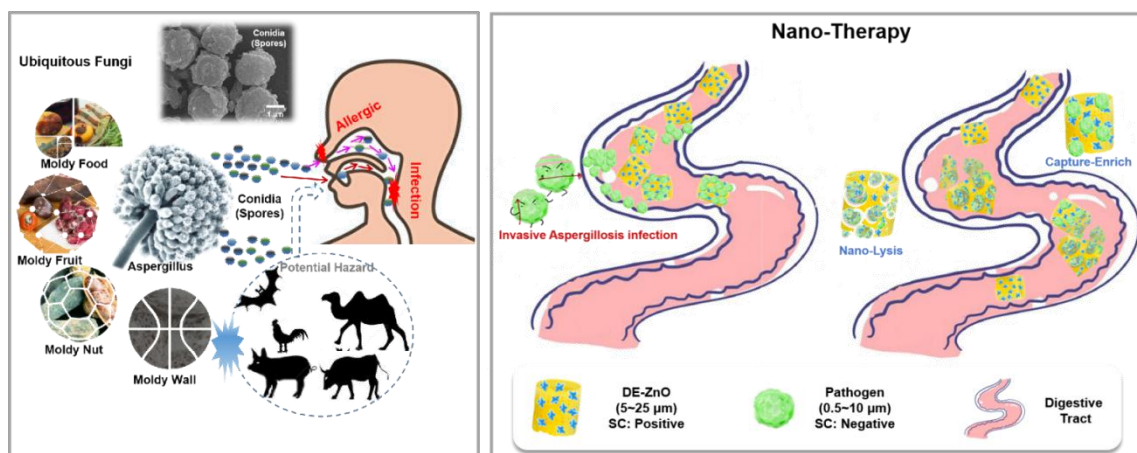


**Figure 6 Perspectives of this DE-ZnO composite in the industry applications.**

## SUMMARY

In section one, we studied the binary nanomaterials (semiconductor ZnO and natural diatomaceous earth) for ultrasensitive nucleic acids isolation and detection which have overcome the sample preparation and detection limitations of conventional point-of-care testing (POCT) systems. These studies provides new insight into amino functionalization and biomolecular (HI and CB) modification in bioapplications. Meanwhile these studies also lay a foundation for further development of sample preparation techniques for human disease diagnostics and molecular encapsulation in drug delivery systems.

In section two, the medical applications of nanocomposites have been studied. Base on the biocompatibility study of the magnetic  $\text{Fe}_3\text{O}_4$ , ZnO and natural diatomaceous earth (DE) with amino functionalization and biomolecular (HI and CB) modification in vitro and in vivo, we tested the absorbance and encapsulation properties of several types composites with dyes, pathogens and drugs. Hence, given recent advances in the surface chemistry of nanomaterials, future study will focus on drug delivery systems containing to develop efficient therapies against target sites in various clinical applications. Therefore, we envision the nanomaterials can be used to enhance the mode of action of antibiotics against fungi and bacteria, and thus will be useful as novel antibiotic agents for fighting antimicrobial infections.

All in all, as the promising area of research, nanotechnology with potential benefits in patients suffering various illnesses. Although nanomaterials are extensively studied for drug delivery and are proving to be effective in drug delivery and the diagnostic field, at least in animal models, further research is needed to prove these benefits in humans which also encourage us to devote more study into it.

## REFERENCE

1. Shin, Y., Lim, S.Y., Lee, T.Y. & Park, M.K. Dimethyl adipimide/Thin film Sample processing (DTS); A simple, low-cost, and versatile nucleic acid extraction assay for downstream analysis. *Scientific reports* **5**, 14127 (2015).
2. Zhao, Y., Chen, F., Li, Q., Wang, L. & Fan, C. Isothermal amplification of nucleic acids. *Chem. Rev* **115**, 12491-12545 (2015).
3. Kim, J., Johnson, M., Hill, P. & Gale, B.K. Microfluidic sample preparation: cell lysis and nucleic acid purification. *Integrative Biology* **1**, 574-586 (2009).
4. Du, Y. & Dong, S. Nucleic Acid Biosensors: Recent Advances and Perspectives. *Anal. Chem* **89**, 189-215 (2017).
5. Jung, M., Uhl, B., Kristiansen, G. & Dietrich, D. Bisulfite conversion of DNA from tissues, cell lines, buffy coat, FFPE tissues, microdissected cells, swabs, sputum, aspirates, lavages, effusions, plasma, serum, and urine. *Population Epigenetics: Methods and Protocols*, 139-159 (2017).
6. Liang, Y. et al. Adhesive hemostatic conducting injectable composite hydrogels with sustained drug release and photothermal antibacterial activity to promote full-thickness skin regeneration during wound healing. *Small* **15**, 1900046 (2019).
7. Porebski, S., Bailey, L.G. & Baum, B.R. Modification of a CTAB DNA extraction protocol for plants containing high polysaccharide and polyphenol components. *Plant molecular biology reporter* **15**, 8-15 (1997).
8. Wu, J., Kodzius, R., Cao, W. & Wen, W. Extraction, amplification and detection of DNA in microfluidic chip-based assays. *Microchimica Acta* **181**, 1611-1631 (2014).
9. Al-Jeboory, M.R., Al-Jailawi, M.H., Al-Obaedi, A.M. & Al-Jeboory, S.R. in Int'l Conf. on Medical Genetics, Cellular & Molecular Biology, Pharmaceutical & Food Sciences (GCMBPF-2015) (2015).
10. Shin, Y., Perera, A.P., Wong, C.C. & Park, M.K. Solid phase nucleic acid extraction technique in a microfluidic chip using a novel non-chaotropic agent: dimethyl adipimide. *Lab on a Chip* **14**, 359-368 (2014).
11. Zhao, F., Lee, E.Y. & Shin, Y. Improved Reversible Cross-linking-based Solid-phase RNA Extraction for Pathogen Diagnostics. *Analytical chemistry* (2018).
12. Kim, J. & Gale, B.K. Quantitative and qualitative analysis of a microfluidic DNA extraction system using a nanoporous AlO<sub>x</sub> membrane. *Lab on a Chip* **8**, 1516-1523 (2008).
13. Liu, H. et al. Large instrument-and detergent-free assay for ultrasensitive nucleic acids isolation via binary nanomaterial. *Analytical chemistry* **90**, 5108-5115 (2018).
14. So, H., Lee, K., Murthy, N. & Pisano, A.P. All-in-one nanowire-decorated multifunctional membrane for rapid cell lysis and direct DNA isolation. *ACS applied materials & interfaces* **6**, 20693-20699 (2014).
15. Bylda, C., Thiele, R., Kobold, U. & Volmer, D.A. Recent advances in sample

- preparation techniques to overcome difficulties encountered during quantitative analysis of small molecules from biofluids using LC-MS/MS. *Analyst* **139**, 2265-2276 (2014).
16. He, M., Crow, J., Roth, M., Zeng, Y. & Godwin, A.K. Integrated immunoisolation and protein analysis of circulating exosomes using microfluidic technology. *Lab on a Chip* **14**, 3773-3780 (2014).
  17. Tsougeni, K. et al. Plasma nanotextured polymeric lab-on-a-chip for highly efficient bacteria capture and lysis. *Lab on a Chip* **16**, 120-131 (2016).
  18. Kashyap, A., Autebert, J., Delamarche, E. & Kaigala, G.V. Selective local lysis and sampling of live cells for nucleic acid analysis using a microfluidic probe. *Scientific reports* **6**, 29579 (2016).
  19. Buser, J.R. et al. A disposable chemical heater and dry enzyme preparation for lysis and extraction of DNA and RNA from microorganisms. *Analytical Methods* **8**, 2880-2886 (2016).
  20. Kim, J., Hong, J.W., Kim, D.P., Shin, J.H. & Park, I. Nanowire-integrated microfluidic devices for facile and reagent-free mechanical cell lysis. *Lab on a Chip* **12**, 2914-2921 (2012).
  21. Zhao, F., Koo, B., Liu, H., Jin, C.E. & Shin, Y. A single-tube approach for in vitro diagnostics using diatomaceous earth and optical sensor. *Biosensors and Bioelectronics* (2017).
  22. Lawn, S.D. et al. Advances in tuberculosis diagnostics: the Xpert MTB/RIF assay and future prospects for a point-of-care test. *The Lancet infectious diseases* **13**, 349-361 (2013).
  23. Panigrahi, A.K., Singh, V. & Singh, S.G. A multi-walled carbon nanotube–zinc oxide nanofiber based flexible chemiresistive biosensor for malaria biomarker detection. *Analyst* **142**, 2128-2135 (2017).
  24. Jang, Y.O. et al. A homobifunctional imidoester-based microfluidic system for simultaneous DNA and protein isolation from solid or liquid biopsy samples. *Lab on a Chip* **19**, 2256-2264 (2019).
  25. Holzinger, M., Le Goff, A. & Cosnier, S. Nanomaterials for biosensing applications: a review. *Frontiers in chemistry* **2**, 63-63 (2014).
  26. Wei, W., Rosenkrans, Z.T., Luo, Q.Y., Lan, X. & Cai, W. Exploiting Nanomaterial-Mediated Autophagy for Cancer Therapy. *Small methods* **3**, 1800365 (2019).
  27. Jahangirian, H., Lemraski, E.G., Webster, T.J., Rafiee-Moghaddam, R. & Abdollahi, Y. A review of drug delivery systems based on nanotechnology and green chemistry: green nanomedicine. *International journal of nanomedicine* **12**, 2957 (2017).
  28. Zhang, S.-L. et al. Study of the size effect on the optical mode frequencies of ZnO nanoparticles with nearly uniform size. *Applied physics letters* **89**, 243108 (2006).
  29. Al-Gaashani, R., Radiman, S., Daud, A., Tabet, N. & Al-Douri, Y. XPS and optical studies of different morphologies of ZnO nanostructures prepared by microwave methods. *Ceramics International* **39**, 2283-2292 (2013).



30. Xu, P. et al. Use of iron oxide nanomaterials in wastewater treatment: a review. *Science of the Total Environment* **424**, 1-10 (2012).
31. Liu, H., Zhong, L., Yun, K. & Samal, M. Synthesis, characterization, and antibacterial properties of silver nanoparticles-graphene and graphene oxide composites. *Biotechnology and bioprocess engineering* **21**, 1-18 (2016).
32. Lee, D.W., Yoo, B.R.J.J.o.I. & Chemistry, E. Advanced silica/polymer composites: Materials and applications. **38**, 1-12 (2016).
33. Fu, Y.Q. et al. Recent developments on ZnO films for acoustic wave based bio-sensing and microfluidic applications: a review. *Sensors and Actuators B: Chemical* **143**, 606-619 (2010).
34. Ma, H., Williams, P.L. & Diamond, S.A. Ecotoxicity of manufactured ZnO nanoparticles—a review. *Environmental Pollution* **172**, 76-85 (2013).
35. Kim, I. et al. ZnO Nanostructures in Active Antibacterial Food Packaging: Preparation Methods, Antimicrobial Mechanisms, Safety Issues, Future Prospects, and Challenges. *Food Reviews International*, 1-29 (2020).
36. Al-Tayyar, N.A., Youssef, A.M. & Al-Hindi, R.R. Antimicrobial packaging efficiency of ZnO-SiO<sub>2</sub> nanocomposites infused into PVA/CS film for enhancing the shelf life of food products. *Food Packaging and Shelf Life* **25**, 100523 (2020).
37. Ramachandrappa, L.T. et al. Biofabrication of zinc oxide nanoparticles with Syzygium aromaticum flower buds extract and finding its novel application in controlling the growth and mycotoxins of Fusarium graminearum. *Frontiers in microbiology* **10**, 1244 (2019).
38. Applerot, G. et al. Enhanced antibacterial activity of nanocrystalline ZnO due to increased ROS-mediated cell injury. *Advanced Functional Materials* **19**, 842-852 (2009).
39. Bhat, S.S., Qurashi, A. & Khanday, F.A. ZnO nanostructures based biosensors for cancer and infectious disease applications: Perspectives, prospects and promises. *TrAC Trends in Analytical Chemistry* **86**, 1-13 (2017).
40. Mansor, N.A. et al. Detection of Breast Cancer 1 (BRCA1) Gene Using an Electrochemical DNA Biosensor Based on Immobilized ZnO Nanowires. *Open Journal of Applied Biosensor* **3**, 9 (2014).
41. Umar, A. et al. Applications of ZnO nanoflowers as antimicrobial agents for escherichia coli and enzyme-free glucose sensor. *Journal of biomedical nanotechnology* **9**, 1794-1802 (2013).
42. Dutta, R., Nenavathu, B.P., Gangishetty, M.K. & Reddy, A. Studies on antibacterial activity of ZnO nanoparticles by ROS induced lipid peroxidation. *Colloids and Surfaces B: Biointerfaces* **94**, 143-150 (2012).
43. Khan, M.F. et al. Flower-shaped ZnO nanoparticles synthesized by a novel approach at near-room temperatures with antibacterial and antifungal properties. *International journal of nanomedicine* **9**, 853 (2014).
44. Han, C., Yang, M.-Q., Weng, B. & Xu, Y.-J. Improving the photocatalytic activity and anti-photocorrosion of semiconductor ZnO by coupling with versatile carbon. *Physical Chemistry Chemical Physics* **16**, 16891-16903

- (2014).
45. Münchow, E.A. et al. Development and characterization of novel ZnO-loaded electrospun membranes for periodontal regeneration. *Dental Materials* **31**, 1038-1051 (2015).
  46. Ümit, Ö., Hofstetter, D. & Morkoc, H. ZnO devices and applications: a review of current status and future prospects. *Proceedings of the IEEE* **98**, 1255-1268 (2010).
  47. Hamm, C.E., Merkel, R., Springer, O. & Jurkojc, P. Architecture and material properties of diatom shells provide effective mechanical protection. *Nature* **421**, 841 (2003).
  48. Henderson, R.K., Baker, A., Parsons, S.A. & Jefferson, B. Characterisation of algogenic organic matter extracted from cyanobacteria, green algae and diatoms. *Water research* **42**, 3435-3445 (2008).
  49. Losic, D. et al. Surface functionalisation of diatoms with dopamine modified iron-oxide nanoparticles: toward magnetically guided drug microcarriers with biologically derived morphologies. *Chemical Communications* **46**, 6323-6325 (2010).
  50. Gärdes, A., Iversen, M.H., Grossart, H.-P., Passow, U. & Ullrich, M.S. Diatom-associated bacteria are required for aggregation of *Thalassiosira weissflogii*. *The ISME journal* **5**, 436 (2011).
  51. Zhang, H. et al. Diatom silica microparticles for sustained release and permeation enhancement following oral delivery of prednisone and mesalamine. **34**, 9210-9219 (2013).
  52. Rea, I. et al. Diatomite biosilica nanocarriers for siRNA transport inside cancer cells. *Biochimica et Biophysica Acta (BBA)-General Subjects* **1840**, 3393-3403 (2014).
  53. Ruggiero, I. et al. Diatomite silica nanoparticles for drug delivery. *Nanoscale research letters* **9**, 329 (2014).
  54. Viji, S. et al. Diatom-based label-free optical biosensor for biomolecules. *Applied biochemistry and biotechnology* **174**, 1166-1173 (2014).
  55. Shi, J., Kantoff, P.W., Wooster, R. & Farokhzad, O.C. Cancer nanomedicine: progress, challenges and opportunities. *Nature Reviews Cancer* (2016).
  56. Soenen, S.J., Parak, W.J., Rejman, J. & Manshian, B. (Intra) cellular stability of inorganic nanoparticles: effects on cytotoxicity, particle functionality, and biomedical applications. *Chemical reviews* **115**, 2109-2135 (2015).
  57. Terracciano, M. et al. in *Algae-Organisms for Imminent Biotechnology* (InTech, 2016).
  58. Liu, D. et al. Metal-Organic Frameworks Reactivate Deceased Diatoms to be Efficient CO<sub>2</sub> Absorbents. *Advanced Materials* **26**, 1229-1234 (2014).
  59. Cicco, S.R. et al. Biosilica from Living Diatoms: Investigations on Biocompatibility of Bare and Chemically Modified *Thalassiosira weissflogii* Silica Shells. *Bioengineering* **3**, 35 (2016).
  60. Jang, L.-S. & Liu, H.-J. Fabrication of protein chips based on 3-aminopropyltriethoxysilane as a monolayer. *Biomedical microdevices* **11**,

- 331-338 (2009).
61. Jiang, J., Pi, J. & Cai, J. The advancing of zinc oxide nanoparticles for biomedical applications. *Bioinorganic chemistry and applications* **2018** (2018).
  62. Tanaka, M., Harlisa, I.H., Takahashi, Y., Ikhsan, N.A. & Okochi, M. Screening of bacteria-binding peptides and one-pot ZnO surface modification for bacterial cell entrapment. *RSC advances* **8**, 8795-8799 (2018).
  63. Morris, A.S. et al. Amine modification of nonporous silica nanoparticles reduces inflammatory response following intratracheal instillation in murine lungs. *Toxicology letters* **241**, 207-215 (2016).
  64. Heo, S.W. et al. Host–guest chemistry in the gas phase: selected fragmentations of CB [6]–peptide complexes at lysine residues and its utility to probe the structures of small proteins. *Analytical chemistry* **83**, 7916-7923 (2011).
  65. An, J. et al. Purification of protein therapeutics via high-affinity supramolecular host–guest interactions. *Nature Biomedical Engineering* (2020).
  66. Karcher, S., Kornmüller, A. & Jekel, M. Cucurbituril for water treatment. Part I:: Solubility of cucurbituril and sorption of reactive dyes. *Water research* **35**, 3309-3316 (2001).
  67. Lagona, J., Mukhopadhyay, P., Chakrabarti, S. & Isaacs, L. The cucurbit [n] uril family. *Angewandte Chemie International Edition* **44**, 4844-4870 (2005).
  68. Rekharsky, M.V. et al. Chiral recognition in cucurbituril cavities. *Journal of the American Chemical Society* **128**, 14871-14880 (2006).
  69. Kim, K. et al. Functionalized cucurbiturils and their applications. *Chemical Society Reviews* **36**, 267-279 (2007).
  70. Lee, J.W., Samal, S., Selvapalam, N., Kim, H.-J. & Kim, K. Cucurbituril homologues and derivatives: new opportunities in supramolecular chemistry. *Accounts of chemical research* **36**, 621-630 (2003).
  71. Salleh, M.A.M., Mahmoud, D.K., Karim, W.A.W.A. & Idris, A.J.D. Cationic and anionic dye adsorption by agricultural solid wastes: A comprehensive review. **280**, 1-13 (2011).
  72. Liu, H. et al. A Sample Preparation Technique Using Biocompatible Composites for Biomedical Applications. *Molecules* **24**, 1321 (2019).
  73. Khezri, K. Polystyrene–mesoporous diatomite composites produced by in situ activators regenerated by electron transfer atom transfer radical polymerization. *RSC Advances* **6**, 109286-109295 (2016).
  74. Liu, H. et al. Cucurbituril-based Reusable Nanocomposites for Efficient Molecular Encapsulation. *ACS Sustainable Chemistry & Engineering* (2019).
  75. Dharmalingam, K., Bordoloi, D., Kunnumakkara, A.B. & Anandalakshmi, R. Formation and characterization of zinc oxide complexes in composite hydrogel films for potential wound healing applications. *Polymer Composites* (2020).
  76. Patterson, T.F. et al. Practice guidelines for the diagnosis and management of

- aspergillosis: 2016 update by the Infectious Diseases Society of America. *Clinical Infectious Diseases* **63**, e1-e60 (2016).
77. Zhao, X.B. & Lee, R.J. Tumor-selective targeted delivery of genes and antisense oligodeoxyribonucleotides via the folate receptor. *Advanced drug delivery reviews* **56**, 1193-1204 (2004).
  78. Tasciotti, E. et al. Mesoporous silicon particles as a multistage delivery system for imaging and therapeutic applications. *Nature nanotechnology* **3**, 151 (2008).
  79. Lim, Y.-b. et al. Self-assembled ternary complex of cationic dendrimer, cucurbituril, and DNA: noncovalent strategy in developing a gene delivery carrier. *Bioconjugate chemistry* **13**, 1181-1185 (2002).
  80. Kwon, E.J. et al. Porous Silicon Nanoparticle Delivery of Tandem Peptide Anti-Infectives for the Treatment of Pseudomonas aeruginosa Lung Infections. *Advanced materials* **29**, 1701527 (2017).
  81. Zhang, Y. et al. A bioadhesive nanoparticle–hydrogel hybrid system for localized antimicrobial drug delivery. *ACS applied materials & interfaces* **8**, 18367-18374 (2016).
  82. Wang, Y., Yang, Y., Shi, Y., Song, H. & Yu, C. Antibiotic-Free Antibacterial Strategies Enabled by Nanomaterials: Progress and Perspectives. *Advanced Materials*, 1904106 (2019).
  83. Xiong, Z.-C. et al. Ultralong hydroxyapatite nanowires-based paper co-loaded with silver nanoparticles and antibiotic for long-term antibacterial benefit. *ACS applied materials & interfaces* **9**, 22212-22222 (2017).
  84. Bai, H. et al. A supramolecular antibiotic switch for antibacterial regulation. *Angewandte Chemie International Edition* **54**, 13208-13213 (2015).
  85. Quan, K. et al. Artificial channels in an infectious biofilm created by magnetic nanoparticles enhanced bacterial killing by antibiotics. *Small* **15**, 1902313 (2019).
  86. Yang, X., Zhang, L. & Jiang, X. Aminosaccharide–gold nanoparticle assemblies as narrow-spectrum antibiotics against methicillin-resistant Staphylococcus aureus. *Nano Research* **11**, 6237-6243 (2018).
  87. Dar, M.A., Ingle, A. & Rai, M. Enhanced antimicrobial activity of silver nanoparticles synthesized by Cryphonectria sp. evaluated singly and in combination with antibiotics. *Nanomedicine: Nanotechnology, Biology and Medicine* **9**, 105-110 (2013).
  88. Fayaz, A.M. et al. Biogenic synthesis of silver nanoparticles and their synergistic effect with antibiotics: a study against gram-positive and gram-negative bacteria. *Nanomedicine: Nanotechnology, Biology and Medicine* **6**, 103-109 (2010).
  89. Patterson, K. & Streck, M.E. Allergic bronchopulmonary aspergillosis. *Proceedings of the American Thoracic Society* **7**, 237-244 (2010).
  90. Pavani, K., Kumar, N.S. & Sangameswaran, B. Synthesis of lead nanoparticles by Aspergillus species. *Polish Journal of Microbiology* **61**, 61-63 (2012).
  91. El-Nahhal, I.M., Salem, J., Anbar, R., Kodeh, F.S. & Elmanama, A.

- Preparation and antimicrobial activity of ZnO-NPs coated cotton/starch and their functionalized ZnO-Ag/cotton and Zn (II) curcumin/cotton materials. *Scientific Reports* **10**, 1-10 (2020).
92. Nami, S., Aghebati-Maleki, A., Morovati, H. & Aghebati-Maleki, L. Current antifungal drugs and immunotherapeutic approaches as promising strategies to treatment of fungal diseases. *Biomedicine & Pharmacotherapy* **110**, 857-868 (2019).
  93. Howard, K.C., Dennis, E.K., Watt, D.S. & Garneau-Tsodikova, S. A comprehensive overview of the medicinal chemistry of antifungal drugs: perspectives and promise. *Chemical Society Reviews* **49**, 2426-2480 (2020).
  94. Shi, X. et al. Efficient production of antifungal proteins in plants using a new transient expression vector derived from tobacco mosaic virus. *Plant biotechnology journal* **17**, 1069-1080 (2019).
  95. Zhao, Y., Prideaux, B., Baistrocchi, S., Sheppard, D.C. & Perlin, D.S. Beyond tissue concentrations: antifungal penetration at the site of infection. *Medical mycology* **57**, S161-S167 (2019).
  96. Mora-Duarte, J. et al. Comparison of caspofungin and amphotericin B for invasive candidiasis. *New England Journal of Medicine* **347**, 2020-2029 (2002).
  97. Deray, G. Amphotericin B nephrotoxicity. *Journal of antimicrobial chemotherapy* **49**, 37-41 (2002).
  98. Cornely, O.A. et al. Posaconazole vs. fluconazole or itraconazole prophylaxis in patients with neutropenia. *New England Journal of Medicine* **356**, 348-359 (2007).
  99. Zhang, L. et al. Improving Drug Delivery of Micellar Paclitaxel against Non-Small Cell Lung Cancer by Co-loading Itraconazole as a Micelle Stabilizer and a Tumor Vascular Manipulator. *Small* **14**, 1802112 (2018).
  100. Kim, J. et al. Itraconazole, a commonly used antifungal that inhibits Hedgehog pathway activity and cancer growth. *Cancer cell* **17**, 388-399 (2010).
  101. Zhong, L. & Yun, K. Graphene oxide-modified ZnO particles: synthesis, characterization, and antibacterial properties. *International journal of nanomedicine* **10**, 79 (2015).
  102. Pati, R. et al. Topical application of zinc oxide nanoparticles reduces bacterial skin infection in mice and exhibits antibacterial activity by inducing oxidative stress response and cell membrane disintegration in macrophages. *Nanomedicine: Nanotechnology, Biology and Medicine* **10**, 1195-1208 (2014).
  103. Da Silva, E., Kembouche, Y., Tegner, U., Baun, A. & Jensen, K.A. Interaction of biologically relevant proteins with ZnO nanomaterials: A confounding factor for in vitro toxicity endpoints. *Toxicology in Vitro* **56**, 41-51 (2019).
  104. Leung, Y.H. et al. Toxicity of ZnO and TiO<sub>2</sub> to Escherichia coli cells. *Scientific reports* **6** (2016).
  105. Senapati, V.A., Kumar, A., Gupta, G.S., Pandey, A.K. & Dhawan, A. ZnO nanoparticles induced inflammatory response and genotoxicity in human blood cells: A mechanistic approach. *Food and Chemical Toxicology* **85**, 61-70

- (2015).
106. Sirelkhatim, A. et al. Review on zinc oxide nanoparticles: antibacterial activity and toxicity mechanism. *Nano-Micro Letters* **7**, 219-242 (2015).
  107. Adekogbe, I. & Ghanem, A. Fabrication and characterization of DTBP-crosslinked chitosan scaffolds for skin tissue engineering. *Biomaterials* **26**, 7241-7250 (2005).
  108. Tholudur, A. et al. Comparing automated and manual cell counts for cell culture applications. *Bioprocess Int* **4**, 28-34 (2006).
  109. Ragni, R., Cicco, S.R., Vona, D. & Farinola, G.M. Multiple Routes to Smart Nanostructured Materials from Diatom Microalgae: A Chemical Perspective. *Advanced Materials* (2017).
  110. Márquez, C., Hudgins, R.R. & Nau, W.M. Mechanism of host– guest complexation by cucurbituril. *Journal of the American Chemical Society* **126**, 5806-5816 (2004).
  111. Li, X. et al. Adsorption of reactive yellow X-RG and reactive brilliant red X-3B onto cucurbit [8] uril and cucurbit [6] uril: Effect factors, adsorption behavior and mechanism study. **498**, 31-46 (2017).
  112. Barrow, S.J., Kasera, S., Rowland, M.J., del Barrio, J. & Scherman, O.A.J.C.r. Cucurbituril-based molecular recognition. **115**, 12320-12406 (2015).
  113. Huang, Z. et al. Polypseudorotaxane constructed from cationic polymer with cucurbit [7] uril for controlled antibacterial activity. *ACS Macro Letters* **5**, 1109-1113 (2016).
  114. Shao, L. et al. Facile fabrication of magnetic cucurbit [6] uril/graphene oxide composite and application for uranium removal. *Chemical Engineering Journal* **286**, 311-319 (2016).
  115. Lee, S.J.C. et al. Host–guest chemistry from solution to the gas phase: an essential role of direct interaction with water for high-affinity binding of cucurbit [n] urils. *The Journal of Physical Chemistry B* **117**, 8855-8864 (2013).
  116. Barooah, N., Kunwar, A., Khurana, R., Bhasikuttan, A.C. & Mohanty, J. Stimuli-Responsive Cucurbit [7] uril-Mediated BSA Nanoassembly for Uptake and Release of Doxorubicin. *Chemistry–An Asian Journal* **12**, 122-129 (2017).
  117. Kimoon, K., Ho, K.Y. & Narayanan, S. Cucurbiturils: Chemistry, supramolecular chemistry and applications. (World Scientific, 2018).
  118. Zhou, X. et al. Host–Guest Tethered DNA Transducer: ATP Fueled Release of a Protein Inhibitor from Cucurbit [7] uril. *Journal of the American Chemical Society* **139**, 13916-13921 (2017).
  119. El-Sheshtawy, H.S. et al. A Supramolecular Approach for Enhanced Antibacterial Activity and Extended Shelf-life of Fluoroquinolone Drugs with Cucurbit [7] uril. *Scientific reports* **8**, 13925 (2018).
  120. MiáLee, Y., JongáKim, W., HyunáKang, J., YoungáKim, J. & MináPark, K. Cucurbit [6] uril-based polymer nanocapsules as a non-covalent and modular bioimaging platform for multimodal in vivo imaging. *Materials Horizons* **4**,

- 450-455 (2017).
121. Alfaro, I. et al. Silica-coated magnetite nanoparticles functionalized with betaine and their use as an adsorbent for Mo (VI) and Re (VII) species from acidic aqueous solutions. (2019).
  122. Guo, S., Li, D., Zhang, L., Li, J. & Wang, E. Monodisperse mesoporous superparamagnetic single-crystal magnetite nanoparticles for drug delivery. *Biomaterials* **30**, 1881-1889 (2009).
  123. Roefinfard, M. & Bahari, A. Nanostructural Characterization of the Fe<sub>3</sub>O<sub>4</sub>/ZnO Magnetic Nanocomposite as an Application in Medicine. *Journal of Superconductivity and Novel Magnetism* **30**, 3541-3548 (2017).
  124. Xia, T. et al. Facile complex-coprecipitation synthesis of mesoporous Fe<sub>3</sub>O<sub>4</sub> nanocages and their high lithium storage capacity as anode material for lithium-ion batteries. *Electrochimica Acta* **160**, 114-122 (2015).
  125. Zhu, M. et al. Construction of Fe<sub>3</sub>O<sub>4</sub>/Vancomycin/PEG magnetic nanocarrier for highly efficient pathogen enrichment and gene sensing. *ACS applied materials & interfaces* **7**, 12873-12881 (2015).

## ABSTRACT IN KOREAN

### 국문 초록

현재 병원체의 검출 및 치료로서의 접근은 감염을 제어하는데 매우 중요한 역할을 수행하고 있다. 그러나, 일반적으로 사용하는 표준진단방법인 세포 배양 및 콜로니 계수 방법은 대부분의 임상 병원체를 배양하는 데 1~2 일 또는 병원체의 종류에 따라 더 많은 시간이 필요하며, 오염 및 심각한 실험적 오류로 인해 특이도가 낮은 단점을 가지고 있다. 또한, 낮은 약리 효과 및 약물 내성의 증가로 인해 치료 방법이 제한적이다. 따라서 낮은 농도의 표적 병원균을 조기에 검출할 수 있는 빠르고 효과적인 검출 기술 도입이 필요하다. 특히 새로운 항생제에 관한 연구는 전염병의 유행성 감염을 막기 위해 중요하다.

본 연구는 기능화된 생체적합성 나노 물질을 이용한 질병의 진단과 치료를 포함한 생체 응용연구에 초점을 맞추었다. 이에 대형 장비와 세제 없이 빠르고 민감하게 핵산을 분리 및 검출할 수 있는 유용한 진단 방법과 항생제 치료를 위한 나노 물질의 시너지 효과에 대한 기술이 연구 및 개발 되었다.

대표적인 반도체물질인 산화물 아연(ZnO) 나노 물질은 이온 아연 ( $Zn^{2+}$ )에 용해되고 활성 산소를 생성하기 때문에 추가적인 연구를 위한 주요 메커니즘으로 사용이 가능하다. 본 연구는 나노 물질의 모양과 크기를 제어하여 얻은 ZnO 나노 물질을 이용하여 핵산의 추출과 검출 및 병원성 박테리아 치료에 사용 할 수 있음을 연구하였다.

한편, 자연적으로 표면에 수많은 나노 크기의 기공과 풍부한 수산기를 가지고 있는 마이크로 크기의 비정질 실리카 구조인 규조토를 이용하여 화학적 표면 처리의 용이성을 이용하여 생물학적 응용연구에 사용되었다. 이에 규조토의 화학적 표면 처리와 샘플 전 처리에 관하여 연구하였다.

본 연구는 규조토와 산화물 아연이 조합된 나노 물질과 화학적 표면처리 및 homobifunctional imidoester 을 이용하여 현장현시검사를 위해 진행되었다. 또한, 나노 물질들의 시너지 효과를 이용하여 곰팡이 (*Aspergillus fumigatus*)와 그람음성균 (*Escherichia coli* and *Salmonella enterica*)에 대한 항균 활성이 강화됨을 확인하였다.



## ABOUT THE AUTHOR

## LIST OF PUBLICATIONS

1. **Liu, H.**, Zhao, F., Jin, C. E., Koo, B., Lee, E. Y., Yun, K., & **Shin, Y.** (2018). Large instrument-and detergent-free assay for ultrasensitive nucleic acids isolation via binary nanomaterial. *Analytical chemistry*, 90(8), 5108-5115.
2. **Liu, H.**, Zhao, F., Koo, B., Luan, Y., Zhong, L., Yun, K., & **Shin, Y.** (2019). Dimethyl 3, 3'-dithiobispropionimidate (DTBP) as a cleavable disulfide-based polymer to encapsulate nucleic acids in biological sample preparation. *Sensors and Actuators B: Chemical*, 288, 225-231.
3. **Liu, H.**, Luan, Y., Koo, B., Lee, E. Y., Joo, J., Dao, T. N. T., ... & **Shin, Y.** (2019). Cucurbituril-based Reusable Nanocomposites for Efficient Molecular Encapsulation. *ACS Sustainable Chemistry & Engineering*, 7(5), 5440-5448.
4. **Liu, H.**, **Noh, G. S.**, Luan, Y., Qiao, Z., Koo, B., Jang, Y. O., & **Shin, Y.** (2019). A Sample Preparation Technique Using Biocompatible Composites for Biomedical Applications. *Molecules*, 24(7), 1321.
5. **Luan, Y.**, **Liu, H.**, Qiao, Z., Koo, B., Shin, J., Jang, Y. O., ... & **Shin, Y.** (2020). An enhanced recyclable 3D adsorbent for diverse bio-applications using biocompatible magnetic nanomulberry and cucurbituril composites. *Scientific reports*, 10(1), 1-11.
6. **Qiao, Z.**, **Liu, H.**, Noh, G. S., Koo, B., Zou, Q., Yun, K., ... & **Shin, Y.** (2020). A Simple and Rapid Fungal DNA Isolation Assay Based on ZnO Nanoparticles for the Diagnosis of Invasive Aspergillosis. *Micromachines*, 11(5), 515.
7. Noh, G. S., **Liu, H.**, Kim, M. G., Qiao, Z., Jang, Y. O., & Shin, Y. (2020). Multi-Sample Preparation Assay for Isolation of Nucleic Acids Using Bio-Silica with Syringe Filters. *Micromachines*, 11(9), 823.
8. Zhao, F., Koo, B., **Liu, H.**, Jin, C. E., & Shin, Y. (2018). A single-tube approach for in vitro diagnostics using diatomaceous earth and optical sensor. *Biosensors and Bioelectronics*, 99, 443-449.

9. Zhao, F., Lee, E. Y., Noh, G. S., Shin, J., **Liu, H.**, Qiao, Z., & Shin, Y. (2019). A robust, hand-powered, instrument-free sample preparation system for point-of-care pathogen detection. *Scientific reports*, 9(1), 1-11.
10. Koo, B., Jun, E., **Liu, H.**, Kim, E. J., Park, Y. Y., Lim, S. B., ... & Shin, Y. (2020). A biocomposite-based rapid sampling assay for circulating cell-free DNA in liquid biopsy samples from human cancers. *Scientific reports*, 10(1), 1-10.
11. Jang, Y. O., Noh, G. S., **Liu, H.**, Koo, B., Qiao, Z., & Shin, Y. (2020). Dimethyl 3, 3'-dithiobispropionimide-functionalized diatomaceous earth particles for efficient biomolecule separation. *Scientific reports*, 10(1), 1-9.
12. Zhong, L., **Liu, H.**, Samal, M., & Yun, K. (2018). Synthesis of ZnO nanoparticles-decorated spindle-shaped graphene oxide for application in synergistic antibacterial activity. *Journal of Photochemistry and Photobiology B: Biology*, 183, 293-301.
13. **Liu, H., Zhong, L.**, Govindaraju, S., & Yun, K. (2019). ZnO rod decorated with Ag nanoparticles for enhanced photocatalytic degradation of methylene blue. *Journal of Physics and Chemistry of Solids*, 129, 46-53.
14. **Liu, H.**, Zhong, L., Yun, K., & Samal, M. (2016). Synthesis, characterization, and antibacterial properties of silver nanoparticles-graphene and graphene oxide composites. *Biotechnology and bioprocess engineering*, 21(1), 1-18.

## IN PREPARATION

15. **Liu, H., Qiao, Z.,...& Shin, Y.** A Diatom Earth Framework Semiconductor Composite Assisted Antibiotic with Enhanced Efficacy and Therapy Persistence in Nano-therapy
16. **Liu, H., Zou, Q.,...& Shin, Y.** Facile Homobifunctional Imidoester Modification on Advanced Semiconductor Nanomaterials for Enhanced Antibiotic Synergistic Effect and Biocompatibility

## PERSONAL PROFILE

**Name** : Huifang Liu  
**Date of birth** : 1991-December-29  
**Gender** : Female  
**Nationality** : Chinese  
**Marital Status** : Single  
**E-mail** : liuhuifang.1229@gmail.com  
**Phone** : +82 10-2660-9221

### Education:

09/98 ~ 06/03 Miao-Hou Elementary School, Lai Yang, China  
09/03 ~ 06/07 Ji-Ge-Zhuang Middle School, Lai Yang, China  
09/07 ~ 06/10 Lai Yang NO.9 High School, Yan Tai, China  
09/10 ~ 06/14 Lu Dong University (B.D), Yan Tai, China  
09/14 ~ 08/16 Gachon University (M.D), Seongnam, Korea  
03/17 ~ 02/21 University of Ulsan Medical College (Ph.D), Seoul, Korea

### Research:

10/16 ~ 02/21 Asan Medical Center (AMC), Asan Medical Institute of  
Convergence Science and Technology (AMIST),  
Biomedical Engineering Research Center  
Prof. Yong Shin's Laboratory

**Permanent Address** : Lai Yang City, Shan Dong Province, China

**Current Address** : 88 Olympicro-43 gil, Songpa-gu, Seoul, Korea

## REFERENCES

**Prof. Kyusik Yun** (M.D Course) Department. of BioNano Technology, Gachon University, Seongnam, Republic of Korea. E-mail: [ykyusik@gachon.ac.kr](mailto:ykyusik@gachon.ac.kr)

**Prof. Yong Shin** (Ph.D Course) Department of Convergence Medicine, University of Ulsan, Seoul, Republic of Korea. E-mail: [shinyongno1@ulsan.ac.kr](mailto:shinyongno1@ulsan.ac.kr)